Secular Stellar Dynamics near Massive Black Holes

Ann-Marie Madigan

Secular Stellar Dynamics near Massive Black Holes

PROEFSCHRIFT

ter verkrijging van
de graad van Doctor aan de Universiteit Leiden,
op gezag van de Rector Magnificus prof. mr. P. F. van der Heijden,
volgens besluit van het College voor Promoties
te verdedigen op donderdag 16 februari 2012
klokke 11.15 uur

door

Ann-Marie Madigan

geboren te Dublin
in 1982

Promotiecommissie

Promotor: Prof. dr. K. H. Kuijken

Co-Promotors: Dr. Y. Levin (Monash University)
Dr. C. Hopman

Overige leden: Prof. dr. A. Ghez (University of California, Los Angeles)
Prof. dr. R. Genzel (Max Planck Institute for Extraterrestrial Physics)
Prof. dr. S. F. Portegies Zwart
Prof. dr. S. Tremaine (Institute for Advanced Studies, Princeton)

This research has been supported by a TopTalent fellowship from the Netherlands Organisation for Scientific Research (NWO).

for Ev and Dave

ISBN 978-94-6191-145-2
Cover design by Dave Madigan

Contents

Chapter 1. Introduction 1
- 1.1 Massive black holes 2
- 1.2 Mysteries at the Galactic center 2
- 1.3 Stellar dynamics near massive black holes 4
- 1.4 Thesis summary 7

Chapter 2. The Eccentric Disk Instability 11
- 2.1 Introduction 12
- 2.2 The eccentricity instability 12
- 2.3 N-body simulations 14
  - 2.3.1 Initial conditions 14
- 2.4 Results 15
- 2.5 Application to S-stars 16
  - 2.5.1 Bimodal eccentricity distribution in disk 18
- 2.6 Critical discussion 19

Chapter 3. Secular Stellar Dynamics 23
- 3.1 Introduction 24
- 3.2 N-body simulations 25
  - 3.2.1 Model of Galactic nucleus 26
  - 3.2.2 Illustrative simulations 28
- 3.3 Statistical description of resonant relaxation 30
  - 3.3.1 The autoregressive moving average model ARMA(1, 1) . . 32
- 3.4 Interpretation of the ARMA parameters and extension of parameter space 35
  - 3.4.1 Non-resonant relaxation (NR): the parameter σ 36
  - 3.4.2 Persistence of coherent torques: the parameter ϕ 37
  - 3.4.3 Magnitude of resonant relaxation steps: the parameter θ . 39
- 3.5 Results: ARMA analysis of the N-body simulations 40
- 3.6 Monte Carlo simulations and applications 44
  - 3.6.1 Angular momentum 46
  - 3.6.2 Energy 48
  - 3.6.3 Initial conditions and boundary conditions 48
  - 3.6.4 Time steps 48
  - 3.6.5 Treatment of the loss cone 48

3.7 Results 49
  3.7.1 Evolution to steady-state 49
  3.7.2 A depression in the Galactic center 50
  3.7.3 Dynamical evolution of the S-stars 56
3.8 Summary 62
3.A Description of N-body code 65
3.B Energy evolution and cusp formation 67
3.C Precession due to power-law stellar cusp 71
3.D Equations of ARMA(1,1) model 72
  3.D.1 Variance 73
  3.D.2 Autocorrelation function 73
  3.D.3 Variance at coherence time t_ϕ 73

Chapter 4. Build-up of Stars in the Galactic Center 79
4.1 Introduction 80
  4.1.1 Nuclear star cluster formation 80
  4.1.2 Observational constraints from extra-galactic nuclei 80
  4.1.3 Evidence from the Galactic center 81
4.2 Numerical methods and scenarios 84
4.3 Results 88
  4.3.1 Evolution of orbital eccentricities 88
  4.3.2 The high-eccentricity statistic 90
4.4 Summary 94
4.A Statistical constraints on eccentricity from the h-statistic 96

Chapter 5. Secular Dynamical Anti-Friction 103
5.1 Introduction 104
5.2 Secular dynamical anti-friction 105
  5.2.1 Increase in orbital eccentricity 109
  5.2.2 Comparison with theories in the literature 109
5.3 Numerical method and simulations 110
  5.3.1 Secular horseshoe orbits 112
  5.3.2 Separation of potential into pro- and retro- grade orbits . 113
  5.3.3 Increase in orbital eccentricity of IMBH 114
5.4 Discussion 115

Nederlandse samenvatting (Dutch Summary) **119**

Curriculum Vitae **123**

Acknowledgments **125**

1

Introduction

Stars near massive black holes move on elliptical orbits which precess slowly, exerting persistent gravitational torques on each other. In this thesis we present four important consequences of these gravitational torques: 1) A new instability which exposes the inherently unstable nature of eccentric stellar disks in galactic nuclei, 2) A density depression of stars near massive black holes due to enhanced angular momentum relaxation and tidal disruptions, 3) A signature of high-eccentricity orbits for stars formed by Hills' mechanism at large radii from the massive black hole, and a directly-observable statistic that can highlight these populations, and 4) A new dynamical process which we call "secular dynamical anti-friction" which boosts the orbital eccentricity of hypothesized intermediate-mass black holes as they spiral into massive black holes.

Ann-Marie Madigan 2011

Figure 1.1 – Composite image of the Galactic center ($2280'' \times 840''$) with the Hubble Space Telescope (near-infrared, in yellow), Spitzer Space Telescope (infrared, in red) and Chandra X-ray Observatory (X-ray, in blue/violet). The bright white cluster at lower middle-right is the location of the MBH SgrA*. *Credit: X-ray: NASA/CXC/UMass/D. Wang et al.; Optical: NASA/ESA/STScI/D.Wang et al.; IR: NASA/JPL-Caltech/SSC/S.Stolovy*.

1.1 Massive black holes

Massive black holes (MBHs) are found in the nuclei of most, if not all, galaxies (Ferrarese & Ford 2005). Embedded in dense star clusters, they dominate the gravitational potential out to their dynamical radius where the mass in stars becomes comparable to that of the MBH. If one understands the dynamics of stars within this radius, one can provide a theoretical framework for some of the most energetic phenomena in the universe such as the tidal disruption of stars and launching of relativistic jets. Compact stellar remnants on high-eccentricity orbits within these clusters, such as neutron stars, white dwarfs and stellar-mass black holes, interact with the MBH producing gravitational waves potentially detectable by future space observatories.

1.2 Mysteries at the Galactic center

In the center of our Galaxy, at a distance of $\sim 8\,\mathrm{kpc}$ (Eisenhauer et al. 2003; Ghez et al. 2008; Gillessen et al. 2009), there quietly lives a MBH[1]. Though highly under-luminous with respect to its Eddington luminosity (Melia & Falcke 2001), its presence is inferred by the effect it has on the orbits of stars that live in the surrounding dense nuclear star cluster. Just as (exo-)planets revolve around their sun, so too do the stars in the Galactic center orbit the MBH on near-Kepler ellipses.

---

[1] At this distance $1'' \sim 0.038$ pc.

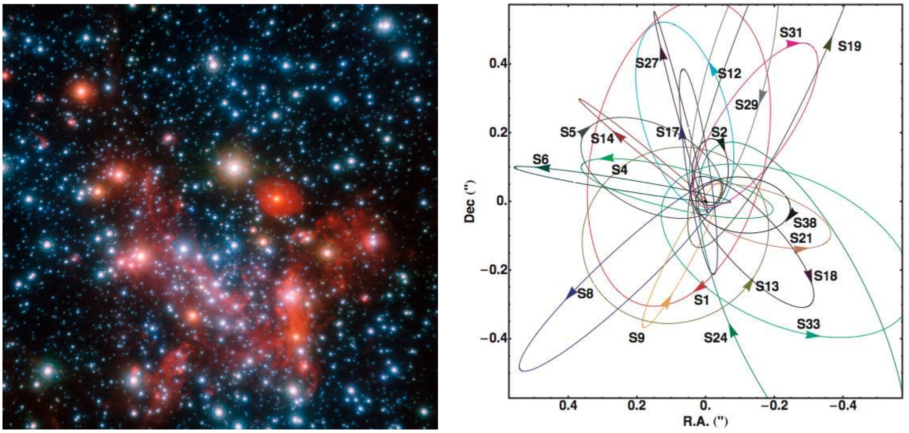

Figure 1.2 – *Left* - The central $\sim 20''$ of our Galaxy imaged in near-infrared. *Right* - The S-star orbits: the result of 16 years of tracking the motions of stars around the MBH in the Galactic center. *Credit: ESO/Gillessen et al. (2009).*

Obscuration from interstellar dust in the plane of the Galaxy results in a high optical extinction of ~ 30 magnitudes towards the Galactic center. For this reason, observations of the stars near the MBH are taken at longer, near-infrared wavelengths. The development of near-infrared instruments, adaptive optics and integral field spectroscopy has lead to dramatic progress in our knowledge of the Galactic center in the past two decades. Angular resolution has improved by more than an order of magnitude to $\sim 5 \times 10^{-4}$ arcseconds, and sensitivity by three to five magnitudes to $K_s \sim 16-18$, for spectroscopy and imaging respectively (Genzel et al. 2010). Using astrometric tracking of the orbits of luminous B-stars, astronomers have revealed that the MBH (known as SgrA*) has a mass of $M_\bullet \simeq 4 \times 10^6 M_\odot$. The most intensely-studied of these stars is called S0/S0-2; with an orbital period of just 15.2 years (Schödel et al. 2003) its orbit has been fully traced and shown to be a bound, high-eccentricity Kepler ellipse.

The proximity of the Galactic center makes it unique among galactic nuclei in that one can resolve individual stars of different ages and potentially test decades-old predictions of the dynamics of stars near MBHs. One such prediction is a lack of young stars near the MBH; its immense tidal force prohibits star formation from the collapse and fragmentation of molecular gas clouds (Sanders 1992; Morris 1993). We do however observe many (~ 200) early type stars within the central parsec. They can be separated roughly into two groups. The first is a population of O and Wolf-Rayet (WR) stars, $\sim 6 \pm 2\,\mathrm{Myr}$ old, with masses $\gtrsim 20 M_\odot$ (Paumard et al. 2006). The majority form a well-defined, warped disk with projected radii $0.8'' - 12''$, which rotates clockwise on the sky (Levin & Beloborodov 2003; Genzel et al. 2003; Lu et al. 2009; Bartko et al. 2009). The second population is an apparently isotropic distribution of B-stars

($< 10 \sim 100\,\mathrm{Myr}$). Those that lie within the central $0.8''$ are often collectively referred to as the "S-stars"; see Figure 1.2. Their kinematics reveal randomly-inclined and highly-eccentric orbits (Ghez et al. 2005; Gillessen et al. 2009). Their proximity to the MBH, combined with their young ages, are indicative of a "paradox of youth" (Ghez et al. 2003; Eisenhauer et al. 2005; Martins et al. 2008). They could not have formed in-situ, but due to their young ages they have not had much time to dynamically migrate to their current locations.

Another prediction is that we would expect, due to gravitational interactions, that the population of late type stars in the Galactic nuclear star cluster is dynamically relaxed and forms a steep density power-law cusp around the MBH (e.g., Bahcall & Wolf 1976). However, the late type k-giants, 1–$10\,\mathrm{Gyr}$ old, do not show a central concentration as is theoretically expected for a steady-state stellar cusp (Do et al. 2009; Buchholz et al. 2009; Bartko et al. 2010), a fact reflected in the flattening of the surface brightness distribution of diffuse stellar light (Yusef-Zadeh et al. 2011). Instead they suggest the presence of a $\sim 0.3\,\mathrm{pc}$ scale core, a puzzle referred to as the "conundrum of old age" (Merritt 2011).

This thesis aims to address these types of puzzles at the Galactic center. To begin, we must first ask, *how do stars move and gravitationally interact with each other around MBHs?* This simple question is key to understanding the dynamics of stars near MBHs – the dynamics responsible for illuminating the MBH both through highly-energetic phenomena and gravitational-wave astrophysics.

1.3 Stellar dynamics near massive black holes

One can picture stars moving on orbits determined by the combined smooth gravitational potential of the MBH and surrounding cluster stars. The orbit of a star can be described by its six phase space parameters $(\mathbf{r}, \mathbf{v})$ or alternatively by its energy and angular momentum (E, J). In a Kepler potential, the stellar orbit is an ellipse with specific energy and angular momentum

$$E = -\frac{GM_\bullet}{2a}, \tag{1.1}$$

$$J = J_c(1-e^2)^{1/2}, \tag{1.2}$$

where e is the eccentricity and $J_c = \sqrt{GM_\bullet a}$ is the circular (maximum) angular momentum of a star with semi-major axis a. Due to the additional potential of the surrounding stars in the cluster (and general relativistic effects), the stellar orbit will experience apisidal precession (see Figure 1.3) which can be described as a rotation in the eccentricity vector in the retrograde (prograde) direction.

In reality, the stars are not moving in a smooth potential – they feel gravitational forces from each other and are perturbed from their original orbits. To calculate the timescale over which a star will be significantly perturbed away

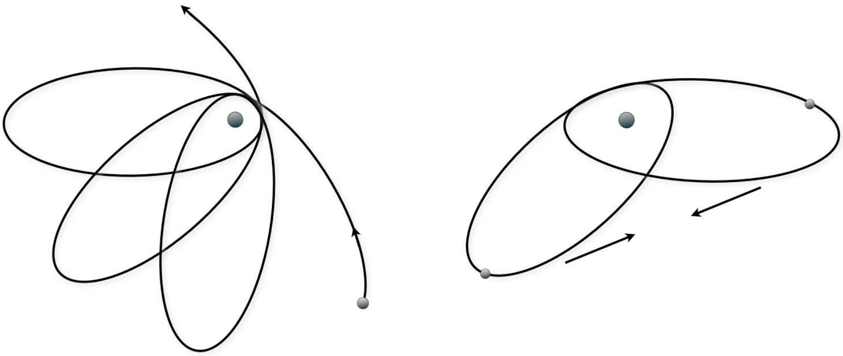

Figure 1.3 – *Left* - Illustration of the apsidal precession of a stellar orbit (retrograde with respect to the star's motion) due to the additional Newtonian potential from surrounding stars near the MBH. *Right* - Schematic diagram illustrating coherent torques between two stellar orbits.

from its original orbit (known as the relaxation time), we follow the outline of the derivation[2] by Rauch & Tremaine (1996).

We consider a spherical volume of radius R centred on a point mass – an MBH of mass $M_\bullet$ – populated uniformly with $N \gg 1$ stars of mass m which move with average velocity $V \sim \sqrt{GM_\bullet/R}$. As $Nm \ll M_\bullet$, the stellar orbits are Kepler ellipses which precess on a timescale

$$t_{\rm prec} \sim \frac{M_\bullet}{Nm} P, \tag{1.3}$$

where P is the orbital period of order $\sim R/V$. The relaxation time for a single test star may be derived considering a spherical shell of outer radius $r \ll R$ and inner radius $1/2\, r$, centred on the test star. The number of stars within this shell is $n \sim N(r/R)^3$; the instantaneous number fluctuates by $n^{1/2}$. Hence the test star experiences a fluctuating gravitational acceleration of magnitude

$$a \sim \frac{Gmn^{1/2}}{r^2}, \tag{1.4}$$

on a timescale $t_f \sim r/V$. The typical impulse is therefore

$$\delta v \sim a t_f \sim \frac{Gmn^{1/2}}{rV}. \tag{1.5}$$

As successive impulses are uncorrelated, the total impulse in time t is

$$(\Delta v)^2 \sim (\delta v)^2 \frac{t}{t_f} \sim \frac{G^2 m^2 N}{R^3 V} t \sim V^2 \frac{m^2 N}{M_\bullet^2} \frac{t}{P}. \tag{1.6}$$

---

[2] We will ignore factors of order unity throughout the derivation.

Δv is independent of r. Hence the shells spanning the radii $(1/2\, r, r)$, $(r, 2r)$ $\ldots$ all contribute equally to the relaxation rate of the test star. We account for this by multiplying the total rate by the Coulomb logarithm $\ln \Lambda$, which represents the number of octaves that lead to to the relaxation of the test star. Defining the non-resonant relaxation time as $(\Delta v/V)^2 = t/t_{\mathrm{rel}}^{\mathrm{nr}}$, we find

$$t_{\mathrm{rel}}^{\mathrm{nr}} \sim \frac{M_\bullet^2}{m^2 N \ln \Lambda} P. \tag{1.7}$$

The fluctuating force changes both energy and angular momentum of the stellar orbit, such that

$$\frac{\Delta E}{E} \sim \frac{\Delta J}{J_c} \sim \left(\frac{t}{t_{\mathrm{rel}}^{\mathrm{nr}}}\right)^{1/2} \sim \frac{m(N \ln \Lambda)^{1/2}}{M_\bullet} \left(\frac{t}{P}\right)^{1/2}. \tag{1.8}$$

The characteristic timescale of this non-resonant relaxation in the Galactic center is greater than $5\,\mathrm{Gyr}$ at all radii (Merritt 2010). This means that, under this mechanism, stars will retain memory of their initial orbital parameters for very long times. It is this form of stellar relaxation that underlies many long-standing predictions about the distribution of stars around MBHs.

However, as demonstrated by Rauch & Tremaine (1996), rapidly fluctuating forces are not the dominant mechanism for stellar relaxation near MBHs. Stars orbiting in the gravitational potential of a MBH move along nearly-closed Kepler ellipses, which remain fixed in space over long timescales. It is therefore instructive to imagine the mass of each star spread out along its orbit, with the density at each segment inversely proportional to the local speed in the orbit. Instead of a system of point particles orbiting the MBH, one can imagine a collection of massive stellar 'wires'. Over a timescale $P \ll t \ll t_{\mathrm{prec}}$, the wires remain fixed in space and exert persistent mutual torques on each other (see Figure 1.3). The specific torques are of the order

$$\tau \sim \frac{GmN^{1/2}}{R}. \tag{1.9}$$

As the gravitational potential remains stationary over this timescale, there is no additional energy relaxation, but the torques change the angular momenta of the stellar wires, $\Delta J \sim \tau t$. The apisidal precession of the stellar wires limits the timescale over which the torques act on each other. For a time $t \ll t_{\mathrm{prec}}$,

$$\frac{\Delta J}{J_c} \sim \frac{N^{1/2} m}{M_\bullet} \left(\frac{t}{P}\right). \tag{1.10}$$

For $t \gg t_{\mathrm{prec}}$, the change in angular momentum is a random walk with increments of the order

$$\begin{aligned} \frac{\Delta J}{J_c} &\sim \frac{N^{1/2} m}{M_\bullet} \left(\frac{t_{\mathrm{prec}}}{P}\right) \left(\frac{t}{t_{\mathrm{prec}}}\right)^{1/2} \\ &\sim \left(\frac{m}{M_\bullet}\right)^{1/2} \left(\frac{t}{P}\right)^{1/2}. \end{aligned} \tag{1.11}$$

Defining the resonant relaxation[3] time as $(\Delta J/J_c)^2 = t/t_{\rm rel}^{\rm rr}$,

$$t_{\rm rel}^{\rm rr} \sim \frac{M_\bullet}{m} P. \tag{1.12}$$

The resonant relaxation time is shorter than the non-resonant timescale by a factor $(mN/M_\bullet)\ln\Lambda$, depending on the eccentricity of the stellar orbit (Gürkan & Hopman 2007). In the Galactic center this difference in timescale can be greater than two orders of magnitude, making secular torques between stellar orbits the driving mechanism for angular momentum relaxation. This thesis explores the consequences of these secular torques, and applies the results to the observations of stars in the Galactic center.

1.4 Thesis summary

In **Chapter 2**, we present a new secular gravitational instability present in coherently eccentric disks of stars around MBHs in galactic nuclei. The instability separates, on less than a precession timescale, both the scalar values and the directions of the eccentricity vectors of the stellar orbits within the disk. We apply our results to the Galactic center and propose that the O/WR stars fragmented from a gaseous, coherently eccentric disk and were promptly subject to this instability. The observed bi-modality in the eccentricity distribution of the disk may be explained in this way. Binary stars propelled to high eccentricity orbits may have played a role in the formation of the S-stars, and of the hyper-velocity stars in the Galactic halo through Hills (1988) mechanism.

We investigate the long-term angular momentum evolution of stars around MBHs in **Chapter 3**. We perform Monte Carlo simulations which use an autoregressive moving average (ARMA) equation for angular momentum evolution to capture the statistics of both two-body and resonant relaxation. We show that for a single-mass system in steady state, a depression is carved out near an MBH as a result of tidal disruptions. In context of the Galactic center, the extent of the depression is about 0.1 pc, of similar order to but less than the size of the observed “hole” in the distribution of bright late-type stars. We furthermore predict that the velocity vectors of stars around an MBH are locally not isotropic. As a final application, we use the ARMA code to evolve high-eccentricity S-star orbits that result from the tidal disruption of binary stars, and find that RR predicts more highly eccentric ($e > 0.9$) orbits than have been observed to date. In this chapter we also describe in detail our special purpose N-body code, which we use in extensive N-body simulations to calibrate the ARMA equation.

In **Chapter 4** we investigate the build-up of stars in the Galactic center. We contrast two formation scenarios for the intermediate-aged B-stars which are on the order of $\sim 100\,\mathrm{Myr}$ old – episodic star formation in nuclear disks, and tidal disruptions of binaries by the MBH. We perform N-body simulations to show that after $6\,\mathrm{Myr}$ of gravitational interactions with the O/WR disk, the two scenarios lead to very different dynamical outcomes. In particular, we find a high-eccentricity signature at large radii for the stars in the tidal disruption scenario. We present a new statistic, h, that uses directly-observable kinematical stellar data to highlight high-eccentricity populations, and show how this statistic may distinguish between the two scenarios.

---

[3] The term ‘resonant’ refers to the $1:1$ resonance in the azimuthal and radial frequencies in a Kepler ellipse. Resonant relaxation is a secular relaxation process in that the position of the star along its orbit is dynamically unimportant.

In **Chapter 5** we present a new gravitational dynamical process in galactic nuclei containing MBHs, which we call secular dynamical anti-friction (SDAF). We show that the gravitational torque exerted on the orbit of a massive body by less massive bodies comes from a force acting parallel to its direction of precession - a dynamical *anti*-friction which affects the angular momentum of the orbit, not the energy. Together with Chandrasekhar's dynamical friction the effective result of this anti-friction is to increase the orbital eccentricity of the more massive object. N-body simulations of the inspiral and coalescence of intermediate-mass black holes into MBHs show this increase in eccentricity, but as of yet the underlying mechanism has eluded a complete description. In this chapter we show that the theory of SDAF can account for such an increase.

References

Bahcall, J. N. & Wolf, R. A. 1976, ApJ, 209, 214

Bartko, H., Martins, F., Fritz, T. K., Genzel, R., Levin, Y., Perets, H. B., Paumard, T., Nayakshin, S., Gerhard, O., Alexander, T., Dodds-Eden, K., Eisenhauer, F., Gillessen, S., Mascetti, L., Ott, T., Perrin, G., Pfuhl, O., Reid, M. J., Rouan, D., Sternberg, A., & Trippe, S. 2009, ApJ, 697, 1741

Bartko, H., Martins, F., Trippe, S., Fritz, T. K., Genzel, R., Ott, T., Eisenhauer, F., Gillessen, S., Paumard, T., Alexander, T., Dodds-Eden, K., Gerhard, O., Levin, Y., Mascetti, L., Nayakshin, S., Perets, H. B., Perrin, G., Pfuhl, O., Reid, M. J., Rouan, D., Zilka, M., & Sternberg, A. 2010, ApJ, 708, 834

Buchholz, R. M., Schödel, R., & Eckart, A. 2009, A&A, 499, 483

Do, T., Ghez, A. M., Morris, M. R., Lu, J. R., Matthews, K., Yelda, S., & Larkin, J. 2009, ApJ, 703, 1323

Eisenhauer, F., Schödel, R., Genzel, R., Ott, T., Tecza, M., Abuter, R., Eckart, A., & Alexander, T. 2003, ApJ, 597, L121

Ferrarese, L. & Ford, H. 2005, Space Science Reviews, 116, 523

Genzel, R. et al. 2003, ApJ, 594, 812

Genzel, R., Eisenhauer, F., & Gillessen, S. 2010, Reviews of Modern Physics, 82, 3121

Ghez, A. M. et al. 2003, ApJ, 586, L127

Ghez, A. M., Salim, S., Hornstein, S. D., Tanner, A., Lu, J. R., Morris, M., Becklin, E. E., & Duchêne, G. 2005, ApJ, 620, 744

Ghez, A. M., Salim, S., Weinberg, N. N., Lu, J. R., Do, T., Dunn, J. K., Matthews, K., Morris, M. R., Yelda, S., Becklin, E. E., Kremenek, T., Milosavljevic, M., & Naiman, J. 2008, ApJ, 689, 1044

Gillessen, S., Eisenhauer, F., Trippe, S., Alexander, T., Genzel, R., Martins, F., & Ott, T. 2009, ApJ, 692, 1075

Gürkan, M. A. & Hopman, C. 2007, MNRAS, 379, 1083

Hills, J. G. 1988, Nature, 331, 687

Levin, Y. & Beloborodov, A. M. 2003, ApJ, 590, L33

Lu, J. R., Ghez, A. M., Hornstein, S. D., Morris, M. R., Becklin, E. E., & Matthews, K. 2009, ApJ, 690, 1463

Martins, F., Gillessen, S., Eisenhauer, F., Genzel, R., Ott, T., & Trippe, S. 2008, ApJ, 672, L119

Melia, F. & Falcke, H. 2001, ARA&A, 39, 309

Merritt, D. 2010, ApJ, 718, 739

Merritt, D. 2011, in ASP Conf. Ser. 439, The Galactic Center: a Window to the Nuclear Environment of Disk Galaxies, ed. M. R. Morris, Q. D. Wang, & F. Yuan, 142

Morris, M. 1993, ApJ, 408, 496

Paumard, T., Genzel, R., Martins, F., Nayakshin, S., Beloborodov, A. M., Levin, Y., Trippe, S., Eisenhauer, F., Ott, T., Gillessen, S., Abuter, R., Cuadra, J., Alexander, T., & Sternberg, A. 2006, ApJ, 643, 1011

Rauch, K. P. & Tremaine, S. 1996, New Astronomy, 1, 149

Sanders, R. H. 1992, Nature, 359, 131

Schödel, R., Ott, T., Genzel, R., Hofmann, R., Lehnert, M., Eckart, A., Mouawad, N., Alexander, T., et al., Nature, 419, 694

Yusef-Zadeh, F., Bushouse, H., & Wardle, M. 2011, ArXiv e-prints

2

A New Secular Instability of Eccentric Stellar Disks Around Supermassive Black Holes, with Application to the Galactic Center

We identify a new secular instability of eccentric stellar disks around supermassive black holes. We show that retrograde precession of the stellar orbits, due to the presence of a stellar cusp, induces coherent torques that amplify deviations of individual orbital eccentricities from the average, and thus drive all eccentricities away from their initial value. We investigate the instability using N-body simulations, and show that it can propel individual orbital eccentricities to significantly higher or lower values on the order of a precession time-scale.

This physics is relevant for the Galactic center, where massive stars are likely to form in eccentric disks around the SgrA* black hole. We show that the observed bimodal eccentricity distribution of disk stars in the Galactic center is in good agreement with the distribution resulting from the eccentricity instability and demonstrate how the dynamical evolution of such a disk results in several of its stars acquiring high $(1 - e \ll 0.1)$ orbital eccentricity. Binary stars on such highly eccentric orbits would get tidally disrupted by the SgrA* black hole, possibly producing both S-stars near the black hole and high-velocity stars in the Galactic halo.

Ann-Marie Madigan, Yuri Levin and Clovis Hopman
The Astrophysical Journal Letters, 697, 44M (2009)

2.1 Introduction

Most well-observed galaxies with stellar bulges show evidence for supermassive black holes (SMBHs) in their centers (Kormendy 2004). An important feature of stellar dynamics in galactic nuclei is that for orbits contained well within the SMBH's radius of influence, the precession time $t_{\rm prec}$ is many orders of magnitude larger than their period P.[1] Therefore, for a study of long-term (secular) gravitational dynamics, it is useful to think of the stars not as particles but as massive elliptical wires stretched along the stars' eccentric orbits (Rauch & Tremaine 1996). Gravitational torques between the wires can become the dominant mode of orbital eccentricity evolution, as is seen in the case of resonant relaxation (Rauch & Tremaine 1996; Gürkan & Hopman 2007; Touma et al. 2009; Eilon et al. 2008). Secular effects have a significant impact on the stability of stellar cusps (Tremaine 2005; Polyachenko & Shukhman 1981; Polyachenko et al. 2008), on gravitational wave emission from in-spiraling compact objects (Hopman & Alexander 2006a,b), on tidal disruption of stars (Rauch & Ingalls 1998) and, as we show here, on the origin of the S-stars in the Galactic center.

In this chapter we describe a mechanism for generating high-eccentricity stars via a fast secular instability of an eccentric stellar disk (Section 2.2). We use N-body simulations to investigate the non-linear development of the instability (Section 2.3 and Section 2.4) and to explore its dependence on the initial eccentricity and mass of the disk. We then show that the instability may be relevant for young stars in the Galactic center, and may provide an interesting channel for formation of the S-stars and of high-velocity stars in the Galactic halo (Section 2.5). We critically discuss our results in Section 2.6.

2.2 The eccentricity instability

Consider a thin stellar disk of mass $M_{\rm disk}$ around a SMBH of mass $M_\bullet$ which is embedded in a power-law stellar cusp of mass $M_{\rm cusp}$. Our two main assumptions are that (1) $M_{\rm disk} \ll M_{\rm cusp}$, so that precession of individual orbits is driven by the cusp, and (2) initially the stellar eccentricity vectors

$$\mathbf{e} = \frac{1}{GM_\bullet}\mathbf{v} \times (\mathbf{r} \times \mathbf{v}) - \hat{\mathbf{r}} \tag{2.1}$$

are aligned and similar in magnitude so that the disk precesses coherently as a whole (for a typical power-law cusp, the orbital precession rate depends only weakly on the semi-major axis; see below). Here $|\mathbf{e}|$ corresponds to the magnitude of the eccentricity of the orbit and $\mathbf{r}$ and $\mathbf{v}$ are the position and velocity vectors respectively. Both assumptions are realistic for a disk of young stars formed in a galactic center via the gravitational capture of part of an infalling molecular cloud: observations reveal a massive spherical stellar cusp

---

[1] This is in contrast to the rapidly precessing stellar orbits typical for globular clusters or galaxies.

(Genzel et al. 2003; Schödel et al. 2007), while hydrodynamical simulations tentatively show similar, aligned initial orbital eccentricities of young stars[2] (Sanders 1998; Alexander et al. 2008; Bonnell & Rice 2008; Hobbs & Nayakshin 2009). The orbits precess in the direction opposite to the orbital rotation of the stars. The precession time-scale scales as

$$\begin{aligned} t_{\rm prec} &\sim \frac{M_\bullet}{N(<a)m} P(a) f(e) \\ &\propto a^{\gamma-3/2} f(e) \end{aligned} \tag{2.2}$$

where $P(a) = 2\pi\sqrt{a^3/GM_\bullet}$ is the period of a star with semi-major axis a, $N(<a)$ is the number of stars in the cusp within a, m is the individual mass of the stars, and γ is the power-law index for the space-density $\rho(r) \propto r^{-\gamma}$. For a power-law cusp with $\gamma = 3/2$, formed in the special case when the SMBH grows adiabatically (Young 1980), $t_{\rm prec}$ is constant for all a.

Observations of the Galactic center indicate that there is a stellar cusp in the inner parsec, with published measurements of the slope not significantly different from $\gamma = 3/2$, e.g. $\gamma = 1.4 \pm 0.1$ (Genzel et al. 2003) and $\gamma = 1.19 \pm 0.05$ (Schödel et al. 2007). It is important to stress that these observations only show a small and biased subset of the stellar content in that region. They are restricted to massive young stars, that have not yet relaxed, and to giants, which have relaxed, but are affected by hydrodynamical collisions with other stars (e.g. Alexander 1999). These two stellar types are not expected to dominate the density. Instead, theoretical models accounting for mass-segregation show that the density at the regions of interest is mostly determined by stellar black holes and main sequence stars, with cusp values between $\gamma_{\rm MS} = 1.4$ and $\gamma_{\rm BH} = 2.0$ (Alexander et al. 2008). We conclude that both theory and observations yield values of γ close to $3/2$ and the dependence of $t_{\rm prec}$ on a is weak.

A key element of the eccentric instability is that $f(e)$ in Equation (2.2) is an increasing function of eccentricity (e.g. Binney & Tremaine 2008), so that an orbit that is slightly more eccentric than average will lag behind in precession. Such a star will feel a strong, coherent torque from the other stars in the disk, in the *opposite* direction of its angular momentum vector. As a result, its angular momentum decreases in magnitude, causing its eccentricity to increase even further. In this way, very high eccentricities can potentially be achieved. Conversely, if a stellar orbit is slightly less eccentric than the average, it will have a higher precession rate, thus experiencing a torque which acts to decrease its eccentricity further.

---

[2] Bonnell & Rice (2008) make two large simulations, investigating star-formation in the Galactic center. In their Run 1 they find $0.6 < e < 0.7$, while in Run 2 the inner edge of the disk is circularized, and hence the stellar eccentricities range between 0 in the inner disk and ~ 0.6 in the outer. While the precise nature of the circularization, or its absence, has not been investigated, it is clear that it depends on the initial conditions.

We thus find that the initial eccentricity vector distribution is unstable, due to a combination of retrograde precession and $df/de > 0$, and that all eccentricities are driven away from the initial eccentricity of the disk. It can be shown analytically that the initial growth timescale of the eccentric instability scales as

$$\tau_{\rm growth} \sim t_{\rm prec} \left(\frac{M_{\rm cusp}}{M_{\rm disk}}\right)^{1/2} \left[e\sqrt{1-e^2}\,\frac{d}{de}\left(\frac{1}{f(e)}\right)\right]^{-1/2}. \tag{2.3}$$

For the Galactic center this amounts to several precession time-scales. We now demonstrate the eccentricity instability using N-body simulations and look at its impact on the young stars in the Galactic center.

2.3 N-body simulations

We summarize a newly-developed code which we have used in these simulations. Our integrator is based on a 4th-order Wisdom-Holman algorithm (Wisdom & Holman 1991; Yoshida 1990), where the forces on a particle are split into a dominant Keplerian force and perturbation forces. We use Kepler's equation to integrate the orbit (Danby 1992), keeping the position of the central object fixed. We use adaptive time-stepping to deal with close encounters and the algorithm is not strictly energy conserving. We implement time-symmetry to reduce the energy error and the K_2 kernel from Dehnen (2001) for gravitational softening. The overall fractional energy error for these simulations is typically $\sim 10^{-8}$ or less. We describe the code in detail in Chapter 3.

2.3.1 Initial conditions

We have three main components in our simulations. (1) An eccentric disk with surface density profile $\Sigma \propto r^{-2}$ (cf. Paumard et al. 2006), consisting of 100 equal-mass stars, with semi-major axes $0.05\,{\rm pc} \leq a \leq 0.5\,{\rm pc}$. We vary the masses of the stars for different simulations. We initialize the eccentricity vectors of all stars pointing in roughly the same direction, though they are scattered in their orbital phase. The initial rms inclination is ~ 0.01. (2) A SMBH of $4 \times 10^6 M_\odot$ (Ghez et al. 2008), and (3) a smooth stellar cusp with density profile index $\gamma = 1.5$ and a mass of $0.5 \times 10^6 M_\odot$ within 1 pc (Schödel et al. 2007; Genzel et al. 2003). The stars within the disk precess due to the cusp and experience a prograde general relativistic precession which amounts to apsidal precession of the orbit by an angle

$$\delta\phi_{\rm prec} = \frac{6\pi G M_\bullet}{a(1-e^2)c^2} \tag{2.4}$$

per orbit. Precession due to self-gravity of the disk is minimal. To verify our results, we also run simulations with twice the number of half-as-massive stars and various softening parameters. We discuss the use of different values of γ (e.g. Bahcall & Wolf 1976) in Section 2.6.

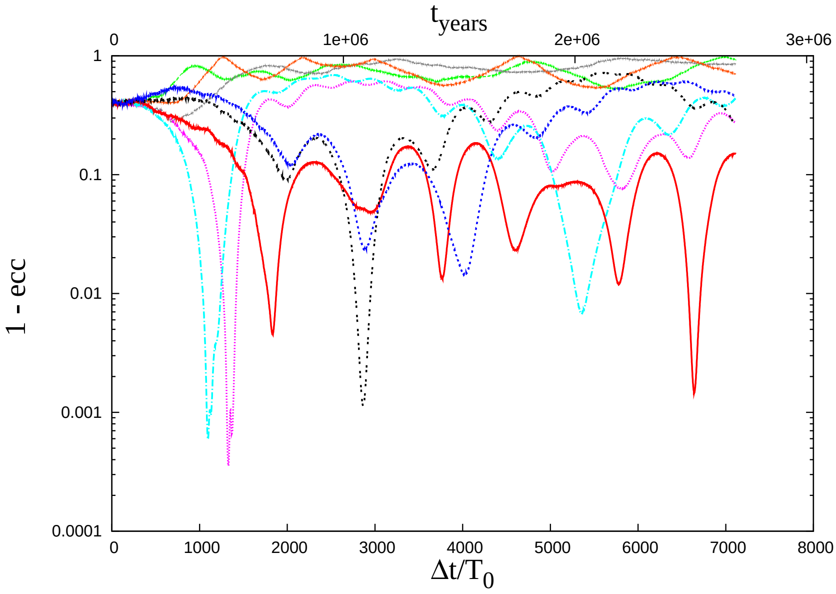

Figure 2.1 – Eccentricity evolution of stars in an eccentric disk ($M_{\rm disk} = 8 \times 10^3 M_\odot$) as a function of time. Δt is elapsed time expressed in units of the initial period of the innermost orbit T_0 ($t_{\rm prec} \sim 1200\ T_0$). The smoothly varying behavior is characteristic of the secular nature of the instability.

2.4 Results

With a mass of $8 \times 10^3 M_\odot$ and an initial eccentricity of 0.6, we let the disk of stars evolve for several precession times ($t_{\rm prec} \sim$ 0.6 - 0.7 Myrs or $\sim$ 1200 orbits at a = 0.05 $\,$pc). In Figure (2.1) we show a selection of stars from this run which best demonstrates the dispersion of the disk's initial eccentricity, while Figure (2.2) follows the evolution of the eccentricity vectors (this time for $M_{\rm disk} = 4 \times 10^3 M_\odot$). The circles in the latter plot indicate the stars experiencing the highest torque (τ) and hence angular momentum changes. Note that the highest eccentricity orbits are precessing behind the bulk of the stars as expected. We find a monotonically decreasing relationship between the rate of change of angular momentum, i.e. torque on each orbit, and semi-major axis a.

The effects of the instability on the stellar eccentricity distribution are evident after $\sim 0.5 - 1\ t_{\rm prec}$ and the strongest torques are experienced over a few precession times before the disk loses coherence.

We explore the dependence of the final range of eccentricities on the mass and initial eccentricity of the disk. To this end, we run a set of simulations with a disk of initial eccentricity 0.6 for various disk masses (4, 6, 8, 10 $\times 10^3 M_\odot$), and a set with $M_{\rm disk} = 10^4 M_\odot$ for various initial eccentricities (0.1, 0.4, 0.5,

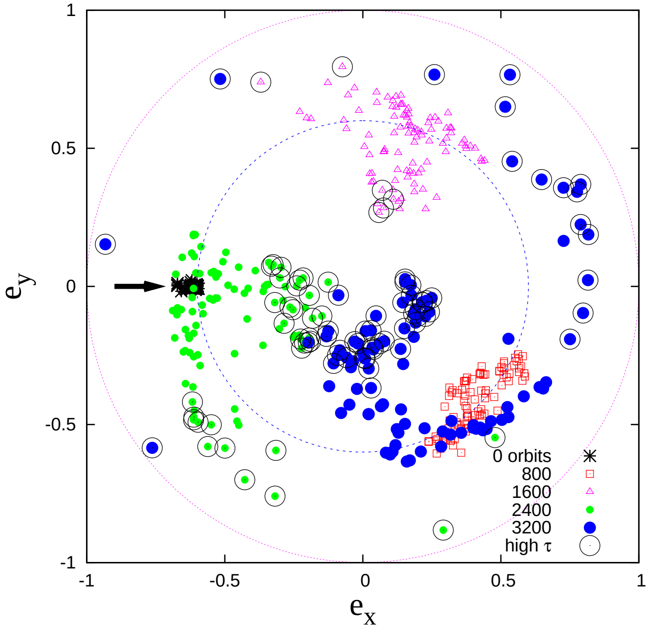

Figure 2.2 – Evolution of the eccentricity vectors of all the stars in the disk ($M_{\rm disk} = 4 \times 10^3 M_\odot$) for different times. The outermost circle indicates where $|\mathbf{e}| = 1$; the inner circle indicates the initial value of the eccentricities $|\mathbf{e}| = 0.6$. An arrow points to the initial positions. The eccentricity vectors spread out as the stars complete more and more orbits, and precess with retrograde motion. Those experiencing the highest torques (τ) are over-plotted with small circles. As the eccentric disk instability predicts, the slowest precessing orbits have the highest eccentricities. In addition, orbits with low eccentricity clump together at late times. We believe non-linear effects are responsible for this feature.

0.6, 0.7, 0.9). The results are presented in Table (2.1). Higher initial eccentricities and masses of the disk are correlated with higher resulting eccentricities. We also see a correlation between the highest eccentricities and inclinations reached, with the largest values occurring at the smallest radii.

In contrast to the secular instability described in Tremaine (2005), relativistic effects in this case do not promote stability once the relativistic prograde precession rate exceeds that of the retrograde precession due to the cusp. The highest eccentricity orbit precesses with prograde motion at a higher rate than the average and again experiences a torque in the opposite direction of its angular momentum.

2.5 Application to S-stars

The region surrounding the SMBH in the Galactic center (Gillessen et al. 2009) is host to several interesting populations of young stars, which include one

Table 2.1 – Simulation Parameters and Statistics of S-stars

M_{disk} ($M_\odot$)	e_{disk}	$e_{\text{high}}{}^{a}$	$i_{\text{high}}{}^{b}$ (rads)	a_{bin} (AU)	r_t (pc)	$a_\bullet$ (pc)	$r_p < r_t{}^{c}$ (%)
4×10^3	0. 4	0.8755	0.4662	0.1	3.57×10^{-5}	0.0026	0
...	...	...	...	1	3.57×10^{-4}	0.026	0
...	0.6	0.9691	0.7960	0.1	3.57×10^{-5}	0.0026	0
...	...	...	...	1	3.57×10^{-4}	0.026	0
6×10^3	0.6	0.9981	1.824	0.1	3.57×10^{-5}	0.0026	4
...	...	...	...	1	3.57×10^{-4}	0.026	8
8×10^3	0. 4	0.8796	0.6643	0.1	3.57×10^{-5}	0.0026	0
...	...	...	...	1	3.57×10^{-4}	0.026	0
...	0.6	0.9993	2.170	0.1	3.57×10^{-5}	0.0026	3
...	...	...	...	1	3.57×10^{-4}	0.026	7
1×10^4	0.1	0.5115	0.2935	0.1	3.57×10^{-5}	0.0026	0
...	...	...	...	1	3.57×10^{-4}	0.026	0
...	0.4	0.9580	1.440	0.1	3.57×10^{-5}	0.0026	1
...	...	...	...	1	3.57×10^{-4}	0.026	2
...	0.5	0.9773	1.348	0.1	3.57×10^{-5}	0.0026	0
...	...	...	...	1	3.57×10^{-4}	0.026	3
...	0.6	0.99991	2.328	0.1	3.57×10^{-5}	0.0026	14
...	...	...	...	1	3.57×10^{-4}	0.026	14
...	0.7	0.99998	3.0312	0.1	3.57×10^{-5}	0.0026	32
...	...	...	...	1	3.57×10^{-4}	0.026	32
...	0.9	1.0	3.125	0.1	3.57×10^{-5}	0.0026	58
...	...	...	...	1	3.57×10^{-4}	0.026	59

Notes

Disks with $M_{\text{disk}} \gtrsim 6 \times 10^3 M_\odot$ and initial eccentricity $e_{\text{disk}} \gtrsim 0.6$ produce very high eccentricities, possibly leading to tidal disruptions of binaries.

[a] Mean of highest five eccentricities reached during simulation.

[b] Mean of highest five inclinations (in radians).

[c] Percentage of stars that enter the tidal radius.

well-defined clockwise disk of O and Wolf-Rayet (WR) stars, and a group of counter-clockwise moving O and WR stars, possibly a dissolving second disk (Levin & Beloborodov 2003; Nayakshin & Cuadra 2005; Genzel et al. 2003; Paumard et al. 2006; Lu et al. 2008; Bartko et al. 2008). These O and WR stars are located at projected distances of 0.05 pc to 0.5 pc, and were most likely formed as a result of gravitational fragmentation of a gaseous disk (Levin & Beloborodov 2003). More puzzling in terms of origin is the population of B-stars known as the ‘S-stars’ (Schödel et al. 2002; Ghez et al. 2005; Eisenhauer et al. 2005; Gillessen et al. 2009). At distances of 0.003–0.03pc from the SMBH, in-situ formation seems highly improbable due to the tidal field of SgrA* (Levin 2007). In addition, their young age ($\sim 20{-}100$ Myr) imposes a tight constraint on formation scenarios in that they cannot have travelled far from their place of birth. One possibility is the formation of the S-stars from the disruption of stellar binaries (Hills 1988; Gould & Quillen 2003). Perets et al. (2007) propose the surrounding stellar bulge as the source of the binaries, while Löckmann, Baumgardt, & Kroupa (2008) (LBK) invoke two stellar disks in the Galactic center to explain the origin. In their simulations the stars experienced Kozai-type torques which induced strong changes in their inclination and eccentricity. The eccentricity of many of the stars became greater than 0.9, and LBK argued that if these stars were binaries they would be tidally disrupted by the SMBH, thus producing the S-stars and high-velocity stars via Hills' (1988) mechanism.

However, the gravitational influence of a stellar cusp, which was neglected by LBK, strongly suppresses Kozai-type dynamics. This was recently discussed in Chang (2009). Chang's treatment was highly simplified; in particular, his expressions for Kozai evolution were valid only if the stellar orbits were inside the inner edges of both disks. We have performed LBK-type simulations and have confirmed Chang's general conclusion that a realistically massive stellar cusp entirely suppresses the production of high-eccentricity stars via a Kozai-type mechanism.

In contrast, the eccentricity instability is capable of driving several stars to near-radial orbits, as is evident in Figure (2.1). For capture, the pericenter r_p of the binary's orbit must come within the tidal radius $r_t = (2M_\bullet/m_{\rm bin})^{1/3}a_{\rm bin}$. This results in a captured star with semi-major axis $a_\bullet$ that scales as $a_\bullet \sim (M_\bullet/m_{\rm bin})^{2/3}a_{\rm bin}$, where $a_{\rm bin}$ is the semi-major axis of the binary itself, $m_{\rm bin}$ is its combined mass and the eccentricity of the captured star can be approximated as $1-e \sim (m_{\rm bin}/M_\bullet)^{1/3}$.

We summarize our results for varying masses and initial eccentricities of the disk in Table (2.1). All simulations have evolved for $\sim$ 7 Myr. For a given semi-major axis of a binary system, we calculate the tidal radius at which the binary will be disrupted and finally the percentage of stars that come within this radius. It is clear that for many parameters of our disk, stars have $r_p < r_t$. For example, a disk with an initial eccentricity of 0.6 and mass of $10^4 M_\odot$, 14 % of stars in the disk will enter the tidal radius. Thus, if some of these stars are binaries, Hills' mechanism for producing the S- and high-velocity stars (Brown et al. 2006) could be at work. An important element in this scenario is the binary survival rate at the radii of the disk; however, Perets (2009) show that for $a = 0.1\,\mathrm{AU}$ the evaporation rate is $> 10^7\,\mathrm{yr}$.

The scalar resonant relaxation time in the Galactic center is everywhere larger than the age of the disks. It follows that since the post-capture eccentricity of the stars is of order $1-e \approx 10^{-2}$, most of the S-stars cannot have formed in the *current* disk. The lifetime of many S-stars could be of the order of 100 Myr, and thus earlier ($\sim 10-100$ Myr) starburst episodes could have contributed to their present population. In that case, the scalar relaxation time is short enough to randomize the eccentricities (Hopman & Alexander 2006a; Perets et al. 2009). We note that the scenario presented by LBK has the same limitation.

2.5.1 Bimodal eccentricity distribution in disk

In Figure (2.3) we compare the observed stellar eccentricity distribution of the clock-wise disk (Bartko et al. 2008) with the simulated post-instability ec-

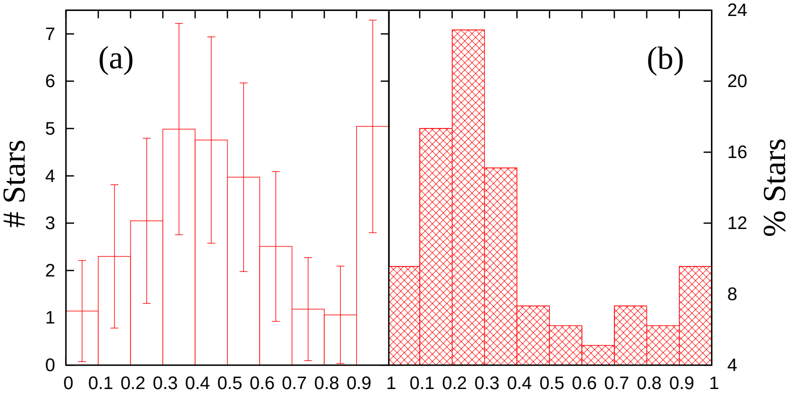

Figure 2.3 – (a) Observed eccentricity distribution of clock-wise stellar disk in the Galactic center, reproduced with permission from Bartko et al. (2008). (b) Simulated distribution for a disk with an initial eccentricity of 0.6 and $M_{\rm disk} = 10^4$ after 5.7 Myr. Both the observed and simulated eccentricity distributions exhibit bimodality.

centricity distribution for all stars with an initial disk eccentricity of 0.6 (c.f. Bonnell & Rice 2008). We draw attention to the qualitative similarities in the two plots, in particular the double-peaked profile. This bimodality is a natural consequence of the eccentric disk instability as all eccentricities are driven away from the mean. Without the instability it is unclear how to generate such a distribution.

2.6 Critical discussion

So far, we have described the eccentricity instability for an idealized initial disk configuration. We now demonstrate the effectiveness of the instability for a broader scope of parameters and extend our disk model to include (1) a significant range in both magnitude and direction of the stellar eccentricity vectors, (2) heavily inclined stellar orbits, and (3) different values of γ, the power-law index of the cusp, which determines the precession rate within the disk. We discuss each of these in turn.

(1) We simulate disks with initial eccentricity vectors scattered between a range of opening angles $\theta \in [0, 2\pi]$. As anticipated, significant spreading of the vector decreases the effectiveness of the instability. However, we find sufficiently high eccentricity orbits to generate S-stars up to $\theta \sim \pi\,\mathrm{radians}$, which suggests that the instability remains important for substantially less favorable circumstances. Next we vary the magnitudes of the eccentricities throughout the disk, basing our initial conditions on Run 1 and 2 of Bonnell & Rice (2008). Run 1 (0.6 $< e <$ 0.7) is in excellent agreement with our previous results. The instability in Run 2 (0 $< e <$ 0.6) however, is not efficient at generating the

highest e orbits and hence the S-stars. These conclusions are transparent; the stars which experience the greatest torque are those at small a (see Section 2.3) and if initially circular, need a greater torque to produce the highest e orbits. We find that the most important condition, for $M_{\rm disk} = 10^4$, is for innermost orbits to have $e > 0.4$. Future work on gas dynamics of eccentric disks will tell whether this presents a serious problem for our scenario.

(2) We study disks with stellar rms inclinations in the range $[0, 0.3]$ and find that the instability is robust in all cases. However, above the limit 0.2, the instability appears ineffective in generating the highest e ($> 1 - 10^{-3}$) orbits.

(3) We vary the power-law slope of the cusp. For $\gamma < 3/2$, due to the shallowness of the cusp, the innermost orbits lag behind in precession and are more susceptible to being pushed to high e orbits. While this improves the ability of the instability to produce S-stars, the instability is not as effective at generating low e orbits. Conversely, an increase in γ ($> 3/2$) results in the innermost orbits precessing faster than the bulk of the stars and hence suppresses the generation of the highest e orbits and lengthens the time-scale on which it occurs. We conclude that the production of S-stars is unlikely for a cusp with $\gamma > 7/4$. In all cases examined ($1 < \gamma < 2$), the instability proves robust and, as emphasized in Section 2.2, there is both observational and theoretical evidence that the slope of the cusp in the Galactic center is sufficiently close to $3/2$ for the instability to be highly effective.

The eccentricity instability described in this work is relevant for an eccentric disk embedded in a stellar cusp. We note that the instability is not directly applicable for the eccentric disk in M31 (Tremaine 1995) as the mass of the disk is much greater than the mass of the stellar bulge enclosed within the same radius. Indeed we find that such a disk remains coherent over several precession times, although the innermost stars can undergo significant angular momentum changes as described by Cuadra et al. (2008). The situation is different in the Galactic center, where massive stars were likely born from an eccentric gaseous disk, and where there is strong observational evidence for a heavy spherical stellar cusp (Genzel et al. 2003; Schödel et al. 2007). We have shown that the instability may have strongly influenced the development of the eccentricities of the massive stars observed, and in particular, can account for the bimodality in their eccentricity distribution. Furthermore, combined with Hills' (1988) mechanism, the eccentricity instability may have played a role in the formation of the S-stars and of the high-velocity stars in the Galactic halo.

Acknowledgments We thank Atakan Gürkan, Richard Alexander, Simon Portegies Zwart, Mher Kazandjian, Jihad Touma and Sergei Nayakshin for useful discussions, and Mark Hayden for comments on the text. AM is supported by a TopTalent fellowship from the Netherlands Organization for Scientific Research (NWO), YL by a Vidi fellowship from NWO and CH by a Veni fellowship from NWO.

References

Alexander, T. 1999, ApJ, 527, 835

Alexander, T., & Hopman, C. 2008, ArXiv e-prints, astro-ph/0808.3150

Alexander, R. D., Armitage, P. J., Cuadra, J., & Begelman, M. C. 2008, ApJ, 674, 927

Bahcall, J. N., & Wolf, R. A. 1976, ApJ, 209, 214

Bartko, H., Martins, F., Fritz, T. K., Genzel, R., Levin, Y., Perets, H. B., Paumard, T., Nayakshin, S., et al., 2008, eprint arXiv, 0811., 3903

Binney, J. & Tremaine, S. 2008, Galactic Dynamics (Princeton University Press)

Bonnell, I. A. & Rice, W. K. M. 2008, Science, 321, 1060

Brown, W. R., Geller, M. J., Kenyon, S. J., & Kurtz, M. J. 2006, ApJ, 647, 303

Chang, P. 2009, MNRAS, 393, 224

Cuadra, J., Armitage, P. J., & Alexander, R. D. 2008, MNRAS, 388, L64

Danby 1992, "Fundamentals of celestial mechanics", (Richmond: Willman-Bell, |c1992, 2nd ed.,)

Dehnen, W. 2001, MNRAS, 324, 273

Eilon, E., Kupi, G., & Alexander, T. 2008, eprint arXiv, 0807., 1430

Eisenhauer, F., Genzel, R., Alexander, T., Abuter, R., Paumard, T., Ott, T., Gilbert, A., Gillessen, et al., 2005, ApJ, 628, 246

Genzel, R., Schödel, R., Ott, T., Eisenhauer, F., Hofmann, R., Lehnert, M., Eckart, A., Alexander, T., et al., 2003, ApJ, 594, 812

Ghez, A. M., Salim, S., Hornstein, S. D., Tanner, A., Lu, J. R., Morris, M., Becklin, E. E., & Duchêne, G. 2005, ApJ, 620, 744

Ghez, A. M., Salim, S., Weinberg, N. N., Lu, J. R., Do, T., Dunn, J. K., Matthews, K., Morris, M. R., et al., 2008, ApJ, 689, 1044

Gillessen, S., Eisenhauer, F., Trippe, S., Alexander, T., Genzel, R., Martins, F., & Ott, T. 2009, ApJ, 692, 1075

Gould, A. & Quillen, A. C. 2003, ApJ, 592, 935

Gürkan, M. A. & Hopman, C. 2007, MNRAS, 379, 1083

Hills, J. G. 1988, Nature, 331, 687

Hobbs, A. & Nayakshin, S. 2009, MNRAS, 394, 191

Hopman, C. & Alexander, T. 2006a, ApJ, 645, L133

—. 2006b, ApJ, 645, 1152

Kormendy, J. 2004, Coevolution of Black Holes and Galaxies, 1, ISBN: 0521824494

Levin, Y. 2007, MNRAS, 374, 515

Levin, Y. & Beloborodov, A. M. 2003, ApJ, 590, L33

Löckmann, U., Baumgardt, H., & Kroupa, P. 2008, ApJ, 683, L151

Lu, J. R., Ghez, A. M., Hornstein, S. D., Morris, M. R., Becklin, E. E., & Matthews, K. 2008, ApJ, accepted

Nayakshin, S. & Cuadra, J. 2005, A&A, 437, 437

Paumard T., Genzel R., Martins F., et al., 2006, ApJ, 643, 1011

Perets, H. B., Hopman, C., & Alexander, T. 2007, ApJ, 656, 709

Perets, H. B. 2009, The Astrophysical Journal, 690, 795

Perets, H. B., Gualandris, A., Kupi, G., Merritt, D., & Alexander, T. 2009, eprint arXiv, 0903, 2912

Polyachenko, V. L., Polyachenko, E. V., & Shukhman, I. G. 2008, Astronomy Letters, 34, 163

Polyachenko, V. L. & Shukhman, I. G. 1981, Soviet Astronomy (tr. astr. Zhurn.) V. 25, 25, 533

Rauch, K. P. & Ingalls, B. 1998, MNRAS, 299, 1231
Rauch, K. P. & Tremaine, S. 1996, New Astronomy, 1, 149
Sanders, R. H. 1998, MNRAS, 294, 35
Schödel, R., Eckart, A., Alexander, T., Merritt, D., Genzel, R., Sternberg, A., Meyer, L., Kul, F., et al., A&A, 469, 125
Schödel, R., Ott, T., Genzel, R., Hofmann, R., Lehnert, M., Eckart, A., Mouawad, N., Alexander, T., et al., Nature, 419, 694
Touma, J. R., Tremaine, S., & Kazandjian, M. V. 2009, MNRAS, 194, 2009
Tremaine, S. 1995, AJ, 110, 628
—. 2005, ApJ, 625, 143
Wisdom, J. & Holman, M. 1991, AJ, 102, 1528
Young, P. 1980, ApJ, 242, 1232
Yoshida, H. 1990, Physics Letters A, 150, 262

3

Secular Stellar Dynamics near Massive Black Holes

The angular momentum evolution of stars close to massive black holes (MBHs) is driven by secular torques. In contrast to two-body relaxation, where interactions between stars are incoherent, the resulting resonant relaxation (RR) process is characterized by coherence times of hundreds of orbital periods. In this chapter, we show that all the statistical properties of RR can be reproduced in an autoregressive moving average (ARMA) model. We use the ARMA model, calibrated with extensive N-body simulations, to analyze the long-term evolution of stellar systems around MBHs with Monte Carlo simulations.

We show that for a single-mass system in steady-state, a depression is carved out near an MBH as a result of tidal disruptions. Using Galactic center parameters, the extent of the depression is about 0.1 pc, of similar order to but less than the size of the observed "hole" in the distribution of bright late-type stars. We also find that the velocity vectors of stars around an MBH are locally not isotropic. In a second application, we evolve the highly eccentric orbits that result from the tidal disruption of binary stars, which are considered to be plausible precursors of the "S-stars" in the Galactic center. We find that RR predicts more highly eccentric ($e > 0.9$) S-star orbits than have been observed to date.

Ann-Marie Madigan, Clovis Hopman and Yuri Levin
The Astrophysical Journal 738, 99 (2011)

3.1 Introduction

The gravitational potential near a massive black hole (MBH) is approximately equal to that of a Newtonian point particle. As a consequence, the orbits of stars are nearly Keplerian, and it is useful, both as a mental picture and as a computational device, to average the mass of the stars over their orbits and consider secular interactions between these ellipses, rather than interactions between point particles. These stellar ellipses precess on timescales of many orbits, due to deviations from the Newtonian point particle approximation: there is typically an extended cluster of stars around the MBH, and there is precession due to general-relativistic (GR) effects. Nevertheless, for timescales less than a precession time, torques between the orbital ellipses are coherent.

It was first shown by Rauch & Tremaine (1996) that such sustained coherent torques lead to much more rapid stochastic evolution of the angular momenta of the stars than normal relaxation dynamics. They called this process resonant relaxation (RR). RR is potentially important for a number of astrophysical phenomena. Rauch & Ingalls (1998) showed that it increases the tidal disruption rate, although in their calculations the effect was not very large since most tidally disrupted stars originated at distances that were too large for RR to be effective (in Section 3.7.2 we will revisit this argument). By contrast with tidally disrupted main-sequence stars, inspiraling compact objects originate at distances much closer to the MBH (Hopman & Alexander 2005). The effect of RR on the rate of compact objects spiralling into MBHs to become gravitational wave sources is therefore much larger (Hopman & Alexander 2006). RR also plays a role in several proposed mechanisms for the origin of the “S-stars”, a cluster of B-stars with randomized orbits in the Galactic center (GC; e.g. Hopman & Alexander 2006; Levin 2007; Perets et al. 2007, see Section 3.7.3 of this chapter).

There have been several numerical studies of the RR process itself, which have verified the overall analytic predictions. However, since stellar orbits in N-body simulations (e.g. Rauch & Tremaine 1996; Rauch & Ingalls 1998; Aarseth 2007; Harfst et al. 2008; Eilon et al. 2009; Perets et al. 2009; Perets & Gualandris 2010) need to be integrated for many precession times, the simulations are computationally demanding. All inquiries have thus far have been limited in integration time and/or particle number. In order to speed up the computation, several papers have made use of the picture described above, where the gravitational interaction between massive wires are considered (Gauss’s method, see e.g. Rauch & Tremaine 1996; Gürkan & Hopman 2007; Touma et al. 2009). It is common, when possible, to use the the Fokker-Planck formalism to carry out long-term simulations of the stellar distribution in galactic nuclei (Bahcall & Wolf 1976, 1977; Lightman & Shapiro 1977; Murphy et al. 1991; Hopman & Alexander 2006,b). The current formalism however is not directly applicable to the case when RR plays an important role. At the heart of all current Fokker-Plank approaches is the assumption of a random-walk diffusion of angular momentum, whereas RR is a more complex relaxation mechanism based on persistent autocorrelations.

In this work, we will show that the *auto-regressive moving average* (ARMA) model provides a faithful representation of all statistical properties of RR. This model, calibrated with special-purpose N-body simulations, allows us to carry out a study of the long-term effects of RR on the stellar cusp, thus far out of reach.

The plan of the chapter is as follows. In Section 3.2, we present an extensive suite of special purpose N-body simulations, which exploit the near-Keplerian nature of stellar orbits and concentrate on the stochastic orbital evolution of several test stars. We use these simulations to statistically examine the properties of RR for many secular timescales. In Section 3.3, we introduce the ARMA model for the data analysis of the N-body simulations. This description accommodates the random, non-secular (non-resonant) effects on very short timescales, the persistent autocorrelations for intermediate timescales less than a precession time, and the random walk behavior for very long times (the RR regime). In Section 3.4 we extend the ARMA model, using physical arguments, to a parameter space that is larger than that of the simulations. In Section 3.5 we calibrate the parameters using the results of the N-body simulations. Once the free parameters of the ARMA model are determined, we then use them in Section 3.6 as an input to Monte Carlo (MC) simulations which study the distribution of stars near MBHs. In Section 3.7 we show that RR plays a major role in the global structure of the stellar distribution near MBHs, and in particular for the young, massive B-type stars near the MBH (the "S-stars") in our GC. We summarize in Section 3.8.

3.2 N-body simulations

We have developed a special-purpose N-body code, designed to accurately integrate stellar orbits in near-Keplerian potentials; see Appendix 3.A for a detailed description. We wrote this code specifically for the detailed study of RR. Such a study requires an integration scheme with an absence of spurious apsidal precession and one which is efficient enough to do many steps per stellar orbit while integrating many orbits to resolve a secular process. The main features of this code are the following:

1. A separation between test particles and field particles. Field particles move on Kepler orbits, which precess due to their averaged potential and general relativity, and act as the mass that is responsible for dynamical evolution. Test particles are full N-body particles and serve as probes of this potential (Rauch & Tremaine 1996; Rauch & Ingalls 1998).
2. The use of a fourth-order mixed-variable symplectic (MVS) integrator (Yoshida 1990; Wisdom & Holman 1991; Kinoshita et al. 1991; Saha & Tremaine 1992). The MVS integrator switches between Cartesian coordi-

nates (in which the perturbations to the orbit are calculated) to one based on Kepler elements (to calculate the Keplerian motion of the particle under the influence of central object). We make use of Kepler's equation (see, e.g., Danby 1992) for the latter step.

3. Adaptive time stepping and gravitational softening. To resolve the periapsis of eccentric orbits (Rauch & Holman 1999) and close encounters between particles, we adapt the time steps of the particles. We use the compact K_2 kernel (Dehnen 2001) for gravitational softening.
4. Time symmetric algorithm. As MVS integrators generally lose their symplectic properties if used with adaptive time stepping, we enhance the energy conservation by time-symmetrizing the algorithm.

Our code is efficient enough to study the evolution of energy and angular momentum of stars around MBHs for many precession times, for a range of initial eccentricities.

3.2.1 Model of Galactic nucleus

We base our Galactic nucleus model on a simplified GC template[1]. It has three main components. (1) An MBH with mass $M_\bullet = 4 \times 10^6 M_\odot$ which remains at rest in the center of the coordinate system. (2) An embedded cluster of equal-mass field stars $m = 10\ M_\odot$, distributed isotropically from $0.003\,\mathrm{pc}$ to $0.03\,\mathrm{pc}$, which follow a power-law density profile $n(r) \propto r^{-\alpha}$. The outer radius is chosen with reference to Gürkan & Hopman (2007), who show that stars with semi-major axes larger than the test star's apoapsis distance $r_{\mathrm{apo}} = a(1+e)$ contribute a negligible amount of the net torque on the test star. The field stars move on precessing Kepler orbits, where the precession rate is determined by the smooth potential of the field stars themselves (see Appendix 3.C) and general relativity. The precession of the field stars is important to account for because for some eccentricities the precession rate of the test star is much lower than that of the "typical" field star, such that it is the precession of the latter that leads to decoherence of the system. The field stars do not interact with each other but they do interact with the test stars if the latter are assumed to be massive. In this way the field stars provide the potential of the cluster but are not used as dynamic tracers. (3) A number of test stars, used as probes of the background potential, that are either massless or have the same mass as the field stars, $m = 10 M_\odot$. We consider both massless and massive stars in order to study the effects of resonant friction (Rauch & Tremaine 1996). The test stars have semi-major axes of $a = 0.01\,\mathrm{pc}$ and a specified initial eccentricity e.

Following Equation (17) from Hopman & Alexander (2006), who use the $M_\bullet - \sigma$ relation (Ferrarese & Merritt 2000; Gebhardt et al. 2000) which correlates the mass of a central black hole with the velocity dispersion of the host

---

[1] Due to the effect of GR precession, the system is not scale-free and the masses need to be specified.

Table 3.1 – Galactic Nucleus Model

Parameter	Numerical Value
$M_\bullet$	$4 \times 10^6 M_\odot$
m	$10\ M_\odot$
α	1.75
r_h	2.31 pc
$r_{\rm min}$	0.003 pc
$r_{\rm max}$	0.03 pc
$a_{\rm teststar}$	0.01 pc
$N(< r_{\rm max})$	1754

galaxy's bulge, we define the radius of influence as

$$r_h = \frac{GM_\bullet}{\sigma^2} = 2.31\ \mathrm{pc} \left(\frac{M_\bullet}{4 \times 10^6 M_\odot} \right)^{1/2} . \qquad (3.1)$$

The number of field stars within radius r is

$$N(< r) = N_h \left(\frac{r}{r_h} \right)^{3-\alpha} , \qquad (3.2)$$

where we assume that the mass in stars within r_h equals that of the MBH, $N_h = M_\bullet / m = 4 \times 10^5$. We take $\alpha = 7/4$ (Bahcall & Wolf 1976), the classic result for the distribution of a single-mass population of stars around an MBH, which relies on the assumption that the mechanism through which stars exchange energy and angular momentum is dominated by two-body interactions. Hence the number of field stars within our model's outer radius is $N(< 0.03\ \mathrm{pc}) = 1754$. We summarize the potential for our Galactic nucleus model in Table 3.1.

We evolve this model of a galactic nucleus for a wide range in eccentricity of the test stars, $e = 0.01, 0.1, 0.2, 0.3, 0.4, 0.6, 0.8, 0.9$ and 0.99. For each initial eccentricity, we follow the evolution of a total of 80 test stars, both massless and massive, in a galactic nucleus. Typically we use four realizations of the surrounding stellar cluster for each eccentricity, i.e., 20 test stars in each simulation. They have randomly oriented orbits with respect to one another, so that they experience different torques within the same cluster. The simulations are terminated after 6000 orbital periods (henceforth denoted by $P = 2\pi \sqrt{a^3 / GM_\bullet}$) at $a = 0.01\,\mathrm{pc}$, roughly equivalent to three precession times for a star of eccentricity $e = 0.6$, deep into the RR regime for all eccentricities, meaning that several coherence timescales have passed; see Section 3.5 for verification. Using our method of analysis, it would not be useful for our simulations to run for longer times as the stars would move significantly away from their initial eccentricities. In addition, the autocorrelation functions (ACFs) of their angular momentum changes drop to zero before this time; see Figure 3.4.

3.2.2 Illustrative simulations

In Section 3.3, we present a description that captures all the relevant statistical properties of RR, and in particular has the correct autocorrelations. Here we consider several individual simulations for illustration purposes, in order to highlight some interesting points and motivate our approach. We define energy E of the test star as

$$E = \frac{GM_\bullet}{2a}, \tag{3.3}$$

and dimensionless angular momentum[2] J as

$$J = \sqrt{1-e^2}. \tag{3.4}$$

Secular torques should affect the angular momentum evolution, but not the energy evolution of the stars (in the picture of interactions between massive ellipses of the introduction, the ellipses are fixed in space for times less than a precession time, $t < t_{\rm prec}$, such that the potential and therefore the energy is time-independent). It is therefore of interest to compare the evolution of these two quantities. An example is shown in Figure 3.1. As expected, the angular momentum evolution is much faster than energy evolution; furthermore, the evolution of angular momentum is much less erratic, which visualizes the long coherences between the torques.

In Figure 3.2 we show the eccentricity evolution for a sample population of stars with various initial orbital eccentricities. There is significant eccentricity evolution in most cases, but almost none for $e = 0.99$, the reasons for which we elucidate in Section 3.6.

To quantify the rate at which the energy E and angular momentum J change as a function of eccentricity e, we calculate the E and J relaxation timescales. We define these as the timescale for order of unity (circular angular momentum) changes in energy E (angular momentum J). We compute the following quantities:

$$t_E = \frac{E^2}{\langle(\Delta E)^2\rangle}\Delta t, \tag{3.5}$$

$$t_J = \frac{J_c^2}{\langle(\Delta J)^2\rangle}\Delta t, \tag{3.6}$$

where ΔE and ΔJ are the steps taken in a time Δt, and we take the mean $\langle\,\rangle$ over 80 test stars in each eccentricity bin.

We plot the resulting timescales as a function of eccentricity in Figure 3.3, taking several Δt values to get order-of-magnitude estimates for these timescales. We find no significant difference between the results for the massless and massive test stars. We note that t_E is only weakly dependent on e, whereas t_J is

---

[2] Throughout this chapter, we use units in which angular momentum J and torque τ are normalized by the circular angular momentum for a given semi-major axis, $J_c = \sqrt{GM_\bullet a}$. All quantities are expressed per unit mass.

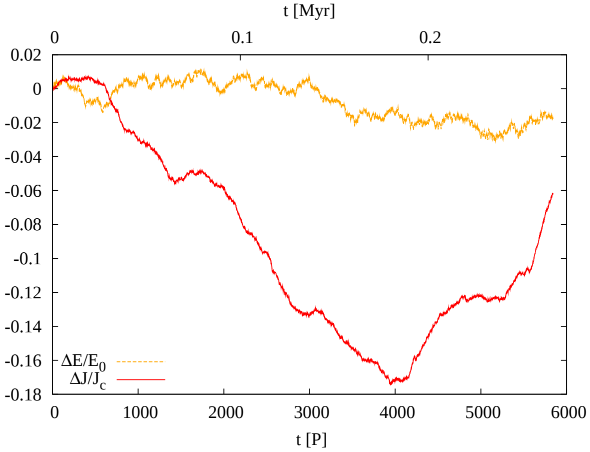

Figure 3.1 – Evolution of angular momentum J and energy E, normalized to the initial values, of a massless test star with semi-major axis $a = 0.01$ pc and eccentricity $e = 0.6$. Time is in units of the initial orbital period P (top axis shows time in Myr). The coherence of RR can be seen in the J evolution (precession time $t_{\rm prec}$ is ~ 2000 orbits), whereas the E evolution displays a much slower, more erratic, random walk.

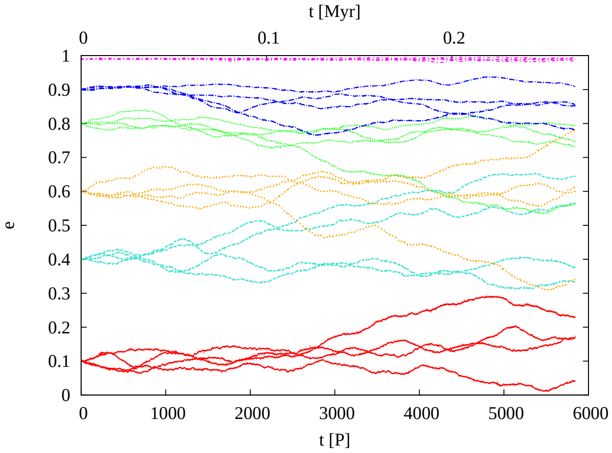

Figure 3.2 – Eccentricity evolution of a sample of massless test stars in a fiducial galactic nucleus model. We show four realizations for five different initial eccentricities. Evolution is rapid for most eccentricities; however, the stars with the highest value $e = 0.99$ have sluggish eccentricity evolution.

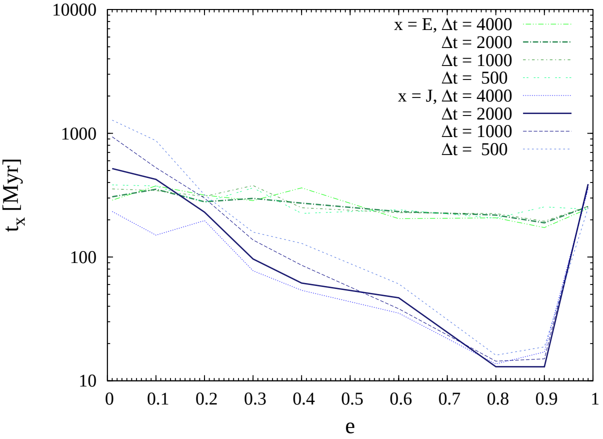

Figure 3.3 – Timescale for order of unity (circular angular momentum) changes in energy E (angular momentum J) for massless test stars in our N-body simulations, presented on a log scale of time in units of Myr; see Equations (3.5) and (3.6). We find a weak trend for lower E relaxation times with increasing eccentricity (from $\sim 400\,\mathrm{Myr}$ to $200\,\mathrm{Myr}$). J relaxation occurs on very short timescales ($\sim 20\,\mathrm{Myr}$) at eccentricities of $0.8 < e < 0.9$. Stellar orbits with low eccentricities have very long J relaxational timescales ($\sim 1\,\mathrm{Gyr}$) as the torque on a circular orbit drops to zero. This timescale increases again at very high eccentricities.

of the same order of magnitude as t_E for $e \to 0$ and $e \to 1$, but much smaller for intermediate eccentricities. It is in the latter regime that secular torques are dominating the evolution. In the following sections, we will give a detailed model for the evolution of angular momentum. Since the focus of this chapter is mainly on secular dynamics, we do not further consider energy diffusion here, but in Appendix 3.B we discuss the timescale for cusp formation due to energy evolution, and compare our results to other results in the literature.

3.3 Statistical description of resonant relaxation

As a result of the autocorrelations in the changes of the angular momentum of a star, as exhibited in Figure 3.1, RR cannot be modeled as a random walk for all times. This is also clear from physical arguments. Rauch & Tremaine (1996) and several other papers take the approach of considering two regimes of evolution: for times $t \ll t_{\mathrm{prec}}$, evolution is approximately linear as the torques continue to point in the same direction. For times $t \gg t_{\mathrm{prec}}$, the torque autocorrelations vanish and it becomes possible to model the system as a random walk. Here we introduce a new approach, which unifies both regimes in a single description. This description is also useful as a way of quantifying the statistical properties of RR.

We study the evolution of the angular momenta of the test stars using a time series of angular momenta at a regular spacing of one period. This choice

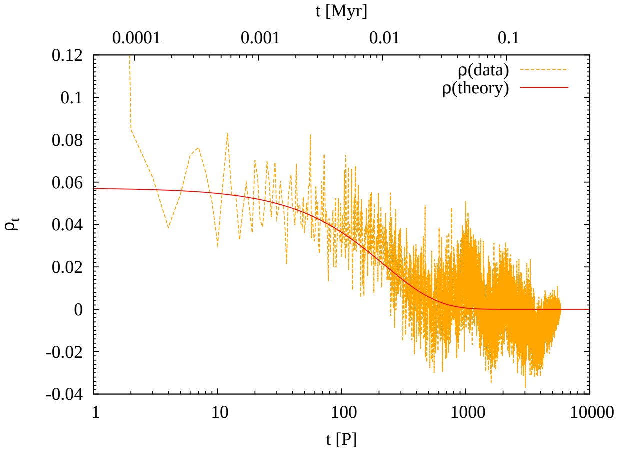

Figure 3.4 – Autocorrelation function for the differences ΔJ in one particular simulation (noisy orange line) as a function of time in units of the initial orbital period P. The test star is massless and has initial eccentricity $e = 0.6$. The autocorrelation function is significantly larger than zero (if much less than one) for several hundred orbits. The smooth red line gives the theoretical ACF for an ARMA(1, 1) model with $\phi_1 = 0.995$, $\theta_1 = -0.976$.

is arbitrary, and below we show how our results generalize to any choice of time steps. The normalized ACF can be written as

$$\rho_t = \frac{\langle(\Delta J_{s+t} - \langle \Delta J\rangle)(\Delta J_s - \langle \Delta J\rangle)\rangle}{\langle(\Delta J_s - \langle \Delta J\rangle)^2\rangle}, \tag{3.7}$$

where ΔJ_s is the change in angular momentum between subsequent measurements at time s and it is assumed that the time series is stationary. A typical ACF from our simulations is shown in Figure 3.4. The fundamental feature of this ACF is that it is significantly larger than zero for hundreds of orbits, but with values much less than unity.

Our goal in this section is to define a process that generates a time series that has the same ACF as that of the changes in angular momentum of a star. Such a time series has all the statistical properties that are relevant for the angular momentum evolution of the star, such as the same Fourier spectrum. We have two motivations for doing this. First, defining such a process implies that once the parameters of the model are calibrated by use of the N-body simulations, RR is fully defined – as it is a random Gaussian process that is also stationary, for sufficiently short times, and as such is entirely described by its ACF. Second, a generated time series with the same statistical properties as the time series generated in the physical process can be used in MC simulations to solve for the long term evolution of RR.

3.3.1 The autoregressive moving average model ARMA(1, 1)

We now introduce the ARMA model, which is often used in econometrics (see, e.g., Heij et al. 2004). We show that this model can generate time series that reproduce the ACF and variance of ΔJ_t. The model is ad hoc in that it does not have a direct physical foundation. However, we will find physical interpretations for the free parameters of the model in Section 3.4. We use a form of the model, ARMA(1,1), with one autoregressive parameter, ϕ_1, and one moving average parameter, θ_1. The model can then be written as

$$\Delta_1 J_t = \phi_1 \Delta_1 J_{t-1} + \theta_1 \epsilon^{(1)}_{t-1} + \epsilon^{(1)}_t. \tag{3.8}$$

The label "1" in this equation refers to the fact that the data have a regular spacing of one period. In this equation, ϕ_1 and θ_1 are free parameters, and the random variable ϵ is drawn from a normal distribution with

$$\langle \epsilon^{(1)} \rangle = 0; \quad \langle \epsilon^{(1)}_t \epsilon^{(1)}_s \rangle = \sigma_1^2 \delta_{ts} \tag{3.9}$$

where σ_1 is a third free parameter and δ_{ts} is the Kronecker delta. For such a model, the variance of the angular momentum step is

$$\langle \Delta J_t^2 \rangle = \frac{1 + \theta_1^2 + 2\theta_1\phi_1}{1 - \phi_1^2} \sigma_1^2, \tag{3.10}$$

and the ACF can be derived analytically (see Appendix 3.D for details):

$$\rho_t = \phi_1^t \left[1 + \frac{\theta_1/\phi_1}{1 + (\phi_1 + \theta_1)^2/(1 - \phi_1^2)} \right] \qquad (t > 0). \tag{3.11}$$

From this expression, we see that the decay time of the ACF is determined by the parameter ϕ_1, and θ_1 captures the magnitude of the ACF. As an example, we plot the ACF in Figure 3.4 with parameters typical for RR. We emphasize the need for both an autoregressive parameter and a moving average parameter to reproduce the slow decay of the ACF. Neither parameters can replicate the features on their own.

A useful reformulation of the ARMA(1, 1) model, which can be found using recursion, is

$$\Delta J_t = \sum_{k=0}^{\infty} \psi_k \epsilon_{t-k}, \tag{3.12}$$

where

$$\psi_k = (\phi_1 + \theta_1)\phi_1^{k-1} \quad (k > 0); \quad \psi_0 = 1. \tag{3.13}$$

Once the model parameters $(\phi_1, \theta_1, \sigma_1)$ are found for a time step of one period, $\delta t = P$, the variance after N steps can be computed. The displacement after N steps is given by

$$\sum_{n=1}^{N} \Delta J_n = \sum_{n=1}^{N} \sum_{k=0}^{\infty} \psi_k \epsilon_{n-k}, \tag{3.14}$$

where $(n-k) \geq 0$. We denote the variance of the displacement after N steps by

$$V(N) \equiv \left\langle \left(\sum_{n=1}^{N} \Delta J_n \right)^2 \right\rangle , \tag{3.15}$$

such that

$$\begin{aligned} V(N) &= \sum_{n=1}^{N} \sum_{k=0}^{\infty} \sum_{m=1}^{N} \sum_{l=0}^{\infty} \psi_k \psi_l \langle \epsilon_{n-k} \epsilon_{m-l} \rangle \\ &= \sigma_1^2 \sum_{n=1}^{N} \sum_{k=0}^{\infty} \sum_{m=1}^{N} \sum_{l=0}^{\infty} \psi_k \psi_l \delta_{n-k,m-l} , \end{aligned} \tag{3.16}$$

which can be decomposed as

$$\begin{aligned} V(N)\sigma_1^{-2} = N + \sum_{m=2}^{N} \sum_{n=1}^{m-1} \psi_{m-n} + \sum_{k=1}^{N-1} \psi_k (N-k) \\ + \sum_{k=1}^{\infty} \sum_{m=1}^{N} \sum_{n=1}^{\min(k+m-1,N)} \psi_k \psi_{k+m-n} . \end{aligned} \tag{3.17}$$

This expression can be cast in a form without summations by repeatedly using the properties of the independent normal random variables ϵ_t in Equation (3.9), resulting after some algebra in

$$\begin{aligned} V(N)\sigma_1^{-2} = N + \frac{\phi_1 + \theta_1}{1-\phi_1} \left[2N - 1 + \frac{2\phi_1^N - \phi_1 - 1}{1-\phi_1} \right] \\ + \left(\frac{\phi_1 + \theta_1}{1-\phi_1} \right)^2 \left[N - 2\frac{\phi_1 (1-\phi_1^N)}{1-\phi_1^2} \right] . \end{aligned} \tag{3.18}$$

Note that in the special case that $N = 1$, Equation (3.10) is recovered. We plot this expression in Figure 3.5.

Three characteristic timescales are clearly discernible in this figure. On a short timescale, the angular momentum diffusion is dominated by the usual two-body gravitational scattering (i.e., non-resonant relaxation, hereafter NR). In this regime the angular momentum deviation scales as $\sqrt{t}$. On an intermediate timescale the orbital angular momentum evolves due to the nearly constant orbit-averaged secular torques from the other stellar orbits, and thus the angular momentum deviation scales linearly with time. On a yet longer timescale the secular torques fluctuate due to orbital precession, and the $\sqrt{t}$ scaling is reinstated, albeit with a much higher effective diffusion coefficient. Thus the ARMA-driven evolution is in agreement with what is expected for a combination of RR and NR acting together; see also Rauch & Tremaine (1996) and Eilon et al. (2009) for discussion.

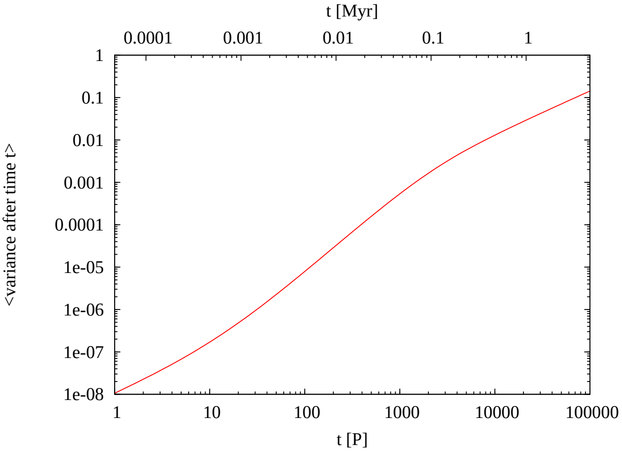

Figure 3.5 – Variance in angular momentum J after time t ($V(t)$; from Equation (3.18)) as a function of time in units of the initial orbital period P, with $\phi_1 = 0.999$, $\theta_1 = -0.988$ and $\sigma_1 = 10^{-4}$. Note that there is first a linear part ("NR"), then a quadratic part ("coherent torque"), and then again a linear part ("RR").

For the typical values of ϕ_1 and θ_1 that we find, these different regimes can be identified in the expression for the variance $V(N)$; Equation (3.18). For very short times, the expression is dominated by the first term, which can thus be associated with NR. The second term and third term are both proportional to N^2 for short times (this can be verified by Taylor expansions assuming $N\phi_1 \ll 1$; the linear terms cancel), and as such represent coherent torques; and they become proportional to N for large time, representing RR. In Figure 3.5 we plot Equation (3.18) for typical values of the parameters of the model.

Equation (3.18) is useful for finding the variance after N periods, but most importantly to define a new process with arbitrary time steps. We can now define a new ARMA(1, 1) process with larger time steps, but with the same statistical properties. If the new process makes steps of N orbits each, we write the new model as

$$\begin{aligned} \Delta_N J_t &= \phi_N \Delta_N J_{t-N} + \theta_N \epsilon_{t-N}^{(N)} + \epsilon_t^{(N)}; \\ \langle [\epsilon^{(N)}]^2 \rangle &= \sigma_N^2, \end{aligned} \tag{3.19}$$

where the parameters $[\phi_N, \theta_N]$ are related to (ϕ_1, θ_1) by[3]

$$\phi_N = \phi(NP) = \phi_1^N; \qquad \theta_N = \theta(NP) = -[-\theta_1]^N. \tag{3.20}$$

---

[3] For ϕ_1 we use the fact that the theoretical ACF of an ARMA(1, 1) model decays on a timescale $P/\ln \phi_1$. We have no interpretation for the functional form of θ_1, which was found after some experimenting. We confirm numerically that this form leads to excellent agreement with simulations with arbitrary time; see Figure 3.6.

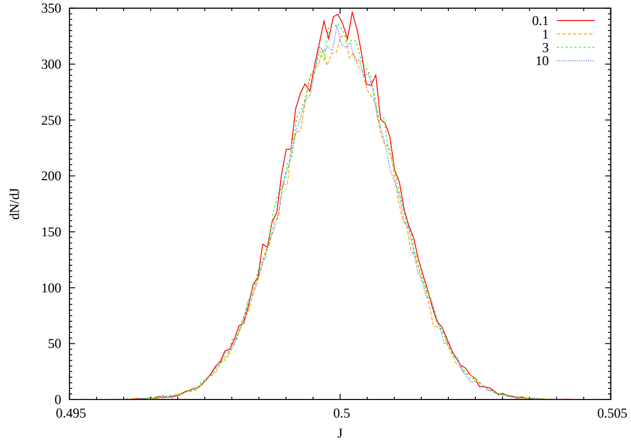

Figure 3.6 – Monte Carlo simulation of RR with the model parameters $\phi_1 = 0.999$, $\theta_1 = -0.988$, and $\sigma_1 = 10^{-6}$ (chosen for purely illustrative purposes), and the time steps in units of the orbital period indicated in the legend. After 10^4 orbits, the distribution is very similar for all time steps chosen, confirming that the diffusion in J is independent of the time step.

Since after N small steps of one period, the variance should be the same as after 1 single step of time N orbits, we can find the new σ to be (see Equations (3.10), (3.18))

$$\sigma_N^2 = \frac{1-\phi_N^2}{1+\theta_N^2+2\phi_N\theta_N}V(N). \tag{3.21}$$

Once the ARMA parameters for steps of one orbital period are found, they can be generalized to a new ARMA model via Equation (3.19), so that the time step equals an arbitrary number of periods (not necessarily an integer number), and the new parameters are found by the use of Equations (3.20) and (3.21). We will exploit these relations in MC simulations (Section 3.6), in which we use adaptive time steps. We have tested the equivalence of the models by considering an ARMA diffusion process over a fixed time interval but with varied time steps. We show an example in Figure 3.6 where we have taken a delta function for the initial J-distribution, and have plotted the resulting final distributions after 10^4 orbits for several different time steps which vary by two orders of magnitude. We find excellent agreement between these distribution functions which verify the generalization of $(\phi_1, \theta_1, \sigma_1)$ to $(\phi_N, \theta_N, \sigma_N)$.

3.4 Interpretation of the ARMA parameters and extension of parameter space

The ARMA(1, 1) model presented here contains the three free parameters $(\phi_1, \theta_1, \sigma_1)$. In this section, we interpret these parameters in the context of a stylized model of a galactic nucleus. Our purpose in doing so is twofold.

First, it relates the ARMA model to the relevant physical processes that play a part in the angular momentum evolution of stars near MBHs, and gives insight into how the parameters depend on the stellar orbits, in particular on their eccentricity. This allows us to define, and discuss, RR in the language of the ARMA model. Second, in Section 3.5 we calibrate the parameters as a function of eccentricity using N-body simulations for one specific configuration — as specified in Section 3.2.1. In order for the parameters to be also valid for other conditions than those studied, one needs to understand how they vary as a function of the quantities that define the system. The model presented in this section, which is based on physical arguments, allows us to generalize our results to models we have not simulated (models with different stellar masses, semi-major axes, etc.) The arguments presented here do not aspire to give a full theoretical model of RR, but rather parameterize the model in a simplified way that is useful for generalization to other systems. We will use this model in our MC simulations (Section 3.6).

3.4.1 Non-resonant relaxation (NR): the parameter σ

For very short times NR dominates the angular momentum evolution of a star and the variance of J is expected to be of order P/t_{NR} after one period, where

$$t_{\mathrm{NR}} = A_{\mathrm{NR}} \left(\frac{M_\bullet}{m}\right)^2 \frac{1}{N_<} \frac{1}{\ln \Lambda} P \tag{3.22}$$

is the NR time (Rauch & Tremaine 1996), defined as the timescale over which a star changes its angular momentum by an order of the circular angular momentum at that radius. In this expression, $N_<$ is the number of stars within the radius equal to the semi-major axis of the star, $\Lambda = M_\bullet/m$, and $A_{\mathrm{NR}} = 0.26$, chosen to match the value of t_E from the N-body simulations; see Figure 3.3. Since this variance should be approximately equal to σ_1^2, it follows that

$$\sigma_1 = f_\sigma \left(\frac{m}{M_\bullet}\right) \sqrt{\frac{N_< \ln \Lambda}{A_{\mathrm{NR}}}}. \tag{3.23}$$

Here f_σ is a (new) free parameter which, calibrated against our N-body simulations, we expect to be of order unity (the deviation from unity will quantify the difference between the energy relaxation time t_E and the non-resonant component of the angular momentum relaxation time t_J). In our N-body simulations we find that σ_1 is an increasing function of e; see Figures 3.12 and 3.14. This suggests that NR is also an increasing function of e which we attribute to the increase in stellar density at small radii which a star on a highly eccentric orbit passes through at periapsis. To account for this in our theory we fit f_σ as a function of e.

3.4.2 Persistence of coherent torques: the parameter ϕ

We now define a new timescale over which interactions between stars remain coherent, the *coherence time* t_ϕ, which corresponds to the time over which secular torques between orbits remain constant. This is the minimum between the precession time of the test star and the median precession time of the field stars. The latter timescale is of importance as there exists at every radius an orbital eccentricity which has equal, but oppositely directed, Newtonian precession due to the potential of the stellar cluster and GR precession. A star with this particular orbital eccentricity remains almost fixed in space; for our chosen model of a galactic nucleus the eccentricity at which this occurs is $e \sim 0.92$ at $0.01\,\mathrm{pc}$. Its coherence time, however, does not tend to infinity, as the surrounding stellar orbits within the cluster continue to spatially randomize.

The timescale for the Newtonian precession (i.e., the time it takes for the orbital periapsis to precess by 2π radians) is given by

$$t_{\mathrm{prec}}^{\mathrm{cl}} = \pi(2-\alpha)\left(\frac{M_\bullet}{N_< m}\right) P(a) f(e,\alpha)^{-1} \tag{3.24}$$

(see Appendix 3.C for derivation), where $N_<$ is the number of stars within the semi-major axis a of the test star, $P(a)$ its period, and

$$\begin{aligned} &f(e,\alpha=7/4)^{-1} \\ &\quad = \left[0.975(1-e)^{-1/2} + 0.362(1-e) + 0.689\right]. \end{aligned} \tag{3.25}$$

The timescale for precession due to general relativity is given by the first order (in $1/c^2$) relativistic correction to the Newtonian result for the angle swept out in one orbit

$$t_{\mathrm{prec}}^{\mathrm{GR}} = \frac{1}{3}(1-e^2)\frac{ac^2}{GM_\bullet}P(a) \tag{3.26}$$

(Einstein 1916). The combined precession time is

$$t_{\mathrm{prec}}(a,e) = \left|\frac{1}{t_{\mathrm{prec}}^{\mathrm{cl}}(a,e)} - \frac{1}{t_{\mathrm{prec}}^{\mathrm{GR}}(a,e)}\right|^{-1}. \tag{3.27}$$

As stated, the coherence time for a particular star is the minimum of its precession time and that of the median precession time of the surrounding stars,

$$t_\phi = f_\phi \min\left[t_{\mathrm{prec}}(a,e), t_{\mathrm{prec}}(a,\tilde{e})\right], \tag{3.28}$$

where $\tilde{e}$ is the median value of the eccentricity of the field stars (so $\tilde{e} = \sqrt{1/2}$ for a thermal distribution) and f_ϕ is a second (new) free parameter.

We now have all the ingredients to define the RR time. This is the timescale over which the angular momentum of a star changes by order of the circular momentum. The angular momentum evolution is coherent over a time of order

t_ϕ, and the change in angular momentum during that time is τt_ϕ, where τ is the torque exerted on the star's orbit. Normalized to the circular angular momentum, this torque is (Rauch & Tremaine 1996)

$$\tau = A_\tau \frac{m}{M_\bullet} \frac{\sqrt{N_<}}{P} e, \tag{3.29}$$

where the linear dependence on eccentricity was determined by Gürkan & Hopman (2007). We adopt their value of $A_\tau = 1.57$ which was determined for a different stellar mass profile $m = 1M_\odot, \alpha = 1.4$ where $M_\bullet = 3\times10^6 M_\odot, r_h = 2\mathrm{pc}$. Assuming that the evolution is random for longer times, this leads to the definition

$$t_{\mathrm{RR}}(E, J) = \left(\frac{1}{\tau t_\phi}\right)^2 t_\phi. \tag{3.30}$$

The theoretical ACF of an ARMA(1, 1) model in Equation (3.11) shows that it decays on a timescale $P/\ln\phi_1$. Hence we find that ϕ scales as $\exp(-P/t_\phi)$. However, even if the coherence time is very long, the evolution of the orbit may not be driven by secular dynamics. The secular torques on an orbit are proportional to its eccentricity so if the eccentricity is very small secular effects are weak. As a result, the evolution is dominated by two-body interactions, which have a vanishingly short coherence time. Within our formalism, this effect can be accounted for by multiplying t_ϕ by a function S,

$$\phi_1 = \exp\left(-\frac{P}{S t_\phi}\right) \tag{3.31}$$

with

$$S \quad = \quad \frac{1}{1 + \exp(k\,[e - e_{\mathrm{crit}}])} \tag{3.32}$$

which interpolates between the secular and two-body regime. We remind the reader that the subscript "1" is used to emphasize that this is the value of ϕ for a time step of one orbital period. The exponential transition between NR and RR regimes is somewhat arbitrarily chosen but fits the data reasonably well. $k > 0$ is a new parameter which determines the steepness of the transition (a third free parameter), and e_{crit} is defined as the critical eccentricity at which the NR and RR times are equal (Equations (3.22), (3.30)):

$$e_{\mathrm{crit}}(a, e) = \sqrt{\frac{\ln\Lambda}{A_{\mathrm{NR}} A_\tau^2}} \left(\frac{P}{t_\phi}\right)^{1/2}. \tag{3.33}$$

Inserting relevant values into the above equation and solving numerically using a Newton-Raphson algorithm, we calculate $e_{\mathrm{crit}} \sim 0.3$ at $a = 0.01$ pc which is in good agreement with the N-body simulations. We plot e_{crit} as a

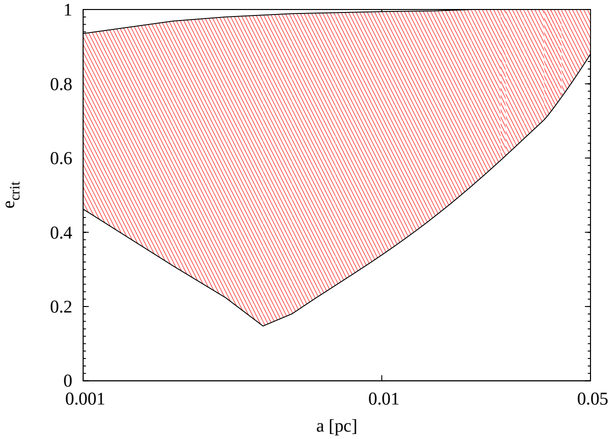

Figure 3.7 – Critical eccentricity $e_{\rm crit}$ for which NR and RR mechanisms work on comparable timescales, as a function of semi-major axis a from the MBH in our Galactic nucleus model. The shaded region in this plot indicates the eccentricities for which RR is the dominant mechanism. The lower values of $e_{\rm crit}$ decrease with distance to the MBH as RR becomes more effective (τ and t_ϕ increase with decreasing a). At $a \sim 0.004$ pc this value rises again in our model as $t_{\rm NR}$ decreases rapidly as $r^{-1/4}$. The higher values of $e_{\rm crit}$ are due to GR effects which decrease t_ϕ toward the MBH and substantially reduce the effectiveness of RR. The lower values of $e_{\rm crit}$ are due to the fact that $\tau \propto e$.

function of a in Figure 3.7. RR becomes more effective at lower a as the mass precession time increases, and the value of $e_{\rm crit}$ decreases. At the lowest a there are two roots to Equation (3.33); this is due to GR effects which compete with mass precession and decrease the coherence time to such an extent as to nullify the effects of RR at high eccentricities. These results are derived for a simplified galactic nucleus model and will change for different assumptions on the mass distribution; nevertheless we find the concept of $e_{\rm crit}$ useful for understanding the relative importance of RR and NR at different radii.

3.4.3 Magnitude of resonant relaxation steps: the parameter θ

For times less than t_ϕ, there are coherent torques between stellar orbits; see Equation (4.6). The expected variance after a time t_ϕ is then

$$\langle \Delta J_\phi^2 \rangle = A_\tau^2 \left(\frac{m}{M_\bullet}\right)^2 N_< \left(\frac{t_\phi}{P}\right)^2 e^2. \qquad (3.34)$$

Alternatively, we can use the ACF (see Appendix 3.D for derivation) to find

$$\langle \Delta J_\phi^2 \rangle = \sigma_1^2 \left(\frac{t_\phi}{P}\right)^2 \frac{(\theta_1 + \phi_1)(\theta_1 + 1/\phi_1)}{1 - \phi_1^2}. \qquad (3.35)$$

Equating Equations (3.34) and (3.35) gives two values for θ_1

$$\theta_1 = \frac{1}{2}\left[-\left(\frac{1}{\phi_1}+\phi_1\right) \pm \sqrt{\frac{1}{\phi_1^2}+\phi_1^2-2+\frac{4(1-\phi_1^2)\tau^2P^2}{\sigma_1^2}}\right] \tag{3.36}$$

Taking the positive root we find an excellent match to the data. For values of $e > e_{\rm crit}$ the first term $\frac{1}{2}(\frac{1}{\phi_1}+\phi_1) \approx 1$ and recognizing the Taylor expansion of $-\exp(-x) \approx x - 1$ we simplify this expression to

$$\theta_1 = -\exp\left(-\frac{f_\theta}{2}\sqrt{\frac{1}{\phi_1^2}+\phi_1^2-2+\frac{4(1-\phi_1^2)\tau^2P^2}{\sigma_1^2}}\right) \tag{3.37}$$

where f_θ is a fourth free parameter.

We summarize this section by clarifying that we have four free parameters in our ARMA model (f_θ, f_ϕ, f_σ, k) fully determinable by our N-body simulations, with which we calibrate our model for use in MC simulations.

3.5 Results: ARMA analysis of the N-body simulations

We now return to the N-body simulations, and use the time series of angular momenta that are generated to calibrate the ARMA model. These parameters fully define both the RR and NR processes. Once they are known, they can be used to generate new angular momentum series that have the correct statistical properties, much like what is done in regular MC simulations. We will exploit this method in Section 3.6.

When a test star has mass, there will be a back-reaction on the field stars known as resonant friction, analogous to dynamical friction (Rauch & Tremaine 1996). In our simulations, we consider both the case that the test star is massless and that it has the same mass as the field stars to calibrate the model parameters. Differences in the parameters then result from resonant friction.

We use the “R” language for statistical computing to calculate the ARMA model parameters from our simulations. We input the individual angular momentum time series of a test star, and use a maximum likelihood method to calculate ϕ_1, θ_1 and σ_1. We find that the drift term $\langle \Delta J \rangle$ for stars of all eccentricities is $\mathcal{O}(10^{-6})$.

In Figure 3.8 and 3.9 we show scatter plots of the model parameters $1-\phi_1$ and $1+\theta_1$, for simulations in which the test stars are massless and massive respectively. We present these quantities rather than ϕ_1 and θ_1 themselves because they span several orders of magnitude and, physically speaking, the relevant question is by how much the parameters differ from (minus) unity. For intermediate eccentricities ($0.4 \lesssim e \lesssim 0.9$), $1-\phi_1$ is much smaller than unity, indicating that the angular momentum autocorrelations are indeed persistent, and there are significant torques between stellar orbits. However, the

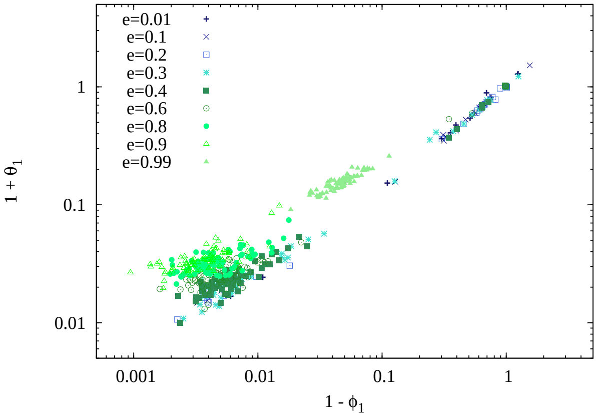

Figure 3.8 – Scatter plot of $(1-\phi_1)$ vs $(1+\theta_1)$ as found from data-analysis on the N-body runs, for the case of massless test stars. For most cases, the parameters cluster, leading to a concentration of points around small values; reasons for exceptions are discussed in the text. From inspection of several individual cases, we see that the test stars of intermediate eccentricities which have values $\phi_1, |\theta_1| \lesssim 1$ (to the bottom left of plot) have non-zero autocorrelations for long times, similar to Figure 3.4. This is as expected from Equation (3.11). Test stars with $\phi_1, \theta_1 \approx 0$ have ACFs that are close to zero everywhere, even for short times.

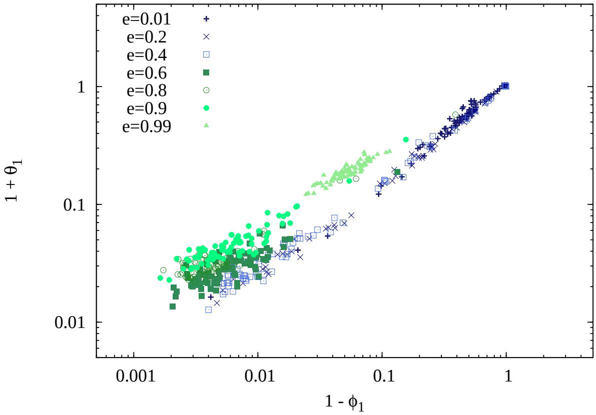

Figure 3.9 – Scatter plot of $(1-\phi_1)$ vs $(1+\theta_1)$ as found from data analysis on the N-body runs, for the case of massive ($m = 10M_\odot$) test stars. We find that, for most eccentricities, the values for $1-\phi_1$ and $1+\theta_1$ cluster around those for the massless cases.

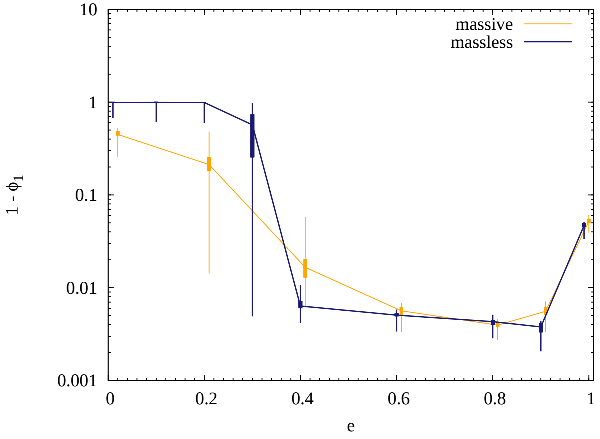

Figure 3.10 – Median value of $1-\phi_1$, plotted on a log scale, for both massless and massive runs, computed for 80 test stars in each eccentricity bin. Closed boxes denote the 45th and 55th percentiles, while the lines indicate the one sigma values. Note that for very high eccentricities the values increase, which in the interpretation of Section 3.4 means that the coherence time has decreased. This is consistent with the fact that for $e \geq 0.92$, GR precession becomes dominant over mass precession. The deviation at low eccentricities between values for massless and massive particles may due to resonant friction.

coherent torques are mixed with NR noise (the classical NR as treated in Binney & Tremaine (2008)), and as a result $1+\theta_1 \ll 1$ as well. These values for $1-\phi_1$ and $1+\theta_1$ confirm that although the ACF for RR is finite for long times, it is much smaller than unity — which would be the case if there was no NR noise at all.

For very small and very large eccentricities, we find $\phi_1 \approx \theta_1 \approx 0$, so there are no persistent torques of significance. The reason for the absence of coherent torques on the high and low eccentricity limits are different: for very small eccentricities, the secular torque on a stellar orbit approaches zero as $\tau \propto e$ (Gürkan & Hopman 2007). At the high eccentricity end, there are significant torques, but the coherence time is so short due to general relativity, that the persistence of these torques is negligible, and there is no coherent effect (quenching of RR: see Merritt & Vasiliev 2010). Test stars with eccentricities of $0.2 \leq e \leq 0.4$ have a large scatter in their $1-\phi_1$ and $1+\theta_1$ values. This is due to their proximity to e_{crit}, the eccentricity at which NR and RR compete for dominance at this radius in our model.

In Figures 3.10 and 3.11 we compare the median values of $1-\phi_1$ and $1+\theta_1$ for both massive and massless test stars. There is significant scatter in the data near $0.2 \leq e \leq 0.4$, where NR relaxation competes with RR, as can be seen from the 45th, 55th and one sigma $(34.1-84.1)$ percentiles. The differences between the median values for massless and massive test stars are very small, such that we did not see a strong feedback effect due to resonant friction,

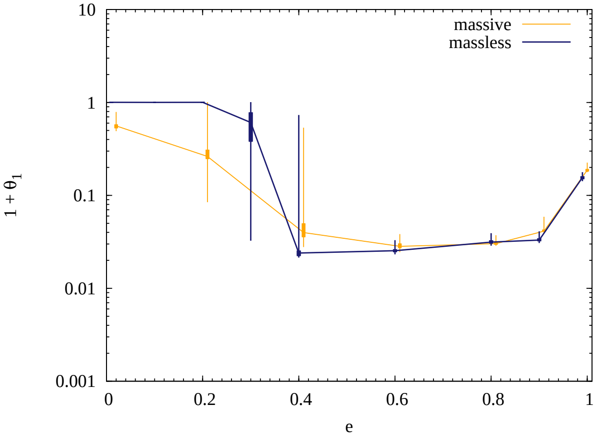

Figure 3.11 – Median value of $1 + \theta_1$, plotted on a log scale, for massless and massive runs, computed for 80 test stars in each eccentricity bin. Closed boxes denote the 45th and 55th percentiles, while the lines indicate the one sigma values. The results for massless and massive particles follow each other closely except at the low-eccentricity end where there is a large scatter in the data.

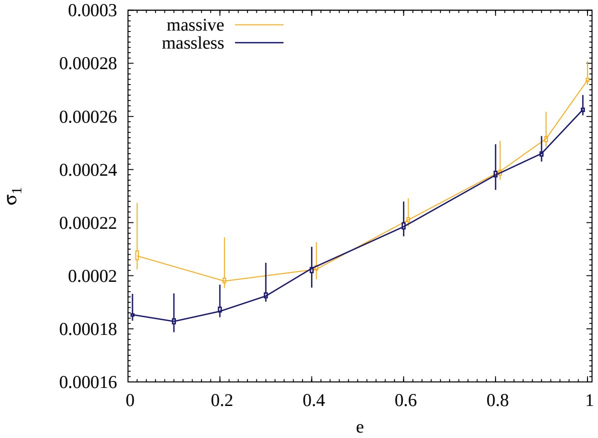

Figure 3.12 – Data for the model parameter σ_1 as a function of eccentricity for massless and massive test stars. Plotted are the 45th to 55th percentiles (open boxes), one sigma values (lines), and 50th percentile for each eccentricity. The results for massive test stars are shifted along the x-axis for clarity. The values follow each other closely with the exception of low eccentricities.

except for small stellar eccentricities. Resonant friction appears to drag stars away from circular angular momentum. The same deviation is seen for the σ_1 model parameter in Figure 3.12.

From here on, we use only the results of the massless simulations as we have a larger range of test star eccentricities and have found the ARMA parameters

Table 3.2 – Median values of $1-\phi_1$, $1+\theta_1$ and σ_1 for massless test stars as a function of eccentricity.

e	$1-\phi_1$	$1+\theta_1$	σ_1 (10^{-4})
0.01	0.992	1.004	1.853
0.1	0.993	1.002	1.828
0.2	0.991	1.003	1.866
0.3	0.569	0.609	1.923
0.4	0.006	0.024	2.027
0.6	0.005	0.025	2.184
0.8	0.004	0.031	2.379
0.9	0.004	0.033	2.460
0.99	0.047	0.156	2.626

$(\phi_1, \theta_1, \sigma_1)$ to be similar in value. We refer the reader to Table 3.2 for exact quantities.

The ARMA model parameters for both very low eccentricities ($e \sim 0.01$) and high eccentricities ($e \gtrsim 0.4$) tend to cluster together. For these cases one form of relaxation, either NR or RR, dominates the form of the ACFs, and taking mean values of (ϕ_1, θ_1) gives an accurate representation of the population. However, near the e_{crit} boundary where the two relaxation effects compete for dominance, (ϕ_1, θ_1) do not consistently cluster but rather choose NR or RR values which can vary significantly. Hence we choose the median value in each case to compare with our theory.

In Figures 3.13 and 3.14 we compare the experimental median values of $(1-\phi_1)$, $(1+\theta_1)$ and σ_1 to our theoretical model. We find that good agreement between the N-body simulations and the model is obtained by assuming values for the free parameters $(f_\phi, f_\theta, k) = (0.105, 1.2, 30)$. The value of f_ϕ shows that the coherence time t_ϕ is much less than the precession time t_{prec}; see Equation (3.28). Fitting f_σ as a function of e we find

$$f_\sigma = 0.52 + 0.62e - 0.36e^2 + 0.21e^3 - 0.29\sqrt{e}. \qquad (3.38)$$

3.6 Monte Carlo simulations and applications

Our aims in this section are to (1) explore the long-term evolution of stars around an MBH, (2) investigate the depletion of stars around an MBH due to RR in context of the “hole” in late-type stars in the GC, and (3) study the evolution of the orbits of possible S-star progenitors from different initial setups. Direct N-body simulations of secular dynamics are challenging due to the inherent large range in timescales. The precession time is orders of magnitude larger than the orbital time, and in order to study relaxation to a steady-state, the system needs to evolve for a large number of precession times. Currently it is not feasible to do this using N-body techniques. Instead we draw on MC

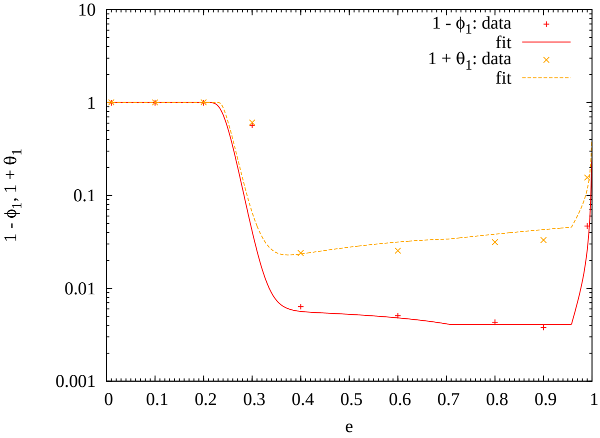

Figure 3.13 – Median value of $(1 - \phi_1)$ and $(1 + \theta_1)$, compared with the theoretical values from (3.31, 3.37). There is a sharp transition between eccentricities $0.3 \lesssim e \lesssim 0.4$ where the two effects of NR and RR compete. A second transition occurs at high eccentricities ($e > 0.92$) as the coherence time, and hence ϕ_1, decreases due to general relativistic effects. The theory does not exactly match the median value of the data at $0.2 < e < 0.3$. However we can vary the value of $e_{\rm crit}$ to reconcile this difference and we find that this is not important for our results in the next section.

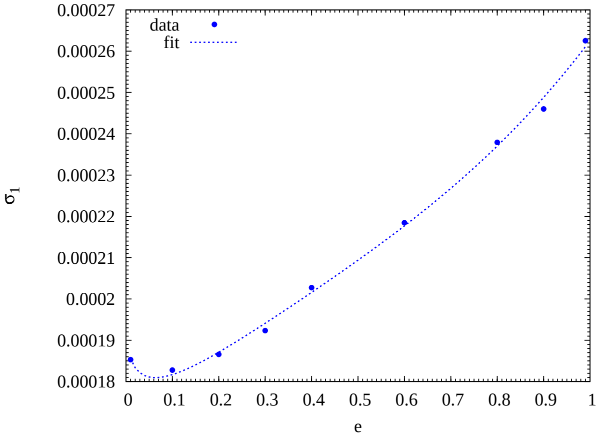

Figure 3.14 – Median values of the model parameter σ_1 (related to non-resonant relaxation) and theoretical fit, as a function of eccentricity for massless test stars.

simulations to study long term secular evolution. For this purpose, we have developed a two-dimensional (energy and angular momentum) MC code. The main new aspect compared to earlier work is that it implicitly includes evolution due to RR. The angular momentum diffusion is based on the ARMA(1, 1) model presented in Section 3.3. For the energy evolution we use a similar method as in Hopman (2009), which was in turn based on Shapiro & Marchant (1978). A key feature of this method is a cloning scheme, which allows one to resolve the distribution function over many orders of magnitude in energy, even though the number of particles per unit energy is typically a steep power-law, $dN/dE \propto E^{-9/4}$. We will not describe the cloning scheme here; for details we refer the reader to Shapiro & Marchant (1978) and Hopman (2009).

We base our model of a galactic nucleus on parameters relevant for the GC; see Section 3.2. We set the MBH mass as $M_\bullet = 4 \times 10^6 M_\odot$, which affects the physics through the GR precession rate and the loss cone. We linearize the system by considering the evolution of test stars on a fixed background stellar potential. We assume a single-mass distribution of stars of either $m = 1M_\odot$ or $m = 10M_\odot$, with the number of stars within a radius r, $N(< r)$, following a power-law profile as in Equation (3.2).

In Figure 3.15 we plot the NR and RR timescales for stars with different orbital eccentricities as a function of semi-major axis for this model with $m = 10M_\odot$. A cuspy minimum arises in the RR timescales where GR precession cancels with Newtonian mass precession. In their GC model Kocsis & Tremaine (2010) find, using Eilon et al. (2009) parameters, the cuspy minimum of RR near $r = 0.007\,\mathrm{pc}$ (see their Figure 1), which falls precisely within the range of values in our model ($0.004 - 0.02\,\mathrm{pc}$). Figure 3.16 shows the RR time as a function of eccentricity e for different stellar masses within $0.01\,\mathrm{pc}$. Models with different enclosed masses will be used in Section 3.7.3.

In reality, several stellar populations are present in the GC, and our choice for a single mass model is therefore a simplification. The slope $\alpha = 1.75$ is smaller than would be expected for strong mass-segregation (Alexander & Hopman 2009; Keshet et al. 2009), but was chosen to make the model self-consistent as a collection of interacting single mass particles will relax to have this distribution (Bahcall & Wolf 1976).

3.6.1 Angular momentum

For the angular momentum evolution of a test star, we go through the following steps: we first calculate the ARMA model parameters for one orbital period $(\phi_1, \theta_1, \sigma_1)$ through Equations ((3.31), (3.37), (3.23)). We then find the model parameters $(\phi_N, \theta_N, \sigma_N)$ for the time step δt, where $N(= \delta t/P) \in \mathbb{R} > 0$, using Equations (3.20) and (3.21). Finally, the step in angular momentum is given by Equation (3.19)

$$\begin{aligned} \Delta_N J_t &= \phi_N \Delta_N J_{t-N} + \theta_N \epsilon_{t-N}^{(N)} + \epsilon_t^{(N)}; \\ \langle [\epsilon^{(N)}]^2 \rangle &= \sigma_N^2. \end{aligned} \tag{3.39}$$

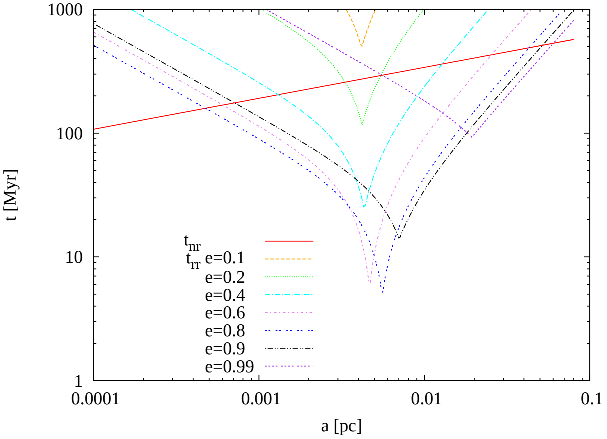

Figure 3.15 – RR and NR timescales in units of Myr as a function of semi-major axis a in our Galactic nucleus model for different eccentricities.

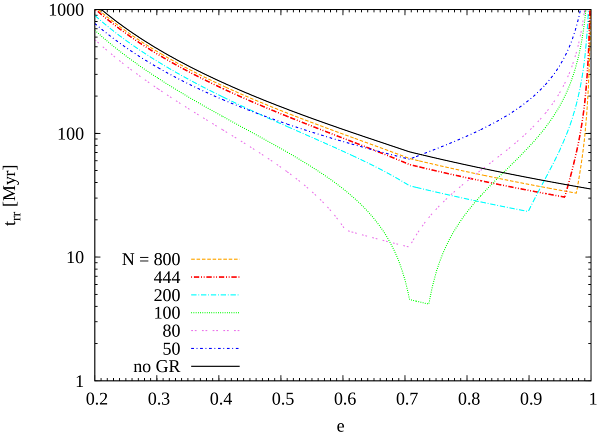

Figure 3.16 – Resonant relaxation timescale $t_{\rm rr}$ for varying stellar mass (Nm where $m = 10M_{\odot}$) within 0.01 pc as a function of e. In this plot the density power-law index $\alpha = 1.75$. The e at which RR is most efficient decreases with decreasing mass. The solid black line indicates the value of $t_{\rm rr}$ if the effects of GR precession are not taken into account (and is independent of number N). In our fiducial model the optimal efficiency (shortest $t_{\rm rr}$) is for $Nm = 1000M_{\odot}$. At this radius, GR effects are important for RR and $t_{\rm rr}$ is not independent of N.

3.6.2 Energy

The energy of a star is given in units of the square of the velocity dispersion at the radius of influence, v_h^2, such that $E = r_h/2a$. The step in energy during a time δt is

$$\Delta E = \xi E \left(\frac{\delta t}{t_{\rm NR}}\right)^{1/2}, \tag{3.40}$$

where ξ is a normal random variable with zero mean and unit variance, and $t_{\rm NR}$ is given by Equation (3.22) with $A_{\rm NR} = 0.26$.

3.6.3 Initial conditions and boundary conditions

For our steady-state simulations, we initialize stars with energies $E = 1$ and angular momenta drawn from a thermal distribution, $dN(J)/dJ \propto J$. We follow the dynamics of stars between energy boundaries $0.5 = E_{\rm min} < E < E_{\rm max} = 10^4$ (for our model this corresponds to $2.31\,{\rm pc} > a > 1.155\times10^{-4}\,{\rm pc}$). Stars that diffuse to $E < E_{\rm min}$ are reinitialized, but their time is not set to zero (zero-flow solution; Bahcall & Wolf 1976, 1977). Stars with $E > E_{\rm max}$ are disrupted by the MBH and also reinitialized while keeping their time. Stars have angular momenta in the range $J_{\rm lc} < J < 1$, where $J_{\rm lc}$ is the angular momentum of the loss cone. Stars with $J < J_{\rm lc}$ are disrupted and reinitialized, while stars with $J > 1$ are reflected such that $J \to 2 - J$.

3.6.4 Time steps

In the coherent regime, the change in angular momentum during a time δt is of order $\delta J \sim \tau\delta t \sim A_\tau e(m/M_\bullet)\sqrt{N_<}(\delta t/P)$. The changes in angular momentum should be small compared to either the size of the loss cone $J_{\rm lc}$, or the separation between J and the loss cone, $J - J_{\rm lc}$; and compared to the distance between the circular angular momentum J_c and J, i.e., compared to $1 - J$. We therefore define the time step to be

$$\delta t = f_t\, \tau(a,e)^{-1} \min\left[J_c - J, \max\left(|J - J_{\rm lc}|, J_{\rm lc}\right)\right], \tag{3.41}$$

where $f_t \ll 1$. After some experimenting we found that the simulations converge for $f_t \leq 10^{-3}$, which is the value we then used in our simulations.

3.6.5 Treatment of the loss cone

Stars with mass m and radius $R_\star$ on orbits which pass through the tidal radius

$$r_t = \left(\frac{2M_\bullet}{m}\right)^{1/3} R_\star \tag{3.42}$$

are disrupted by the MBH. The loss cone is the region in angular momentum space which delineates these orbits and is given by

$$J_{\rm lc} = \sqrt{2GM_\bullet r_t}. \tag{3.43}$$

Our prescription for the time step, which is similar to that used in Shapiro & Marchant (1978), ensures that stars always diffuse into the loss cone and cannot jump over it. Stars are disrupted by the MBH when their orbital angular momentum is smaller than the loss cone, *and* they pass through periapsis. Only if $\mathrm{floor}(t/P) - \mathrm{floor}\left[(t-\delta t)/P\right] > 0$, do we consider the star to have crossed periapsis during the last time step and hence to be tidally disrupted (or directly consumed by the MBH in case of a compact remnant). In that case we record the energy at which the star was disrupted and initialize a new star, which starts at the time t at which the star was disrupted.

3.7 Results

3.7.1 Evolution to steady-state

We first consider a theoretical benchmark problem, that of the steady-state distribution function of a single-mass population of stars around an MBH. With $m = 1M_\odot$ this solution appears after $\sim 100\,\mathrm{Gyr}$ $(10$ energy diffusion timescales; see Appendix 3.B). In order to highlight the differences caused by RR relative to NR, we define the function

$$g(E, J^2) \equiv \frac{E^{5/4}}{J^2}\frac{d^2N(E,J^2)}{d\ln E d\ln J^2}. \tag{3.44}$$

For a Bahcall & Wolf (1976) distribution without RR, this function is constant. In Toonen et al. (2009), simulations similar to those presented here were used, except that angular momentum relaxation was assumed to be NR. It was shown that indeed $g(E, J^2)$ is approximately constant for all (E, J) for the NR case; see Figure A1 in that paper.

In Figure 3.17 we show a density plot of the function $g(E, J^2)$ from our steady-state simulations, which illustrates several interesting effects of RR. At low energies, $g(E, J^2)$ is constant which is to be expected since the precession time is of similar magnitude as the orbital period, such that there are no coherent torques. At higher energies ($E \gtrsim 10$), there are far fewer stars than for a classical Bahcall & Wolf (1976) cusp. This is a consequence of enhanced angular momentum relaxation, where stars are driven to the loss cone at a higher rate than can be replenished by energy diffusion, and was anticipated by one-dimensional Fokker-Planck calculations (Hopman & Alexander 2006, see their Figure 2). At the highest energies considered ($E > 100$) most orbits accumulate close to the loss cone, and there are a few orbits populated at larger angular momenta, with a “desert” in between.

To further illustrate the reaction of the stellar orbits to RR, in Figure 3.18 we show the distribution of eccentricities of stars in slices of energy space. As in Figure 3.17 we see that for higher energies the distribution is double peaked, with most stars accumulating at the highest eccentricities, and another peak at eccentricities around $e = 0.2$. This distribution can be understood as follows:

RR is very effective at intermediate eccentricities, where torques are strong and the coherence time is very long. As a result, the evolution of such eccentricities occurs on a short timescale. At high eccentricities, the coherence time is short due to GR precession, while at low eccentricities the torques are very weak. At such eccentricities, evolution is very slow. The eccentricity therefore tends to “stick” at those values, leading to the two peaks in the distribution. It is interesting to note that N-body simulations by Rauch & Ingalls (1998) also show a rise of the angular momentum distribution near the loss cone. This result however may be affected by the new dynamical mechanism recently described by Merritt et al. (2011).

In Figure 3.19 we show the rate of direct captures of stars by the MBH per log energy. Loss cone theory (Frank & Rees 1976; Lightman & Shapiro 1977; Cohn & Kulsrud 1978; Syer & Ulmer 1999; Magorrian & Tremaine 1999) yields that the disruption rate continues to rise with decreasing energy for energies larger than the “critical energy[4]”, which in our case is at $E < 1$. This is in accordance with Figure 3.19. As the figure shows, the rate drops quickly; this is due to the depletion of stars, and was also found (though to a lesser extent, compare their Figure 4) in Hopman & Alexander (2006).

A limiting factor of our approach in this section is that the potential of our Galactic nucleus does not evolve; hence we cannot look at collective effects (e.g., instabilities). Ideally an iterative process should be used to self-consistently find the steady-state solution; we have shown that RR significantly depletes stars at inner radii. To what extent this will affect our steady-state solution is beyond the scope of the chapter. We note the RR time does not formally depend on the stellar number density until such energies and angular momenta that GR precession becomes important.

3.7.2 A depression in the Galactic center

Early studies of integrated starlight at the GC detected a dip in the CO absorption strength within $15''$ of the MBH, Sgr A* (Sellgren et al. 1990; Haller et al. 1996), which indicated a decrease in the density of old stars (see also Genzel et al. 1996, 2003; Figer et al. 2000, 2003; Schödel et al. 2007; Zhu et al. 2008). Recent observations by Do et al. (2009), Buchholz et al. (2009), and Bartko et al. (2010) have confirmed this suggestion and, in particular, revealed that the distribution of the late-type stars in the central region of the Galaxy is very different than expected for a relaxed density cusp around an MBH.

Do et al. (2009) use the number density profile of late-type giants to examine the structure of the nuclear star cluster in the innermost $0.16\ \mathrm{pc}$ of the GC. They find the surface stellar number density profile, $\Sigma(R) \propto R^{-\Gamma}$, is flat with $\Gamma = 0.26 \pm 0.24$ and rule out all values of $\alpha > 1.0$ at a confidence level of 99.7%. The slope measurement cannot constrain whether there is a hole in the

---

[4] The critical energy is approximately the energy where the change in angular momentum per orbit equals the size of the loss cone.

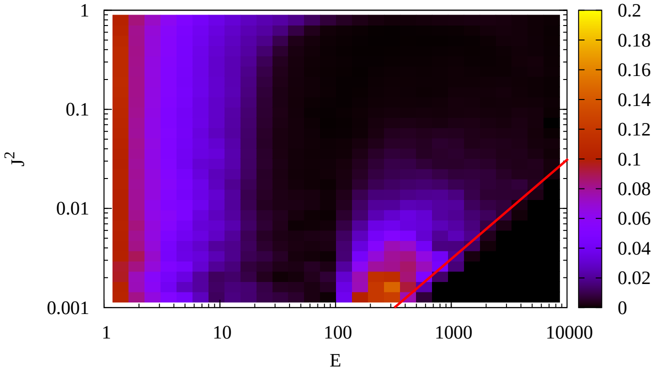

Figure 3.17 – Two-dimensional distribution of stars, normalized such that for an isothermal Bahcall & Wolf (1976) profile the distribution should be constant (see Equation (3.44)). Note that angular momentum is in units of the circular angular momentum, so that the loss cone (indicated by the red line) is not constant. At high energies it is clear that there is a depletion of stars, and that the distribution of angular momenta is far from isotropic.

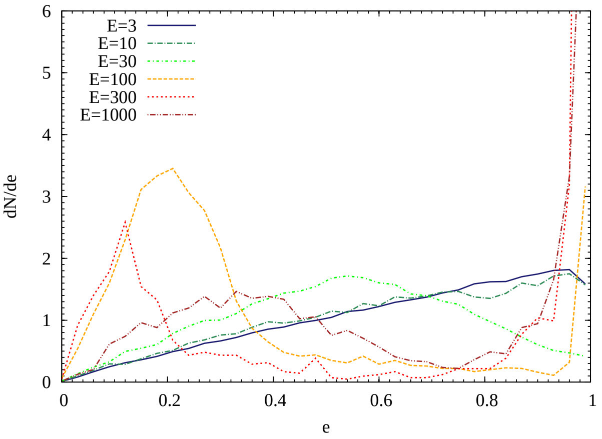

Figure 3.18 – Eccentricity distribution at fixed energies. For high energies the distribution of eccentricities is bimodal due to RR, whereas for low energies the distribution is isotropic with a cutoff at the loss cone.

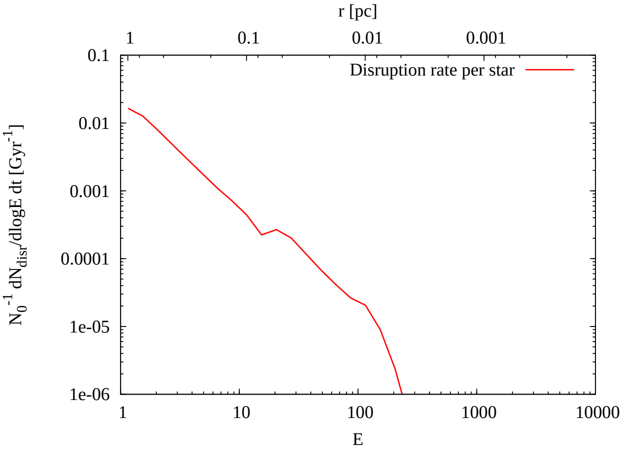

Figure 3.19 – Disruption rate per star per $\log E$, in units of Gyr^{-1}, as a function of energy. The rate drops quickly as the stellar distribution is depleted due to RR.

stellar distribution or simply a very shallow power law volume density profile. Buchholz et al. (2009) show that the late-type density function is flat out to $10''$ with $\Gamma = -0.7 \pm 0.09$ and inverts in the inner $6''$, with power-law slope $\Gamma = 0.17 \pm 0.09$. They conclude that the stellar population in the innermost $\sim 0.2\,\mathrm{pc}$ is depleted of both bright and faint giants. These results are confirmed by Bartko et al. (2010) who find that late-type stars with $m_k \leq 15.5$ have a flat distribution inside of $10''$.

This result has changed our perception of the nuclear star cluster at the center of our Galaxy. Stellar cusp formation theory predicts a volume density profile $n(r) \propto r^{-\alpha}$ of relaxed stars with $\alpha = 7/4$ for a single mass population (Bahcall & Wolf 1976) and has been confirmed in many theoretical papers with different methods, including Fokker-Planck (e.g., Cohn & Kulsrud 1978; Murphy et al. 1991), MC (e.g., Shapiro & Marchant 1978; Freitag & Benz 2002), and N-body methods (Preto et al. 2004; Baumgardt et al. 2004; Preto & Amaro-Seoane 2010). Theory also predicts that a multi-mass stellar cluster will mass segregate to a differential distribution with the more massive populations being more centrally concentrated. The indices of the power-law density profiles for the different mass populations can vary between $3/2 < \alpha < 11/4$ (Bahcall & Wolf 1977; Freitag et al. 2006; Alexander & Hopman 2009).

There have been two types of solutions put forward in the literature to explain the discrepancy between cusp formation theory and observations of the old stellar population in the GC. The first maintains that the stellar cusp in the GC is relaxed as predicted, but additional physical mechanisms have depleted the old stars in the central region. Such mechanisms include strong mass segregation (Alexander & Hopman 2009) and envelope destruction of giants by stellar collisions (see Dale et al. 2009, and references within). The second solution proposes an unrelaxed cusp, either by the depletion of the stars due to the infall of an intermediate-mass black hole (IMBH; Levin 2006; Baumgardt et al. 2006), or from a binary black hole merger (Merritt & Szell 2006; Merritt 2010). Kinematical information for the old stellar population in the GC however shows a lack of evidence for any large-scale disturbance of the old stellar cluster (Trippe et al. 2008), and Shen et al. (2010) find that the Galaxy shows no observational sign that it suffered a major merger in the past $9-10\,\mathrm{Gyr}$. In addition to this, the dynamics of the S-stars and of the MBH greatly restricts the parameter space available for the presence of an IMBH in the GC (Gualandris & Merritt 2009). For a summary see the latest review by Genzel et al. (2010).

Here we propose that these observations can be explained in part by a depression of stars carved out by RR acting together with tidal disruption. The underlying reason is that stars move rapidly in angular momentum space and enter the loss cone at a higher rate than are replaced by energy diffusion. We show that when we initialize the system as a cusp that, even though steady-state is reached in longer than a Hubble time, the depression forms on a shorter timescale.

We perform simulations of stars, both for $m = 1M_\odot$ and $m = 10M_\odot$, initially distributed in a Bahcall-Wolf (BW) cusp around the MBH, such that $dN/dE \propto E^{-9/4}$. We present first the results for $m = 10M_\odot$, chosen to reflect the dominant stellar population at small radii. We plot the stellar distribution function $f(E)$, which scales as $E^{1/4}$ for BW cusp, at various times during the simulation as the stars move in angular momentum space due to RR; see Figure 3.20. In $\sim 1\,\mathrm{Gyr}$ a depression is carved out of the population of stars, significantly depleting the stellar population around the MBH out to $\sim 0.2\,\mathrm{pc}$. To conclusively demonstrate that RR is the reason for this depression, we also show the distribution of stars for simulations in which we have switched RR off (by setting $\phi_1 = \theta_1 = 0$, $\sigma_1 \neq 0$) such that angular momentum relaxation follows a random walk. In this case no depression forms[5]. These simulations show that, as the cusp is destroyed on timescales of a few Gyr due to RR, a BW cusp is not a solution to the distribution of stars around an MBH. We see the same appearance of a depression when we substitute our non-resonant parameters (both energy and angular momentum) for those of Eilon et al. (2009).

In Figure 3.21, we plot the number density of stars as a function of radius from the MBH. We do this by sampling each stellar orbit randomly in mean anomaly. Black lines indicate the initial BW number density slope of -1.75 and a slope of -1. The slope begins to deviate, albeit gently, from the BW solution at $\sim 0.5\,\mathrm{pc}$ and decreases to -1 at $\sim 0.1\,\mathrm{pc}$. We present results from $m = 1M_\odot$ simulations in Figures 3.22 and 3.23 even though, due to mass segregation, we do not expect low-mass stars to dominate the potential so close to an MBH.

---

[5] The fact that the distribution moves away from the BW solution is attributed to a factor of $\sim$two discrepancy in our energy relaxation time due to the outer cut-off in radius in our N-body simulations; see Appendix 3.B

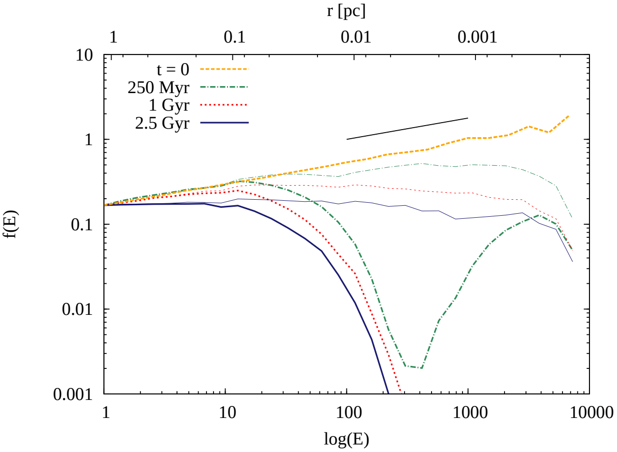

Figure 3.20 – Carving out of a depression in the distribution of stars around an MBH for simulations in which $m = 10M_{\odot}$. The broken orange line shows the stellar distribution at the start of the simulation (the solid black line above indicates a slope of $1/4$). The thick colored lines show the results for RR while the corresponding (in color and style) thin lines show results for simulation in which RR is switched off. The energy, or equivalently radius, at which RR becomes efficient at carving out the depression is clearly seen on the scale of ~ 0.1 pc.

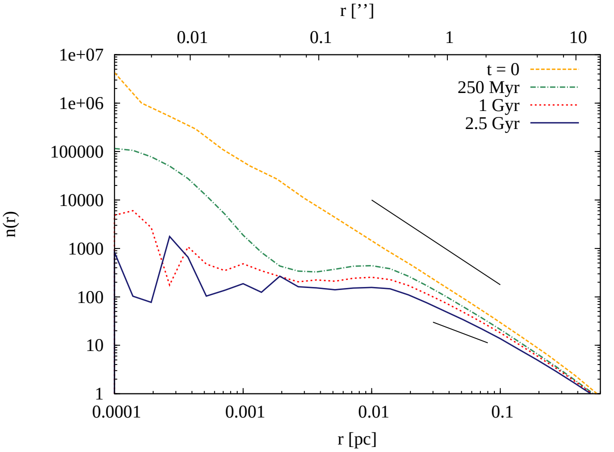

Figure 3.21 – Number density of stars as a function of radius (in parsec and arcsecond) from the MBH for $m = 10M_{\odot}$ simulations. The stellar distribution begins to deviate from the BW solution at ~ 0.5 pc. The black lines indicate a slope of -1.75 (top) and -1.0 (bottom right).

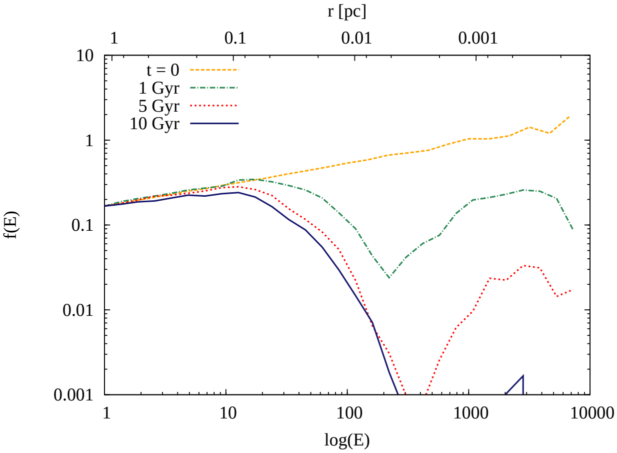

Figure 3.22 – Carving out of a depression in the distribution of stars around an MBH for simulations in which $m = 1M_{\odot}$. The timescale on which the depression develops is longer than for simulations in which the potential is built up of $10M_{\odot}$ stars. Stars which have an energy $E \gtrsim 1000$ survive longer than those with $100 \gtrsim E \gtrsim 1000$ as RR is ineffective so close to the MBH due to GR.

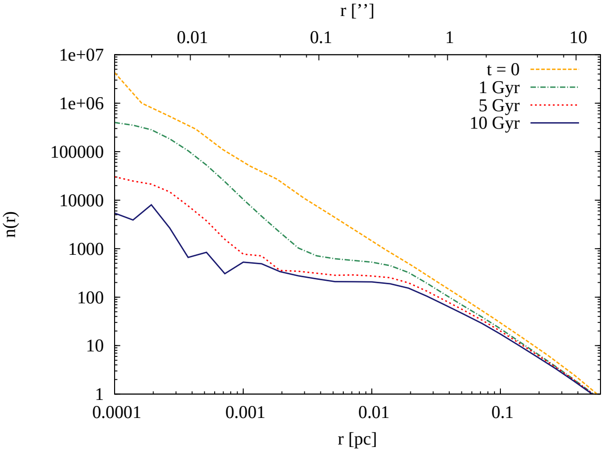

Figure 3.23 – Number density of stars as a function of radius (in parsec and arcsecond) from the MBH for $m = 1M_{\odot}$ simulations. The depression in stars takes an order of magnitude longer in time to develop than the $m = 10M_{\odot}$ simulations.

The major difference between the two simulations is the timescale on which the depression forms, $1\,\mathrm{Gyr}$ and $10\,\mathrm{Gyr}$, respectively.

To reproduce the radial extent of the depletion of old stars in the observations of Do et al. (2009), Buchholz et al. (2009), and Bartko et al. (2010), the size of the hole in energy space must be significantly larger, by a factor of

$5-10$, than what we find in our simulations[6]. In addition, a hole in energy space alone cannot give rise to an inverted profile in surface number density. We stress however that the potential in our model does not evolve in response to RR. As the depression develops and the number of stars at small radii decreases, the energy relaxation timescale, $t_{\rm NR} \propto N^{-1}$, will increase. As N is not important for the RR timescale for all energies but the largest (GR precession at small radii affects the precession rate), this could further enlarge the depression as the rate of stars flowing inward toward the MBH decreases.

In Figure 3.24, we demonstrate the increase in the NR timescale in response to the hole in stars. We use a fit to the stellar density profile at $1\,\rm Gyr$ from Figure 3.21 to recalculate $t_{\rm NR}$, normalizing the profile such that the mass in stars at the radius of influence is equal to that of the MBH. We plot the RR timescale without GR precession as relativistic effects are unimportant at radii greater than $\sim 10^{-2}$; see Figure 3.15. As the outer extent of the hole at $\sim 10^{-1}\,\rm pc$ is at a much larger distance from the MBH, the RR timescale at this scale will not be affected by changes in N. The increase in the radius at which $t_{\rm NR} = t_{\rm RR}$ strongly suggests that the outer radius of the hole should increase in response to the change in stellar potential.

One implication of this depression is that we expect no gravitational wave bursts to be observed from the GC (Hopman et al. 2007). For the implications of the existence of a depletion of stars in the vicinity of an MBH on predicted event rates of gravitational wave inspirals of compact objects (EMRIs) and bursts, see Merritt (2010).

3.7.3 Dynamical evolution of the S-stars

At a distance of $\sim 0.01\,\rm pc$ from the MBH in the GC, there is a cluster of young stars known as the S-stars. This cluster has been the subject of extensive observational and theoretical work, for which we refer the reader to Alexander (2005) and Genzel et al. (2010). The stars are spectroscopically consistent with being late O- to early B-type dwarfs, implying that they have lifetimes that are limited to between $\lesssim 10$ and $400\,\rm Myr$ (Ghez et al. 2003; Eisenhauer et al. 2005; Martins et al. 2008). The upper constraint comes from the limit on the age of a B-type main-sequence star, while the lower constraint comes from the spectroscopic ID of a specific star (S2/S0-2) (Ghez et al. 2003). One particularly interesting question concerns the origin of these stars. There is a consensus in the literature in that they cannot have formed at their current location due to the tidal field of the MBH. Several scenarios incorporating the formation of these stars further out from the MBH, and transport inward through dynamical processes, have been proposed (e.g. Gould & Quillen 2003; Alexander & Livio 2004; Levin 2007; Perets et al. 2007; Löckmann et al. 2008, 2009; Madigan et al. 2009; Merritt et al. 2009; Griv 2010).

---

[6] The absence of a BW cusp in the GC can also simply be explained by the long timescale necessary for steady-state formation; see Appendix 3.B

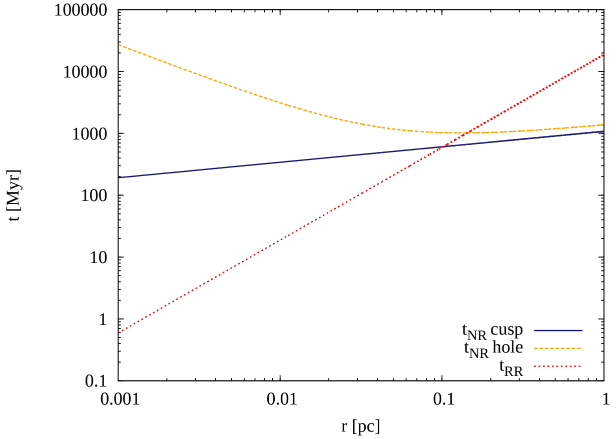

Figure 3.24 – NR (energy) timescale changing in response to the stellar potential ($m = 10M_\odot$) as it develops from a BW cusp to one with a hole in energy space (from $t_{\rm NR}^{\rm cusp}$ to $t_{\rm NR}^{\rm hole}$). The RR timescale is plotted here without GR precession as $M_\bullet/mP$ and, at large radii, does not depend on the number of stars. Hence this timescale should remain constant above $\sim 10^{-2}$ pc as the NR timescale increases. The radius at which $t_{\rm RR}$ is equal to $t_{\rm NR}$ moves outwards in response to the changes and hence the outer radius of the hole in stars will increase.

Many leading hypotheses involve binary disruptions (Hills 1988, 1991). In this scenario a close encounter between a binary system and an MBH leads to an exchange interaction in which one of the stars is captured by the MBH, and the other becomes unbound and leaves the system with a high velocity. For capture, the periapsis r_p of the binary's orbit (with combined mass $m_{\rm bin}$ and semi-major axis $a_{\rm bin}$) must come within the tidal radius

$$r_t = \left(\frac{2M_\bullet}{m_{\rm bin}}\right)^{1/3} a_{\rm bin}. \tag{3.45}$$

The captured star will remain with a semi-major axis $a_{\rm cap}$ that scales as $a_{\rm cap} \sim (M_\bullet/m_{\rm bin})^{2/3} a_{\rm bin}$, and its eccentricity can be approximated as $1 - e \sim (m_{\rm bin}/M_\bullet)^{1/3}$.

A unifying aspect of all proposed formation mechanisms is that none of them lead directly to orbital characteristics that are in agreement with those of the S-stars; in particular, the binary disruption mechanism leads to highly eccentric orbits. Since the local RR time is shorter than the maximum age of the S-stars, it has been suggested that following the arrival of the S-stars on tightly bound orbits to the MBH, a subsequent phase of RR has driven them to their current distribution (Hopman & Alexander 2006; Levin 2007). RR evolution of S-stars has been studied by Perets et al. (2009) by means of direct N-body simulations. They find that high-eccentricity orbits can evolve within a short time (20 Myr), to an eccentricity distribution that is statistically indistinguishable to that of the S-stars. They conclude that the S-star orbital parameters are consistent with a binary disruption formation scenario. However, these simulations do not include GR precession, which we have found to be important for the angular momentum evolution of stars at these radii.

3.7.3.1 Simulations

We use our ARMA code, which includes GR precession, to study the evolution of the S-star orbital parameters within the binary disruption context. We initialize our test stars on high eccentricity orbits, $e = 0.97$ ($m_{\rm bin} \sim 20 M_\odot$), with initial semi-major axes corresponding to those reported by Gillessen et al. (2009) for the S-stars. We assume a distance to SgrA* of $8.0\,{\rm kpc}$ (Eisenhauer et al. 2003; Ghez et al. 2008; Gillessen et al. 2009). For this distance, one arcsecond corresponds to a distance of $0.0388\,{\rm pc}$. We do not include S-stars that are associated with the disk of O/WR stars at larger radii for two reasons. The first is that they most likely originated from the disk with lower initial orbital eccentricities than we simulate here. Second, RR is not the most effective mechanism for angular momentum evolution at their radii; torques from stars at the inner edge of the disk will dominate. We run the simulation one hundred times for each test star to look statistically at the resulting distribution.

We simulate two different initial setups. The first, which we call the *continuous* scenario, assumes that the tidal disruption of binaries is an ongoing process, as is most likely in the case considered by Perets et al. (2007), where individual binaries are scattered into the loss cone by massive perturbers. The same initial conditions also hold if low angular momentum binaries are generated as a result of triaxiality of the surrounding potential. For this study we start evolving the stellar orbits at times that are randomly distributed between $[0, t_{\rm max}]$, and continue the simulation until the time $t = t_{\rm max}$. In our second setup, which we call the *burst* scenario, we consider a situation in which S-stars are formed at once on eccentric orbits at $t = 0$, and follow their evolution until $t = t_{\rm max}$; this enables us to compare directly to the results of Perets et al. (2009) in whose simulations all stars commence their evolution simultaneously. A burst of S-star formation, over a short period of a few ${\rm Myr}$, could for example result from an instability in an eccentric stellar disk (Madigan et al. 2009); we note that the instability is even more effective for a depressed cusp (Madigan 2010).

We use two different models for the galactic nucleus. For each we recompute the ARMA parameters (ϕ, θ, σ) and $t_{\rm NR}$ for the new profile and re-run the MC simulations using Equations (3.39) and (3.40) with the updated values. *Model A* is similar to the galactic nucleus model discussed in Section 3.2. The stellar cusp has a density profile $n(r) \propto r^{-\alpha}$ with $\alpha = 1.75$, and the number of stars is normalized with $N(< 0.01\,{\rm pc}) = 222$ and $m = 10$. We chose this model such that it faithfully reflects the dominant stellar content at a distance of $0.01\,{\rm pc}$, where RR is most important and where the S-stars are located. We use *Model B* to simulate the response of the S-stars to a depression in the GC,

Table 3.3 – S-star Parameters

Model A	$t_{\max}$ (Myr)	6	10	20	100
p^a	Burst[d]	0.012	0.147	0.007	5e-4
	Continuous[e]	2e-4	0.002	0.05	0.02
$f > 0.97^b$	Burst	.40	.29	.24	.07
	Continuous	.47	.40	.33	.16
DR[c]	Burst	.23	.32	.46	.72
	Continuous	.09	.17	.29	.55
Model B					
p^a	Burst	0.002	0.04	0.100	0.0005
	Continuous	1.5e-5	0.0002	0.006	0.06
$f > 0.97^b$	Burst	.45	.35	.22	.07
	Continuous	.50	.47	.38	.19
DR[c]	Burst	.17	.29	.45	.70
	Continuous	.08	.16	.26	.55

Notes

[a] Two-dimensional (a, e) Kolmogorov-Smirnov p-values.

[b] Fraction of S-stars with $e > 0.97$ at end of simulation.

[c] Disruption rate (fraction) of S-stars.

[d] Stars initialized at $t = 0$.

[e] Stars randomly initialized between $[0, t_{\max}]$.

as found in the previous section. This model has a smaller density power-law index of $\alpha = 0.5$ (which is within the 90% boundaries of the bootstrapped values for α in the GC as found by Merritt (2010)) and $N(< 0.01\,\mathrm{pc}) = 148$. Less mass at small radii leads to slower mass precession, pushing to a lower eccentricity the value at which mass precession cancels with GR precession; see Figure 3.16 for an illustration of this effect where $\alpha = 1.75$. Interestingly for all values of $N(< 0.01\,\mathrm{pc}) \lesssim 120$, this eccentricity lies at ~ 0.7 a location in eccentricity space where we do not observe S-stars, which causes a flattening of the observed cumulative distribution.

3.7.3.2 Results

For both models we find the cumulative eccentricity distribution of the stars at different times and compare them to the observed distribution from Gillessen et al. (2009); see Figures 3.25 and 3.26. In Table 3.3, we present results from nonparametric two-dimensional, two-sample, Kolmogorov-Smirnov (2DKS) testing[7] between the observed cumulative distribution and the simulations. The two-sample KS test checks whether two data samples come from different distributions (low p values).

We also give the fraction of stars that have an eccentricity $e > 0.97$ at the end of the simulation. The total disruption rate (DR) gives an indication of how many progenitors would be needed to make up the population of S-stars observed today.

---

[7] We use a version due to Fasano & Franceschini (1987). See also Peacock (1983).

Model A: The best fit to the S-star observations are for the *burst* scenario with $t_{\rm max} = 6 - 10\,{\rm Myr}$. Greater values of $t_{\rm max}$ produce too many low eccentricity stars in our simulations; as the RR time is longer at these eccentricities stars will tend to remain at these low values. In the *continuous* scenario the simulations conclude with many more high eccentricity stars as they do not have as much time to move away from their original eccentricities. Hence the best-fit result for this scenario is $t_{\rm max} = 10 - 20\,{\rm Myr}$. In both cases the 2DKS p-values $\ll 1$, suggesting that no simulated distribution matches very well the observed. Both scenarios predict a large number $(7 - 45\%)$ of high eccentricity stars with $e > 0.97$.

Model B: The best match to the observations is the *burst* scenario with $t_{\rm max} = 20\,{\rm Myr}$, though the *continuous* scenario has a relatively high p-value at a time of $t_{\rm max} = 100\,{\rm Myr}$. In both cases a longer $t_{\rm max}$ is preferred as this model has less mass, and hence GR precession will dominate the precession rate of these stars down to lower eccentricities, rendering RR less effective at high eccentricities. Again the p-values are low in most cases due to the excess of high eccentricity orbits relative to the observations.

For both models, simulations with $t_{\rm max} > 100\,{\rm Myr}$ produce too many low eccentricity stars with respect to the observations. Simulations with $t_{\rm max} = 200 - 400\,{\rm Myr}$ have increasingly smaller p-values for this reason. The small number of observed low eccentricity S-stars could in principle constrain the time S-stars have spent at these radii (their "dynamical lifetimes"). Although the S-stars can in theory have ages up to $\sim 400\,{\rm Myr}$, we find that, in the binary disruption context, their dynamical lifetimes at these radii are $< 100\,{\rm Myr}$. Furthermore, as noted by Perets et al. (2009), the lack of observed low eccentricity S-stars is difficult to reconcile with formation scenarios which bring the stars to these radii on initially low eccentricity orbits. The RR timescale $t_{\rm rr}$ is long and stars will retain their initial values for long times.

For all values of $t_{\rm max}$ there is a clear discrepancy between the lack of high eccentricity S-stars orbits observed and the results from both formation scenarios and models. To further illustrate this problem we show a scatter plot from our simulations in Figure 3.27, of eccentricity e as a function of semi-major axis a after $6\,{\rm Myr}$. We over-plot the observed S-star parameters, indicating separately those associated with the disk. It is clear that while the simulations can reproduce the range of (a, e) in which the S-stars are observed, our theory over-predicts the amount of high eccentricity orbits with respect to the observations. Such orbits at these radii are expected; stars with high orbital eccentricities, although they experience large torques (Equation (4.6)), have short coherence times (Equation (3.28)) and hence long RR times (Equation (3.30)). Consequently, their angular momentum evolution is sluggish. At any given time, we would expect to see a population of stars in this region. Therefore, we find it difficult to explain why so few high eccentricity S-stars have been observed; the maximum is $e = 0.963 \pm 0.006$ (S14; Gillessen et al. 2009); $e = 0.974 \pm 0.016$ (S0-16; Ghez et al. 2005).

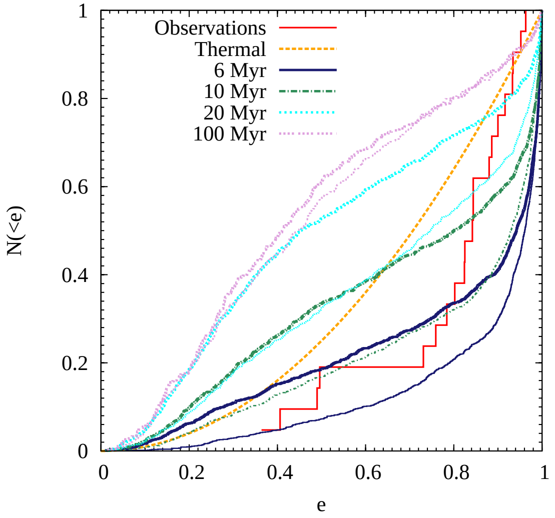

Figure 3.25 – Cumulative distribution of eccentricities for the *burst* scenario in which the stars' initial time is zero. The red step function is the observed cumulative eccentricity distribution of S-stars in the GC as found by Gillessen et al. (2009). The dashed orange line is a thermal distribution $N(< e) = e^2$. The other lines are results from MC simulations, where the evolution time $t_{\max}$ and eccentricity e are indicated in the legend. Thick (thin) lines are the results for Model A (B).

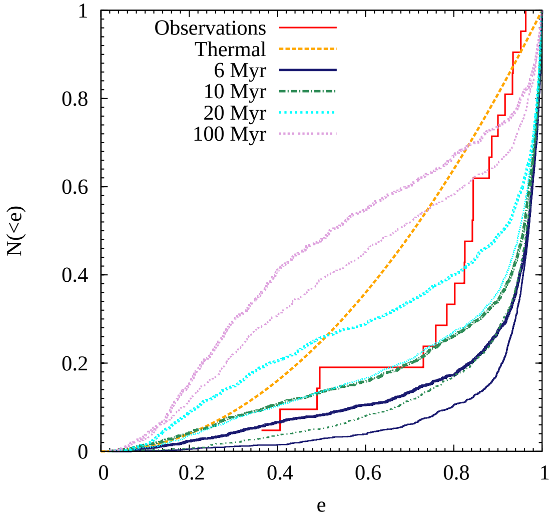

Figure 3.26 – Cumulative distribution of eccentricities for the *continuous* scenario in which the stars' initial time t is randomly distributed between $[0, t_{\max}]$. The red step function is the observed cumulative eccentricity distribution of S-stars in the GC from Gillessen et al. (2009). The dashed orange line is a thermal distribution $N(< e) = e^2$. The other lines are results from MC simulations, where the maximum evolution time $t_{\max}$ and initial eccentricity e are indicated in the legend. Thick (thin) lines are the results for Model A (B).

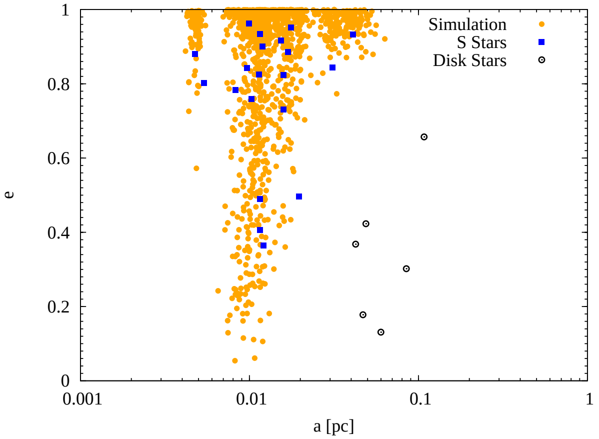

Figure 3.27 – Scatter plot of eccentricity, e, of the S-stars, as a function of semi-major axis, a, on a log scale for the Model B *burst* scenario. The small orange dots represent the results of our simulations after $6\,\mathrm{Myr}$, the blue squares are data from Gillessen et al. (2009) and the black open circles are those S-stars consistent with being members of the CW disk.

An interesting solution to this problem is that there *are* S-stars with higher orbital eccentricities but that their orbital elements have not yet been determined due to the observational detection limits for stellar accelerations. Schödel et al. (2003) show that there is a bias against detecting high eccentricity orbits at the average S-star radius of $0.01\,\mathrm{pc}$ (see their Figure 14). Future observations will be able to reveal if this can account for the discrepancy (Weinberg et al. 2005). The solution on the other hand may involve a new stellar dynamical mechanism which is not accounted for in our ARMA model. Merritt et al. (2011) have recently discovered a new dynamical barrier in angular momentum space, termed the “Schwarzschild barrier”, which can reflect stars orbiting close to the MBH from very high eccentricity orbits ($e > 0.99$) to less eccentric ones. This could well explain why not so many S-stars have been observed on highly eccentric orbits as RR alone predicts.

3.8 Summary

We have used several techniques to study the angular momentum evolution of stars orbiting MBHs, with a focus on secular effects. First, we carried out N-body simulations to generate time series of angular momentum changes for stars with various initial eccentricities. We quantified the evolution in an ARMA(1, 1) model. We then used this model to generate new, much-longer time series in our MC code, which enabled us to study the steady-state distribution of stellar orbits around an MBH, and the evolution of the angular momentum distribution of possible progenitors of the S-stars.

We have shown that the steady-state angular momentum distribution of stars around an MBH is not isotropic when RR is a dominant relaxation mechanism. For the GC this corresponds to the innermost couple of tenths of parsecs. We note that Schödel et al. (2009) find a slight degree of anisotropy in the velocity distribution of late-type stars in the GC within the innermost $6''$ ($\sim 0.2\,\mathrm{pc}$). It is of particular interest to note that close to the MBH, we find that the angular momentum distribution rises more steeply than a linear distribution, which may have consequences for the stability of the system. Tremaine (2005) and Polyachenko et al. (2007) showed that if (1) the distribution rises faster than linearly, and (2) the distribution of angular momenta vanishes at $J = 0$, the system is only neutrally stable (or even unstable if it is flattened). The second condition is also satisfied, because of the presence of the loss cone: $N = 0$ for $J < J_{lc}$. In a later paper, Polyachenko et al. (2008) found that a non-monotonic distribution of angular momenta is required for the system to develop a “gravitational loss cone instability”. This condition is also satisfied for a range of energies. An assessment of the importance and consequences of these instabilities is beyond the scope of this work.

We have furthermore demonstrated the presence of a depression in the distribution of stars near MBHs due to resonant tidal disruption. This depression forms on a timescale shorter than the Hubble time, even though a steady-state solution may not yet be reached. While it is tempting to invoke this mechanism to explain the “hole” in late-type stars in the GC, we stress that our fiducial galactic nucleus model, a single-mass BW distribution of stars around an MBH, is greatly simplified compared to reality and produces an outer hole radius which is too small to explain the observations. We expect the GC to be far more complex, with ongoing star formation, multi-mass stellar populations, mass segregation, physical collisions between stars and additional sources of relaxation (e.g., the circumnuclear ring, the CW disk). Nevertheless, there is merit to our approach: even with our simplified picture, we illustrate the importance of RR on stellar dynamics close to an MBH.

Finally we have shown that the (a, e) distribution of the S-stars does not match that expected by the binary disruption scenario in which the stars start their lives on highly eccentric orbits and evolve under the RR mechanism. We surmise that there are a number of high eccentricity S-stars whose orbital parameters have not yet been derived, though the “Schwarzschild barrier” recently discovered by Merritt et al. (2011) may provided a dynamical solution to this problem. We have confirmed the result by Perets et al. (2009) in that it is unlikely that the S-stars were formed on low eccentricity orbits. We place a constraint on the dynamical age of the S-stars of $100\,\mathrm{Myr}$ from the small number of low eccentricity orbits observed.

Acknowledgments A.M. is supported by a TopTalent fellowship from the Netherlands Organisation for Scientific Research (NWO), C.H. is supported by a Veni fellowship from NWO, and Y.L. by a VIDI fellowship from NWO. We are very grateful to Atakan Gürkan for his significant contribution to this project. A.M. thanks Andrei Beloborodov, Pau Amaro-Seoane and Eugene Vasiliev for stimulating discussions. We thank Tal Alexander and Ben Bar-Or for their comments on the first draft of this chapter, particularly with respect to energy diffusion. Finally, we thank the anonymous referee for a comprehensive reading of this chapter and insightful comments.

3.A Description of N-body code

We have developed a new integrator, specifically designed for stellar dynamical simulations in near-Keplerian potentials. A distinctive feature of this code is the separation between "test" particles and "field" particles (see, e.g., Rauch & Tremaine 1996). The field particles are not true N-body particles; they move on Keplerian orbits which precess according to an analytic prescription (see Equation (3.62)), and do not directly react to the gravitational potential from their neighbors. Conversely, the test particles are true N-body particles, moving on Keplerian orbits and precessing due to the gravitational potential of all the other particles in the system. This reduces the force calculation from $O(N^2) \to O(nN)$, where N is the number of field particles and n is the number of test particles in the simulation. Both test and field particles' orbits precess due to GR effects. The stellar orbits rotate in their planes at each time-step dt by an angle $|\delta\phi| = 2\pi(dt/t_{\rm prec}^{\rm GR})$, with $t_{\rm prec}^{\rm GR}$ given by Equation (3.26).

The main difference between our code and many others, is that instead of considering perturbations on a star moving on a straight line with constant velocity, we consider perturbations on a star moving on a precessing Kepler ellipse. Our algorithm is based on a mixed-variable symplectic method (Wisdom & Holman 1991; Kinoshita et al. 1991; Saha & Tremaine 1992), so called due to the switching of the coordinate system from Cartesian (in which the perturbations to the stellar orbit are calculated) to one based on Kepler elements (to determine the influence of central Keplerian force). These forms of symplectic integrator split the Hamiltonian, H, of the system into individually integrable parts, namely a dominant Keplerian part due to the central object, i.e., MBH, and a smaller perturbation part from the surrounding particles, i.e., stellar cluster,

$$H = H_{\rm Kepler} + H_{\rm interaction}. \tag{3.46}$$

The algorithm incorporates the well-known leapfrog scheme where a single time step (τ) is composed of three components, kick ($\tau/2$)-drift (τ)-kick ($\tau/2$). The *kick* stage corresponds to $H_{\rm interaction}$ and produces a change of momenta in fixed Cartesian coordinates. The *drift* stage describes motion under $H_{\rm Kepler}$ and produces movement along unperturbed Kepler ellipses. To integrate along these ellipses, we exploit the heavily-studied solutions to Kepler's equation. This is a less computationally efficient method than direct integration, but accurate to machine precision. This is of utmost importance in simulations involving RR as spurious precession due to build-up in orbital integration errors will lead to erroneous results. The computation is performed in Kepler elements, using Gauss' f and g functions. We use universal variables which allow the particle to move smoothly between elliptical, hyperbolic, and parabolic orbits, making use of Stumpff functions. For details we refer the reader to Danby (1992). For the simulations presented in this chapter, we use a fourth-order integrator (Yoshida 1990) which is achieved by concatenating second order leapfrog steps in the ratio $(2-2^{1/3})^{-1} : -2^{1/3}(2-2^{1/3})^{-1} : (2-2^{1/3})^{-1}$.

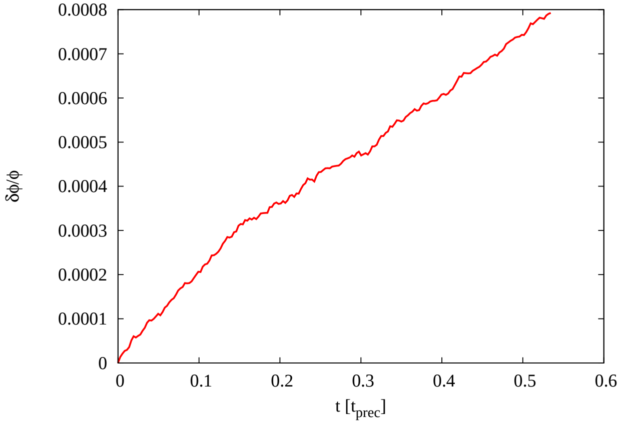

Figure 3.28 – Fractional difference between the theoretical value for apsidal precession and that achieved by our integrator for a test star of eccentricity $e = 0.99$ as a function of time in units of the precession time of the test-star. The angle through which the test star has precessed is given by ϕ. The analytical formula is adjusted for the test star's wandering in semi-major axis.

We use adaptive time stepping to resolve high eccentricity orbits at periapsis, and to accurately treat close encounters between particles, hence our integrator is not symplectic. To reduce the energy errors incurred with the loss of symplecticity, we implement time symmetry in the algorithm. These steps must be sufficient to avoid artificial apsidal precession of stellar orbits, particularly at high eccentricity where Wisdom-Holman integrators are known to perform poorly (Rauch & Holman 1999). To demonstrate this we compare the rate of change, as a function of time, of the direction of the eccentricity vector of a test star using our N-body integrator with our analytical prediction. Figure 3.28 shows our results in terms of the angle through which the test star has precessed, ϕ, for $e = 0.99, a = 0.01$ pc orbits in the gravitational potential as described in Section 3.2.1. We take the average of nine simulations for half a precession time of the test star. Extrapolating to a full precession time we find a fractional difference of $\delta\phi/\phi = 0.00148$ between our analytical estimate and that of the test star precession rate. This verifies that the long RR timescale at high eccentricities, as shown in Figure 3.3, is not a result of artificial rapid apsidal precession. To further demonstrate the accuracy of the integrator with respect to the apsidal precession rate, we run additional calibration simulations for high-eccentricity orbits ($e = 0.96, 0.98$) in order to compare their angular momentum relaxation timescale (calculated using Equation (3.5)) with the formula we derive for RR in Equation (3.30). Figure 3.29 demonstrates the agreement between increase of the RR timescale with eccentricity as retrieved from the simulations and that expected from theory.

An additional feature of the code is the option to implement "reflective"

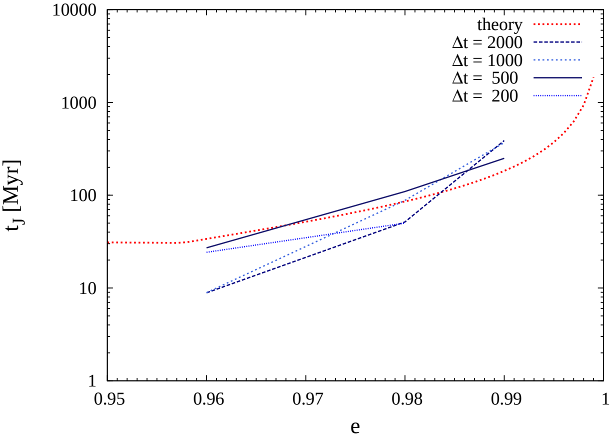

Figure 3.29 – Timescale for angular momentum J changes of the order of the circular angular momentum for massless test stars in our N-body simulations, presented on a log scale of time in units of Myr; see Equation (3.6). We take several Δt values to get order-of-magnitude estimates for this timescale. Over-plotted in red is the theoretical expectation for this timescale based on Equation (3.30).

walls, which bounce field particles back into the sphere of integration. Without these walls, particles on eccentric orbits nearing apoapsis move outside the sphere of interest and alter the density profile of the background cluster of particles, and hence the (stellar) potential. With the walls "on", a particle reaching the reflective boundary is reflected directly back but with a different random initial location on the sphere, to avoid generating fixed orbital arcs in the system which would artificially enhance RR. The reflective walls are most useful in situations where we want to examine how a test particle reacts in a defined environment with a specific background (stellar) potential. The prescription we use for the time step (τ) is based on orbital phase, the collisional timescale between particles and free-fall timescale between particles. We treat gravitational softening between particles with the compact K_2 kernel (Dehnen 2001). We have parallelized our code for shared-memory architecture on single multiple-core processors using OPENMP.

3.B Energy evolution and cusp formation

Many different definitions of relaxation times are used in the literature. In Section 3.2.2 we consider the energy diffusion timescale t_E, defined as $t_E \equiv E^2/D_{\mathrm{EE}}$ where $D_{\mathrm{EE}} \equiv \langle(\Delta E)^2\rangle/\Delta t$ is the energy diffusion coefficient. This is the timescale for order unity steps in energy. In order to be explicit, we now compare our timescale (see Figure 3.3 and Equation (3.5)) with a commonly used reference time for relaxation processes defined in Spitzer (1987):

$$\begin{aligned} t_r &= \frac{1}{3}\frac{v_M^2}{\langle(\Delta v_{||})^2\rangle_{v=v_M}} \\ &= 0.065\frac{v_M^3}{(Gm)^2 n \ln\Lambda}. \end{aligned} \tag{3.47}$$

We note that this is equivalent to the timescale given by Binney & Tremaine (2008) for a Maxwellian velocity distribution, $v_M = \sqrt{3}\sigma$, where $v_M(r)$ is the mean velocity of a star and $\sigma(r)$ is the one-dimensional velocity dispersion of the stellar distribution at radius r,

$$t_r = \frac{0.34\sigma^3}{(Gm)^2 n \ln\Lambda}. \tag{3.48}$$

The velocity dispersion within a stellar cusp with power-law density profile $n(r) \propto r^{-\alpha}$ can be calculated from the Jeans equation for spherical isotropic systems as

$$\sigma^2(r) \equiv -\frac{G}{n(r)}\int_0^r \frac{dr' M(r')n(r')}{r'^2} = \frac{1}{1+\alpha}v_c^2 \tag{3.49}$$

where $M(r)$ is the mass within a radius r and v_c is the circular velocity. For the comparison of t_E and t_r we take Keplerian parameters for the circular velocity at a given radius such that

$$\sigma^2 = \frac{1}{1+\alpha}\frac{GM_\bullet}{r} \tag{3.50}$$

(Alexander 2003), and set the Coulomb logarithm to $\Lambda = M_\bullet/m$ (Bahcall & Wolf 1976). For the cusp model used in our N-body simulations we find from Equations (3.22) and (3.48)

$$t_E \equiv \frac{E^2}{D_{\mathrm{EE}}} = 0.26\left(\frac{M_\bullet}{m}\right)^2 \frac{1}{N_<}\frac{1}{\ln\Lambda}P = 2.18\, t_r, \tag{3.51}$$

with $t_r = 156\,\mathrm{Myr}$, $t_E = 340\,\mathrm{Myr}$ for $r = 0.01\,\mathrm{pc}$. Thus with this definition, the energy of a star changes by order unity in roughly twice a relaxation time.

We compare our result for the energy relaxation time to that found by Eilon et al. (2009) using an entirely different integrator. Their N-body simulations incorporate a fifth-order Runge-Kutta algorithm with optional pairwise KS regularization (Kustaanheimo & Stiefel 1965), without the need for gravitational softening. We use their numerically derived value (see their Table 1) of $\langle\alpha\rangle \equiv \langle\alpha_\Lambda/\sqrt{\ln\Lambda}\rangle$, averaged over all stars in the cluster, and their expression for the energy relaxation time $T^E_{\mathrm{NR}} = (M_\bullet/m)^2 P/(N\alpha_\Lambda^2)$, and compare with our Equation (3.22) with its own numerically derived parameter. We find an energy relaxation timescale which is a factor of $\sim$ four longer than in their

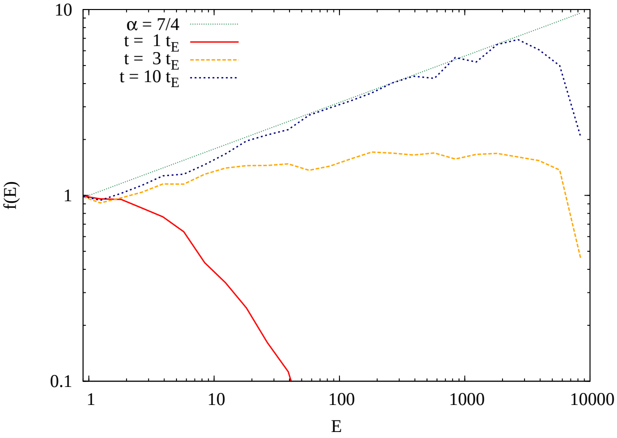

Figure 3.30 – Stellar distribution function $f(E)$ for single mass stars as a function of energy E for different times $t = (1 - 10)\ t_E$, where t_E is the Keplerian energy diffusion timescale evaluated at $E = 1$. steady-state is reached within $10\ t_E$, the solution of which is a BW cusp with $\alpha = 7/4$, represented by the dotted green line.

paper (i.e., their energy diffusion timescale is about half of t_r). Our maximum radius at $0.03\ \mathrm{pc}$ means we do not simulate several “octaves” in energy space which could contribute to energy relaxation. In a Keplerian cusp, the variance in the velocity changes of a star, $(\Delta v)^2$, is not independent of radius r but scales with the power-law density index α. In our simulations $\alpha = 7/4$, and hence the number of octaves from the cutoff radius, $r = 0.03\ \mathrm{pc}$, out to the radius of influence, $r_h = 2.31\ \mathrm{pc}$, can account for at most a factor of $\sim$ two difference in t_{E}. The inner cutoff radius at $r = 0.003\ \mathrm{pc}$ contributes a smaller factor of difference to the energy diffusion timescale.

We now consider the timescale for building a cusp due to energy diffusion. For this purpose, we use our MC code without angular momentum evolution. In Figure 3.30, we show the distribution function for several times, where the system was initialized such that all stars start at $E = 1$, corresponding to half the radius of influence. *From this figure, we find that it takes about* $10\ t_E(E = 1, r = 0.5\ r_h)$ *or 8* $t_E(r = r_h)$ *to form a cusp.* The result that it takes much longer than t_E is also implicitly found in Bahcall & Wolf (1976). They give an expression for D_{EE} (called $c_2(E,t)$ in their paper); evaluating the pre-factor in their expression due to only the contribution of bound stars in steady-state, one finds that $c_2(E = 1) = 16/t_{\mathrm{cusp}}^{\mathrm{BW}}$, where $t_{\mathrm{cusp}}^{\mathrm{BW}}$ is the reference time in which Bahcall & Wolf (1976) find a cusp is formed.

Baumgardt et al. (2004) and Preto et al. (2004) were the first to show the formation of a cusp in direct N-body simulations. We use Equations (3.48) and (3.51) to calculate the cusp formation times in Table 1 of Preto et al. (2004)

in terms of our energy diffusion time. We find that in their simulations a cusp forms on a timescale of the order of $10\ t_E$. We conclude that energy diffusion proceeds in their simulations at a rate similar to ours. However, Preto et al. (2004) state that a cusp forms within one relaxation time. These two statements, apparently contradictory, are reconciled in two ways. First, Preto et al. (2004) define the relaxation time at a radius such that the mass in stars is equal to twice that of the MBH. Second, they include the non-Keplerian potential in their calculation of the relaxation time. It is valid to assume Keplerian parameters for the stellar velocity dispersion at the distances we are interested in close to the MBH. However, neglecting the contribution of the surrounding stellar mass leads to a significant numerical difference in the calculation of the relaxation time near the radius of influence compared with those which incorporate the non-Keplerian potential.

To verify this, and to reconcile our conclusions, we adapt our definition of the energy diffusion time by incorporating the non-Keplerian potential,

$$v_c^3 = \left(\frac{G[M_\bullet + M(<r)]}{r}\right)^{3/2} = \left(\frac{GM_\bullet}{r}\right)^{3/2}\left[1 + \frac{M_h}{M_\bullet r_h^{3-\alpha}} r^{3-\alpha}\right]^{3/2}, \tag{3.52}$$

$$t'_{\mathrm{E}} = \left(1 + AE^{\alpha-3}\right)^{3/2} t_E, \tag{3.53}$$

where $A = 2^{\alpha-3} M_h/M_\bullet$, M_h is the mass inside the radius of influence r_h, t'_{E} is the new energy diffusion timescale and we have used the relation $E = r_h/2a$. The new energy diffusion coefficient is

$$D'_{\mathrm{EE}} = \left(1 + AE^{\alpha-3}\right)^{-3/2} D_{\mathrm{EE}}. \tag{3.54}$$

In Figure 3.31 we show the results of MC simulations in which the new energy diffusion coefficient is used. The system was again initialized such that all stars start at $E = 1$. A BW cusp ($\alpha = 7/4$) forms in about one relaxation time evaluated at $E = 0.287$, the energy at which $M_h = 2M_\bullet$. This result emphasizes the importance of taking the stellar potential into account for the relaxation timescale.

For a simplistic single mass ($m = 1\,M_\odot$) GC model (see Section 3.2.1), we find that at the radius of influence the Keplerian energy diffusion timescale is $t_E = 12\,\mathrm{Gyr}$ and a cusp forms in $\sim 100\,\mathrm{Gyr}$. Alternatively we find from Equation (3.53) a cusp formation time of $t'_E \sim 90\,\mathrm{Gyr}$. We stress that the time for cusp formation is much longer than the Hubble time, even if we halve it to account for the outer cutoff in radius in our N-body simulations which suppresses the energy diffusion timescale. This is in contradiction to what is often claimed; one cause of the discrepancy is that in, for example, Bahcall & Wolf (1976) and Lightman & Shapiro (1977), energy diffusion proceeds at a rate exceeding the relaxation rate by a factor > 10, in contrast to what we find in our N-body simulations. We note here that if energy diffusion did in

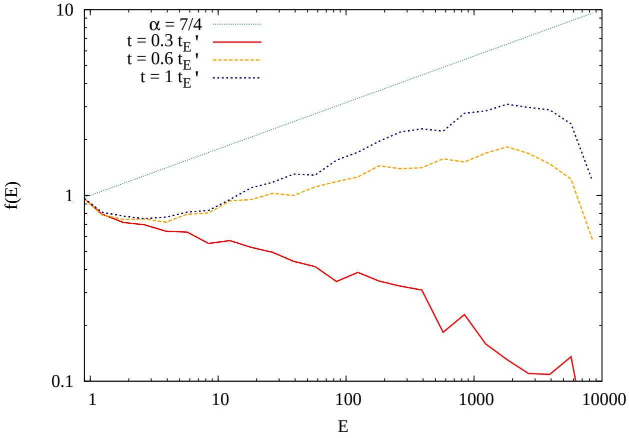

Figure 3.31 – Stellar distribution function $f(E)$ for single mass stars as a function of energy E for different times $t = (0.3 - 1)\ t'_E$, where t'_E is the energy diffusion timescale which incorporates the non-Keplerian stellar potential and is evaluated at $E = 0.287, r = 4.023$ pc. The stars start in a delta function at $E = 1$ (and hence generate an artificial peak at this position) and form a cusp within one relaxation time $1\ t'_E$.

fact proceed at this higher rate, then the energy diffusion timescale for the S-stars in the GC would be on the order of $\sim 20\,\mathrm{Myr}$ which would have profound consequences for the (E, J) evolution of the cluster. It thus appears that the GC cannot have reached a steady-state (see also Merritt 2010), even though mass-segregation enhances the rate of cusp formation by a factor of a few (Preto & Amaro-Seoane 2010; Hopman & Madigan 2010).

3.C Precession due to power-law stellar cusp

The presence of a nuclear stellar cluster in the vicinity of an MBH adds a small correction $\delta U(r)$ to the Keplerian gravitational potential energy $U = -\alpha/r$ of the system. As a consequence, paths of finite motion (i.e., orbits) are no longer closed, and with each revolution the periapsis of a star is displaced through a small angle $\delta\phi$. Given a power-law density profile of the stellar cluster $n(r) \propto r^{-\alpha}$, we can calculate this angle using the formula

$$\delta\phi = \frac{\partial}{\partial L}\left(\frac{2}{L}\int_0^{\pi} r^2 \delta U d\phi\right), \tag{3.55}$$

where $L = \sqrt{GM_\bullet a\left(1-e^2\right)}$ is the unnormalized angular momentum of a Keplerian orbit (Landau & Lifshitz 1969). We continue to use specific parameters in the following equations. The stellar mass within radius r is

$$M(r) = M_0\left(\frac{r}{r_0}\right)^{3-\alpha}, \tag{3.56}$$

M_0, r_0 being proportionality constants which we normalize to the radius of influence, $r_0 = r_h$, $M_0 = M_\bullet$. Thus the potential felt by a massless particle due to this enclosed mass is

$$\begin{aligned}\delta U &= -\int_0^r F(r')\partial r' \\ &= \frac{GM_\bullet r_h^{\alpha-3}}{(2-\alpha)} r^{2-\alpha} \quad (\alpha \neq 2).\end{aligned} \tag{3.57}$$

Inserting δU into Equation (3.55) yields

$$\delta\phi = \frac{GM_\bullet r_h^{\alpha-3}}{(2-\alpha)} \frac{\partial}{\partial L}\left(\frac{2}{L}\int_0^\pi r^{4-\alpha} d\phi\right). \tag{3.58}$$

We apply a change of coordinates here, replacing L with normalized angular momentum $J = \sqrt{1-e^2}$, such that $L = \sqrt{GM_\bullet a}J$. Expressing radius r in terms of Kepler elements, semi-major axis a, eccentricity e and angle from position of periapsis ϕ,

$$r = a\frac{1-e^2}{1+e\cos\phi} = a\frac{J^2}{1+\sqrt{1-J^2}\cos\phi}, \tag{3.59}$$

yields

$$\begin{aligned}\delta\phi &= \frac{2}{(2-\alpha)}\left(\frac{a}{r_h}\right)^{3-\alpha} f(e,\alpha) \\ &= \frac{2}{(2-\alpha)} f(e,\alpha)\left[\frac{N_< m}{M_\bullet}\right],\end{aligned} \tag{3.60}$$

where m is the mass of a single star, $N_<$ is the number enclosed within radius r and

$$f(e,\alpha) = \frac{\partial}{\partial J}\left(\frac{1}{J}\int_0^\pi \left[\frac{J^2}{1+\sqrt{1-J^2}\cos\phi}\right]^{4-\alpha} d\phi\right). \tag{3.61}$$

The function $f(e,\alpha)$ is calculated numerically, and fit, for a given α. This returns a cluster precession time of

$$t_{\rm prec}^{\rm cl} = \pi(2-\alpha)f(e,\alpha)^{-1}\left[\frac{M_\bullet}{N_< m}P(a)\right] \quad (\alpha \neq 2), \tag{3.62}$$

where $P(a)$ is the period of an orbit with semi-major axis a.

3.D Equations of ARMA(1,1) model

We will use Equations (3.8) and (3.9) in our calculations; for clarity we repeat them here, dropping the label “1”,

$$\Delta J_t = \phi\Delta J_{t-1} + \theta\epsilon_{t-1} + \epsilon_t, \tag{3.63}$$

$$\langle\epsilon\rangle = 0; \quad \langle\epsilon_t\epsilon_s\rangle = \sigma^2\delta_{t,s}. \tag{3.64}$$

3.D.1 Variance

$$\begin{aligned}\langle\Delta J_t^2\rangle = \phi^2\langle\Delta J_{t-1}^2\rangle + 2\phi\theta\langle\Delta J_{t-1}\epsilon_{t-1}\rangle + 2\phi\langle\Delta J_{t-1}\epsilon_t\rangle \\ + \theta^2\langle\epsilon_{t-1}^2\rangle + 2\theta\langle\epsilon_{t-1}\epsilon_t\rangle + \langle\epsilon_t^2\rangle\end{aligned} \tag{3.65}$$

Using $\langle\Delta J_t^2\rangle = \langle\Delta J_{t-1}^2\rangle$, expanding ΔJ_{t-1} in the second and third terms, and applying $\langle\epsilon_t\epsilon_s\rangle = \sigma^2\delta_{t,s}$ yields

$$\langle\Delta J_t^2\rangle(1-\phi^2) = \sigma^2(2\phi\theta + \theta^2 + 1), \tag{3.66}$$

which returns Equation (3.10):

$$\langle\Delta J_t^2\rangle = \frac{1+\theta^2+2\theta\phi}{1-\phi^2}\sigma^2. \tag{3.67}$$

3.D.2 Autocorrelation function

The ACF for the ARMA model as described by Equation (3.63), is defined as

$$\rho_t = \frac{\langle\Delta J_{s+t}\Delta J_s\rangle}{\langle\Delta J_t^2\rangle} \quad (t>0). \tag{3.68}$$

Expanding the numerator gives

$$\begin{aligned}\langle\Delta J_{s+t}\Delta J_s\rangle = \phi^2\langle\Delta J_{s+t-1}\Delta J_{s-1}\rangle + \phi\theta\langle\Delta J_{s+t-1}\epsilon_{s-1}\rangle \\ + \phi\langle\Delta J_{s+t-1}\epsilon_s\rangle + \phi\theta\langle\Delta J_{s-1}\epsilon_{s+t-1}\rangle \\ + \phi\langle\Delta J_{s-1}\epsilon_{s+t}\rangle + \theta^2\langle\epsilon_{s+t-1}\epsilon_{s-1}\rangle \\ + \theta\langle\epsilon_{s+t-1}\epsilon_s\rangle + \theta\langle\epsilon_{s+t}\epsilon_{s-1}\rangle + \langle\epsilon_s\epsilon_{s+t}\rangle,\end{aligned} \tag{3.69}$$

where $\langle\Delta J_{s+t}\Delta J_s\rangle = \phi^2\langle\Delta J_{s+t-1}\Delta J_{s-1}\rangle$. Recursively expanding the ΔJ terms, and again using $\langle\epsilon_t\epsilon_s\rangle = \sigma_1^2\delta_{t,s}$, reduces the fourth and fifth terms to zero, and greatly simplifies the expression to

$$\langle\Delta J_{s+t}\Delta J_s\rangle = \frac{\sigma^2\phi^t(\theta+\phi)(\theta+1/\phi)}{1-\phi^2}. \tag{3.70}$$

Normalizing by the variance returns Equation (3.11):

$$\rho_t = \phi^t\left[1 + \frac{\theta/\phi}{1+(\phi+\theta)^2/(1-\phi^2)}\right] \qquad (t>0). \tag{3.71}$$

3.D.3 Variance at coherence time t_ϕ

To calculate the variance at the coherence time, $\langle\Delta J_\phi^2\rangle$, we begin by calculating the variance after some time t,

$$\begin{aligned}\left\langle\left(\sum_{n=0}^{t}\Delta J_n^2\right)\right\rangle &= \int_0^t\int_0^t\langle\tau(t_1)\tau(t_2)\rangle dt_1 dt_2 \\ &= \langle\Delta J_t^2\rangle\int_0^t\int_0^t\rho_{(t_1-t_2)}dt_1 dt_2.\end{aligned} \tag{3.72}$$

Here $\rho_{(t_1-t_2)}$ is the ACF of the torque at $(t_1 - t_2) > 0$, normalized with $\langle \Delta J_t^2 \rangle$ to be comparable with Equation (3.11),

$$\rho_{(t_1-t_2)} = \phi^{(t_1-t_2)} \left[1 + \frac{\theta/\phi}{1 + (\phi+\theta)^2/(1-\phi^2)} \right]. \tag{3.73}$$

From Equation (3.31) we can write

$$\phi^{(t_1-t_2)} = \exp\left[-\frac{(t_1-t_2)}{t_\phi} \right]. \tag{3.74}$$

Inserting this into Equation (3.72), writing

$$A = \langle \Delta J_t^2 \rangle \left[1 + \frac{\theta/\phi}{1 + (\phi+\theta)^2/(1-\phi^2)} \right] \tag{3.75}$$

and taking an upper limit of $t = t_\phi$ yields

$$\begin{aligned} \langle \Delta J_\phi^2 \rangle &= A \int_0^{t_\phi} dt_1 \int_0^{t_\phi} \exp\left[-\frac{(t_1-t_2)}{t_\phi} \right] dt_2 \\ &= \sigma^2 \left(\frac{t_\phi}{P} \right)^2 \frac{(\theta+\phi)(\theta+1/\phi)}{1-\phi^2}. \end{aligned} \tag{3.76}$$

where we have approximated $(e + 1/e - 2) \approx 1$.

References

Aarseth, S. J. 2007, MNRAS, 378, 285
Alexander, T. 2003, in The Galactic Black Hole, ed. H. Falcke & F. Hehl (Bristol: Institute of Physics), 246–275
—. 2005, Phys. Rep., 419, 65
Alexander, T. & Hopman, C. 2009, ApJ, 697, 1861
Alexander, T. & Livio, M. 2004, ApJ, 606, L21
Bahcall, J. N. & Wolf, R. A. 1976, ApJ, 209, 214
—. 1977, ApJ, 216, 883
Bartko, H., Martins, F., Trippe, S., Fritz, T. K., Genzel, R., Ott, T., Eisenhauer, F., Gillessen, S., Paumard, T., Alexander, T., Dodds-Eden, K., Gerhard, O., Levin, Y., Mascetti, L., Nayakshin, S., Perets, H. B., Perrin, G., Pfuhl, O., Reid, M. J., Rouan, D., Zilka, M., & Sternberg, A. 2010, ApJ, 708, 834
Baumgardt, H., Gualandris, A., & Portegies Zwart, S. 2006, MNRAS, 372, 174
Baumgardt, H., Makino, J., & Ebisuzaki, T. 2004, ApJ, 613, 1133
Binney, J. & Tremaine, S. 2008, Galactic Dynamics, Second edition (Princeton, NJ: Princeton University Press)
Buchholz, R. M., Schödel, R., & Eckart, A. 2009, A&A, 499, 483
Cohn, H. & Kulsrud, R. M. 1978, ApJ, 226, 1087
Dale, J. E., Davies, M. B., Church, R. P., & Freitag, M. 2009, MNRAS, 393, 1016
Danby, J. M. A. 1992, Fundamentals of celestial mechanics (Richmond: Willman-Bell, |c1992, 2nd ed.)
Dehnen, W. 2001, MNRAS, 324, 273
Do, T., Ghez, A. M., Morris, M. R., Lu, J. R., Matthews, K., Yelda, S., & Larkin, J. 2009, ApJ, 703, 1323
Eilon, E., Kupi, G., & Alexander, T. 2009, ApJ, 698, 641
Einstein, A. 1916, Annalen der Physik, 354, 769
Eisenhauer, F., Schödel, R., Genzel, R., Ott, T., Tecza, M., Abuter, R., Eckart, A., & Alexander, T. 2003, ApJ, 597, L121
Eisenhauer, F. et al. 2005, ApJ, 628, 246
Fasano, G. & Franceschini, A. 1987, MNRAS, 225, 155
Ferrarese, L. & Merritt, D. 2000, ApJ, 539, L9
Figer, D. F., Gilmore, D., Kim, S. S., Morris, M., Becklin, E. E., McLean, I. S., Gilbert, A. M., Graham, J. R., Larkin, J. E., Levenson, N. A., & Teplitz, H. I. 2003, ApJ, 599, 1139
Figer, D. F. et al. 2000, ApJ, 533, L49
Frank, J. & Rees, M. J. 1976, MNRAS, 176, 633
Freitag, M., Amaro-Seoane, P., & Kalogera, V. 2006, ApJ, 649, 91
Freitag, M. & Benz, W. 2002, A&A, 394, 345
Gebhardt, K. et al. 2000, ApJ, 539, L13
Genzel, R., Eisenhauer, F., & Gillessen, S. 2010, ArXiv:1006.0064
Genzel, R., Thatte, N., Krabbe, A., Kroker, H., & Tacconi-Garman, L. E. 1996, ApJ, 472, 153
Genzel, R. et al. 2003, ApJ, 594, 812
Ghez, A. M., Salim, S., Hornstein, S. D., Tanner, A., Lu, J. R., Morris, M., Becklin, E. E., & Duchêne, G. 2005, ApJ, 620, 744
Ghez, A. M., Salim, S., Weinberg, N. N., Lu, J. R., Do, T., Dunn, J. K., Matthews, K., Morris, M. R., Yelda, S., Becklin, E. E., Kremenek, T., Milosavljevic, M., & Naiman,

J. 2008, ApJ, 689, 1044
Ghez, A. M. et al. 2003, ApJ, 586, L127
Gillessen, S., Eisenhauer, F., Trippe, S., Alexander, T., Genzel, R., Martins, F., & Ott, T. 2009, ApJ, 692, 1075
Gould, A. & Quillen, A. C. 2003, ApJ, 592, 935
Griv, E. 2010, ApJ, 709, 597
Gualandris, A. & Merritt, D. 2009, ApJ, 705, 361
Gürkan, M. A. & Hopman, C. 2007, MNRAS, 379, 1083
Haller, J. W., Rieke, M. J., Rieke, G. H., Tamblyn, P., Close, L., & Melia, F. 1996, ApJ, 456, 194
Harfst, S., Gualandris, A., Merritt, D., & Mikkola, S. 2008, MNRAS, 389, 2
Heij, C., de Boer, P., Franses, P. H., Kloek, T., van Dijk, H. K., 2004, Econometric Methods with Applications in Business and Economics, Oxford University Press
Hills, J. G. 1988, Nature, 331, 687
—. 1991, AJ, 102, 704
Hopman, C. 2009, ApJ, 700, 1933
Hopman, C. & Alexander, T. 2005, ApJ, 629, 362
—. 2006a, ApJ, 645, 1152
—. 2006b, ApJ, 645, L133
Hopman, C., Freitag, M., & Larson, S. L. 2007, MNRAS, 378, 129
Hopman, C. & Madigan, A. 2010, ArXiv:1002.1220
Keshet, U., Hopman, C., & Alexander, T. 2009, ApJ, 698, L64
Kinoshita, H., Yoshida, H., & Nakai, H. 1991, Celestial Mechanics and Dynamical Astronomy, 50, 59
Kocsis, B. & Tremaine, S. 2010, ArXiv:1006.0001
Kustaanheimo, P. & Stiefel, E. 1965, J. Reine Angew. Math., 218, 204
Landau, L. D. & Lifshitz, E. M. 1969, Mechanics (Course of Theoretical Physics, Oxford: Pergamon Press, 1969, 2nd ed.)
Levin, Y. 2006, ApJ, 653, 1203
—. 2007, MNRAS, 374, 515
Lightman, A. P. & Shapiro, S. L. 1977, ApJ, 211, 244
Löckmann, U., Baumgardt, H., & Kroupa, P. 2008, ApJ, 683, L151
—. 2009, MNRAS, 398, 429
Madigan, A.-M., Levin, Y., & Hopman, C. 2009, ApJ, 697, L44
Madigan, A. 2010, ArXiv:1002.1277
Magorrian, J. & Tremaine, S. 1999, MNRAS, 309, 447
Martins, F., Gillessen, S., Eisenhauer, F., Genzel, R., Ott, T., & Trippe, S. 2008, ApJ, 672, L119
Merritt, D. 2010, ApJ, 718, 739
Merritt, D., Gualandris, A., & Mikkola, S. 2009, ApJ, 693, L35
Merritt, D. & Szell, A. 2006, ApJ, 648, 890
Merritt, D. & Vasiliev, E. 2010, ArXiv:1005.0040
Merritt, D., Alexander, T., Mikkola, S., & Will, C. 2011, ArXiv e-prints
Murphy, B. W., Cohn, H. N., & Durisen, R. H. 1991, ApJ, 370, 60
Peacock, J. A. 1983, MNRAS, 202, 615
Perets, H. B. & Gualandris, A. 2010, ApJ, 719, 220
Perets, H. B., Gualandris, A., Kupi, G., Merritt, D., & Alexander, T. 2009, ArXiv:0903.2912
Perets, H. B., Hopman, C., & Alexander, T. 2007, ApJ, 656, 709

Polyachenko, E. V., Polyachenko, V. L., & Shukhman, I. G. 2007, MNRAS, 379, 573
—. 2008, MNRAS, 386, 1966
Preto, M. & Amaro-Seoane, P. 2010, ApJ, 708, L42
Preto, M., Merritt, D., & Spurzem, R. 2004, ApJ, 613, L109
Rauch, K. P. & Holman, M. 1999, AJ, 117, 1087
Rauch, K. P. & Ingalls, B. 1998, MNRAS, 299, 1231
Rauch, K. P. & Tremaine, S. 1996, New Astronomy, 1, 149
Saha, P. & Tremaine, S. 1992, AJ, 104, 1633
Schödel, R., Eckart, A., Alexander, T., Merritt, D., Genzel, R., Sternberg, A., Meyer, L., Kul, F., Moultaka, J., Ott, T., & Straubmeier, C. 2007, A&A, 469, 125
Schödel, R., Merritt, D., & Eckart, A. 2009, A&A, 502, 91
Schödel, R., Ott, T., Genzel, R., Eckart, A., Mouawad, N., & Alexander, T. E. 2003, ApJ, 596, 1015
Sellgren, K., McGinn, M. T., Becklin, E. E., & Hall, D. N. 1990, ApJ, 359, 112
Shapiro, S. L. & Marchant, A. B. 1978, ApJ, 225, 603
Shen, J., Rich, R. M., Kormendy, J., Howard, C. D., De Propris, R., & Kunder, A. 2010, ApJ, 720, L72
Spitzer, L. 1987, Dynamical evolution of globular clusters, ed. Spitzer, L.
Syer, D. & Ulmer, A. 1999, MNRAS, 306, 35
Toonen, S., Hopman, C., & Freitag, M. 2009, MNRAS, 398, 1228
Touma, J. R., Tremaine, S., & Kazandjian, M. V. 2009, MNRAS, 394, 1085
Tremaine, S. 2005, ApJ, 625, 143
Trippe, S., Gillessen, S., Gerhard, O. E., Bartko, H., Fritz, T. K., Maness, H. L., Eisenhauer, F., Martins, F., Ott, T., Dodds-Eden, K., & Genzel, R. 2008, A&A, 492, 419
Weinberg, N. N., Milosavljević, M., & Ghez, A. M. 2005, ApJ, 622, 878
Wisdom, J. & Holman, M. 1991, AJ, 102, 1528
Yoshida, H. 1990, Physics Letters A, 150, 262
Zhu, Q., Kudritzki, R. P., Figer, D. F., Najarro, F., & Merritt, D. 2008, ApJ, 681, 1254

4

On the build-up of stars in the Galactic center

The central parsec of our galaxy is dense with stars of various ages. These populations may well derive from different formation processes and carry signatures of their origins. In this chapter we present a directly-observable statistic, h, that uses kinematical stellar data to highlight high-eccentricity populations. We perform N-body simulations to show how this statistic may be used on intermediate-aged stars, $\sim 100\,\mathrm{Myr}$, in the Galactic center to distinguish between two specific scenarios for their formation: episodic star formation in nuclear disks and tidal disruptions of binaries by the massive black hole. The most distinguishing feature between the two scenarios is a disparate $|h|$-signature at large radii, $p \gtrsim 7''$, where $\langle|h|\rangle = 0.12 \sim 0.48$ in the nuclear disk scenario and $\langle|h|\rangle = 0.1 \sim 0.14$ in the binary disruption scenario. This signature is already detectable with current observational techniques, and new data should soon distinguish between the two scenarios.

Ann-Marie Madigan et al. (2012)
To be submitted to The Astrophysical Journal

4.1 Introduction

The nuclear star cluster (NSC) in the central parsec of our galaxy is, in addition to the massive black hole (MBH) SgrA*, composed of stellar populations of various ages. The question arises as to where these stars originate — in situ, for example in a compact fragmenting gas disk, or outside this central region proceeding dynamical transportation inward? The answer to this question is relevant not only for piecing together the formation history of our Galactic NSC, but for understanding the mass accumulation in extragalactic NSCs in general, which is likely connected to the formation of MBHs at their centers (Hopkins & Quataert 2010a,b).

Due to the long stellar relaxation timescales in galactic nuclei containing MBHs, we expect their formation histories to be recorded in the morphology and kinematics of the cluster and its stellar populations. Extragalactic nuclei have been explored in this context using integral field spectroscopy and photometry, the results of which we briefly review below. In this chapter we focus on our own Galactic center (GC). Due to its proximity, it is possible to constrain formation scenarios using data from individual stellar phase space parameters, rather than collective position/velocity moments.

4.1.1 Nuclear star cluster formation

There are two basic scenarios for the build-up of stars in NSCs. The first scenario involves the merger of multiple star clusters following their inspiral towards the centers of galaxies via dynamical friction with background stars. Initial research focused on globular clusters (Tremaine et al. 1975), but recently Agarwal & Milosavljević (2011) have considered young massive star clusters formed in the inner part of the galaxy disk. The second scenario is in situ formation in nuclear stellar disks as a result of gas migration into the center of galaxies (Milosavljević 2004). The timescales for the inspiral of star clusters in the first scenario and gas migration in the second tell us that both scenarios are theoretically possible and the reality may well be a combination of both mechanisms, each varying in importance depending on factors such as galaxy type and redshift. However the ubiquity of nuclear stellar disks in the local neighborhood (Milky Way; M31; NGC 4244; M32) lends weight to the in situ scenario. Assuming we do not live in a special epoch, it suggests that such structures occur with regularity and are important contributors to the stellar mass in NSCs (e.g., Lauer et al. 1993; Tremaine 1995; Levin & Beloborodov 2003; Bender et al. 2005; Paumard et al. 2006; Chang et al. 2007; Lu et al. 2009; Bartko et al. 2010).

4.1.2 Observational constraints from extra-galactic nuclei

Observations of extragalactic NSCs frequently reveal, in addition to old, red spherical bulges, thin, blue disks of young stars $\lesssim 200\,\mathrm{Myr}$ in age (Seth et al.

2006, 2008; Seth 2010), which support an in situ formation scenario for NSCs. Seth et al. (2006) propose a model in which stars form episodically in compact nuclear disks. As observed NSC disks all have populations younger than 1 Gyr, there must exist a mechanism that disrupts the disk on such a timescale. The authors propose that the stellar disk loses angular momentum or heats vertically within this time to form an older spheroidal structure. As two-body relaxation is too slow a process, we require a more rapid dynamical mechanism. One possibility is torquing on the stellar disk from successive gas accretion (Seth et al. 2006) or due to an inner molecular ring (e.g., the circumnuclear disk in the GC; see Haas et al. 2011, and references therein), or, when formed, from the resulting new stellar disk (this chapter, Nayakshin et al. 2006; Löckmann & Baumgardt 2009; Löckmann et al. 2009). The duty cycle in this model, that is the period between star formation episodes, can be roughly estimated knowing the mass in the currently observed disk and the total mass in the NSC needed to build up over a Hubble time. Using nearby galactic NSCs to estimate this period yields a range between $\sim 0.1 - 1\,\mathrm{Gyr}$ (see discussion in Seth et al. 2006). Further motivation for this model is found in the results of Hartmann et al. (2011) who compare observations and dynamical models of NGC 4244 and M33 to results from N-body simulations of the formation and growth of NSCs through the merger of star clusters. The authors confirm that NSCs cannot form from purely stellar dynamical mergers and that gas dissipation is necessary for at least half of the stellar mass in extragalactic nuclei.

4.1.3 Evidence from the Galactic center

The Galactic NSC is unique among nuclei in that one can resolve individual stars of different ages. The spectroscopic detection is currently limited in magnitude to $m_{\mathrm{k}} \sim 15 - 16$. Early type stars in this magnitude range correspond to O-/WR-/B- dwarfs, giants and supergiants, and late type stars to K-giants and cool red supergiants (Bartko et al. 2010). While the late type stars may be too old to retain memory of their initial orbital conditions, the kinematics of the early type stars should, in some ways, reflect their original distribution. We briefly discuss their possible origins below; for a comprehensive review of the star formation history at the Galactic center see Genzel et al. (2010).

The ~ 200 early type stars within the central parsec can be categorized into two main groups. The first is a population of O- and Wolf-Rayet (WR) stars, $\sim 6 \pm 2\,\mathrm{Myr}$ old, with masses $\gtrsim 20 M_{\odot}$ (Paumard et al. 2006). The majority form a well-defined, warped disk with projected radii $0.8'' - 12''$, which rotates clockwise on the sky (Levin & Beloborodov 2003; Genzel et al. 2003; Lu et al. 2009; Bartko et al. 2009); we will refer to this population as the “O/WR disk”. The second population is an apparently isotropic (though a number may be part of the O/WR disk) distribution of B-stars, $m_{\mathrm{k}} > 15$. Those that lie within the central $0.8''$ are often collectively referred to as the “S-stars”; their kinematics reveal randomly-inclined and highly eccentric orbits (Ghez et al. 2005; Gillessen et al. 2009). Their proximity to the MBH, which prohibits star formation due to its immense tidal force (Morris 1993), combined with their young ages ($< 10\,\mathrm{Myr} \sim 100\,\mathrm{Myr}$) imply a “paradox of youth” (Ghez et al. 2003; Eisenhauer et al. 2005; Martins et al. 2008). Currently, it is not clear from the data whether or not the S-stars and the other B-stars in the central half-parsec form two distinct populations.

While the inspiral and subsequent tidal disruption of a young star cluster can produce a disk-like configuration similar to the O/WR disk (Gerhard 2001; Gürkan & Rasio 2005), the theory suffers from inconsistencies with respect to observations. A short dynamical friction timescale is imposed by the young ages of the stars, which it turn places implausible constraints on the initial location and mass of the cluster (Kim & Morris 2003)[1]. The necessity for an extremely dense cluster core invokes the presence of an intermediate-mass black hole (Hansen & Milosavljević 2003; Gürkan et al. 2004; Levin et al. 2005; Berukoff & Hansen 2006), but the formation of such an object in star clusters is still debated (e.g., Glebbeek et al. 2009) and there are stringent mass and orbital separation constraints from the MBH (Portegies Zwart et al. 2002; Yu & Tremaine 2003; Hansen & Milosavljević 2003; Kim et al. 2004; Gualandris & Merritt 2009). Finally, there is disparity of a factor of ~ 20 between the expected total X-ray luminosity of young, low-mass stars in the cluster and that from *Chandra* observations (Nayakshin & Sunyaev 2005). For these reasons, this scenario is disfavored for the recent build-up of stars in the GC, though it may well be a relevant or even dominant component in some extragalactic nuclei.

The leading theory for the origin of the O/WR disk is the in situ formation from fragmentation of in-falling or colliding gas clumps at the GC (Morris 1993; Sanders 1998; Levin & Beloborodov 2003; Nayakshin & Cuadra 2005; Levin 2007; Wardle & Yusef-Zadeh 2008, 2011). The density profile, radial extent and sharp inner edge of the disk (Lu et al. 2009; Bartko et al. 2010) is reflected in simulations (Bonnell & Rice 2008; Hobbs & Nayakshin 2009). The low levels of X-ray luminosity in the SgrA* field (Nayakshin & Sunyaev 2005) can be explained by a top-heavy initial-mass function, a condition that has so far been fulfilled observationally (Maness et al. 2007; Bartko et al. 2010) and in simulations (Alexander et al. 2008) (but see Löckmann et al. 2010). Additional support comes from recent analysis of *Fermi*-LAT data, which reveal two large gamma-ray bubbles symmetric about the Galactic plane, extending 50° above and below the GC (Su et al. 2010). The authors propose that they were born in a large episode of energy injection in the GC – an accretion event on to SgrA*, or a nuclear starburst in the last $\sim 10\,\mathrm{Myr}$, the latter being coincident with the formation of the O/WR disk, as explored by Zubovas et al. (2011). Assuming, as evidence suggests, the O/WR disk formed in situ around the MBH, it is not unreasonable to expect that previous epochs of gas migration and nuclear stellar disk formation took place in the GC.

---

[1] A problem exacerbated if the core in the GC exists for the bulk of the mass in stars (Antonini & Merritt 2011).

The origin of the B-stars however, is much less clear than that of the O/WR disk. Their ages are ambiguous, and range from a spectroscopically confirmed $< 10\,\mathrm{Myr}$ for the S-star S2/S0-2 (Ghez et al. 2003; Eisenhauer et al. 2005; Martins et al. 2008), to an upper-limit of $\sim 100\,\mathrm{Myr}$ on the main sequence of the lower-mass B-stars. This upper limit does not preclude the B-stars having formed with the O/WR stars, but they may well be from an older population or even form a continuous distribution in age. To discuss various possible formation mechanisms, we must first distinguish between studies on the S-stars and those involving the outermost B-stars.

One of the leading theories for the formation of the S-stars is the tidal capture by SgrA* of close B-star binaries by Hills mechanism (Hills 1988, 1991; Gould & Quillen 2003). The most plausible theory for populating these infalling binaries is dynamical relaxation by massive perturbers such as giant molecular clouds (Perets et al. 2007) within the central $10 - 100\,\mathrm{pc}$, although viable alternatives certainly exist (e.g., Madigan et al. 2009; Löckmann et al. 2009). The challenge in the binary disruption scenario is that the S-stars are captured on orbits of very high eccentricity and yet we observe them to have a near-thermal distribution (Gillessen et al. 2009). Two studies have investigated this issue: direct N-body simulations but without general relativistic precession by Perets et al. (2009), and our own study (Madigan et al. 2011) utilizing a Monte Carlo "ARMA" code with general relativistic precession. Perets et al. (2009) find that resonant relaxation is sufficiently rapid to randomize the orbital eccentricities from high-eccentricity values to those observed within $\sim 20\,\mathrm{Myr}$, while we find that GR precession undermines this process close to the MBH and leaves the stars with too high eccentricities as compared with observations. Further study is necessary to see if the newly identified "Schwarzschild barrier" will resolve this issue (Merritt et al. 2011).

It is attractive to assume that the B-stars outside the central arcsecond have also formed via Hills mechanism, as proposed by Perets & Gualandris (2010). However in this case, as the authors point out, the high eccentricity issue is acute, since neither two-body nor resonant relaxation will be able to significantly change the orbital eccentricities of the B-stars at large radii within the range of their lifetimes. This sets up a prediction which observational data from this population will be able to verify or refute.

In this chapter we 1) point out that there is another mechanism for dynamically relaxing the eccentricity distribution – the formation and presence of the O/WR stellar disk, and 2) devise a statistic which is particularly sensitive to identifying, or ruling out, stellar distributions with high orbital eccentricities. We investigate two scenarios – the massive perturber plus binary disruption scenario (Perets et al. 2007), and one based on the model of Seth et al. (2006), wherein we propose that the B-stars formed in a nuclear stellar disk $\sim 100\,\mathrm{Myr}$ ago – and examine the resulting orbital parameters of the B-stars after $6\,\mathrm{Myr}$ of interaction with the O/WR disk. The chapter is organized as follows. In Section 4.2 we discuss the two formation scenarios in detail and describe our suite of N-body simulations. We show that the new statistic can robustly differentiate between the two scenarios for the origin of the B-stars in the GC in Section 4.3. We summarize our study in Section 4.4.

4.2 Numerical methods and scenarios

Here we contrast two main formation scenarios for the intermediate-aged population of B-stars in the Galactic center. We perform N-body simulations to investigate whether their original orbital eccentricities will be preserved over $6\,\mathrm{Myr}$, having been subjected to torquing from the O/WR disk. We use our special-purpose N-body integrator, which is described in detail in Madigan et al. (2011). Our integrator is based on a mixed-variable symplectic algorithm (Wisdom & Holman 1991; Kinoshita et al. 1991; Saha & Tremaine 1992) and designed to accurately integrate the equation of motion of a particle in a near-Keplerian potential with minimum spurious precession. In the simulations for this study, we use direct N-body particles which move in Kepler elements along ellipses under the influence of the central object, and calculate perturbations to their orbits in Cartesian co-ordinates from surrounding N-body particles (Danby 1992). We define semi major axis, a, and eccentricity, e, of stellar orbits with respect to a stationary MBH in our simulations,

$$a = -\frac{GM_\bullet}{2E}, \tag{4.1}$$

and

$$e = \left(1 - \frac{J^2}{GM_\bullet a}\right)^{1/2}, \tag{4.2}$$

where $M_\bullet$ is the mass of the MBH, and J and E are the specific orbital angular momentum and energy of a star. The periapse of the orbits of these stellar particles precess with retrograde motion due to Newtonian mass precession from the additional smooth potential from surrounding cluster of stars. The time to precess by 2π radians is

$$t_{\mathrm{prec}}^{\mathrm{cl}} = \pi(2-\alpha)\frac{M_\bullet}{N(<a)m}P(a)f(e,\alpha), \tag{4.3}$$

where $N(<a)$ is the number of stars within a given a, m is the mass of a single star, $f(e,\alpha)$ is a function which depends on the eccentricity of the orbit and the power-law index α of the surrounding cluster of stars, and $P(a) = 2\pi(a^3/GM_\bullet)^{1/2}$ is the orbital period of a star with semi-major axis a. We include the first post-Newtonian general relativistic effect, that is prograde apisidal precession with a timescale,

$$t_{\mathrm{prec}}^{\mathrm{GR}} = \frac{1}{3}(1-e^2)\frac{ac^2}{GM_\bullet}P(a). \tag{4.4}$$

Our simulations have four main components chosen to represent the Galactic center $\sim 6\,\mathrm{Myr}$ in the past. The first is a MBH of mass $M_\bullet = 4 \times 10^6 M_\odot$ (Ghez et al. 2008). Second is a smooth stellar cusp with power-law density profile $n(r) \propto r^{-\alpha}$, $\alpha \in [0.5, 1.75]$, normalized with a mass of $1.5 \times 10^6 M_\odot$ within 1 pc (Schödel et al. 2007; Trippe et al. 2008; Schödel et al. 2009). We choose to use a smooth potential for the cusp in our simulations as this greatly decreases the required computation time. Traditional two-body gravitational relaxation has no impact on the stars since its characteristic timescale is greater than $5\,\mathrm{Gyr}$ at all radii (see figure 3 from Merritt 2010). Resonant relaxation (Rauch & Tremaine 1996) occurs on a shorter timescale, and we model it explicitly to use in our initial conditions (see Figure 4.1) using the ARMA code described in detail in Madigan et al. (2011). The numerical simulations of Löckmann & Baumgardt (2009) show that even with resonant relaxation, the cusp contributes relatively little to relaxation of stellar disks as compared with disk stars themselves, and Madigan et al. (2009) find that in the case of coherently eccentric disks, significant angular momentum changes can occur on timescales less than $1\,\mathrm{Myr}$. Hence we are confident that choosing a smooth stellar cusp over a grainy one will not greatly affect our results.

The third component in our simulations is the most dynamically important structure: an eccentric stellar disk ($e = 0.3, 0.6$) with surface density profile $\Sigma(a) \propto a^{-2}$, made up of $N_{\rm disk} = 100$ equal-mass N-body particles with total mass $M_{\rm disk} = 10^4 M_\odot$ and semi-major axes $0.03\ \mathrm{pc} \leq a \leq 0.5\ \mathrm{pc}$. This disk represents the O/WR disk. In our basic model, the O/WR disk is formed instantaneously, i.e., fully formed at $t = 0$, with an inclination opening angle of 1°. However, we also run a number of simulations where we model its formation using a “switch-on” multiplicative function for the disk mass, such that the mass of a single star is

$$m(t) = \frac{M_{\rm disk}}{N_{\rm disk}} \tanh\left(\frac{t - t_0}{\tau}\right), \tag{4.5}$$

where t_0 is -1 years (so that the O/WR disk has mass at t = 0) and the growth timescale τ is 1×10^5 years (Bonnell & Rice 2008). Secular gravitational interactions with the O/WR disk will affect the angular momenta of the B-stars. We anticipate the greatest eccentricity change for stars at similar radii to the inner edge of the disk – the torques are much greater at these radii, as

$$\tau \sim \left(\frac{GM_{\rm disk} e_{\rm disk} e}{a}\right) \delta\phi, \tag{4.6}$$

where τ is specific torque on a stellar orbit, $e_{\rm disk}$ is a typical eccentricity of a star in the disk and $\delta\phi$ is the angle between them.

The fourth component of our simulations, the B-stars, depends on the scenario we are simulating; we describe them both here.

Dissolved Disk (DD) Scenario: In this scenario, the B-stars form in-situ around the MBH in a nuclear stellar disk during an earlier episode ($\sim 100\,\mathrm{Myr}$) of gas infall and fragmentation: we call this the *dissolved disk* scenario as the disk structure should have 'puffed up' due, mainly, to vector resonant relaxation. The disk should not be entirely dissipated within $100\,\mathrm{Myr}$ however – two-body relaxation acts on much longer timescales and vector resonant relaxation is suppressed in high-frequency, short-wavelength modes (Kocsis & Tremaine 2010).

We simulate the B-stars in this scenario as a stellar disk with semi-major axes between $0.03\ \mathrm{pc} \leq a \leq 0.7\ \mathrm{pc}$, consisting of 100 N-body particles with equal masses of $100M_{\odot}$. The density profile is $\Sigma(a) \propto a^{-2}$ while the initial eccentricities and opening angle of the disk vary (the basic model draws from a thermal eccentricity distribution), and the inclination with respect to the O/WR is systematically explored. These initial conditions are crude out of necessity – we have a poor understanding of the true initial parameters – but nevertheless we are able to capture the essential dynamics of the interaction with the O/WR disk.

Binary disruption (BD) Scenario: This formation scenario invokes enhanced relaxation from massive perturbers (Perets et al. 2007) which propel binaries from outside the central parsec onto near-radial orbits where they can be disrupted by the MBH near periapsis via Hills' mechanism. Thus, in this scenario the B-stars are members of binaries that have been left bound to the MBH as their partners were ejected into the halo at high velocities. They have a spatially isotropic distribution, represented by 100 N-body particles with masses $100M_{\odot}$ distributed between $0.03\ \mathrm{pc} \leq a \leq 0.7\ \mathrm{pc}$. They are initialized with a density profile $\Sigma(a) \propto a^{-2}$ and begin their lives in the Galactic center on Kepler orbits with very high eccentricities as $e = 1 - r_t/a \sim (m_{\mathrm{bin}}/M_{\bullet})^{1/3}$ (see, e.g., Pfahl 2005), where $r_t = a_{\mathrm{bin}}(M_{\bullet}/m_{\mathrm{bin}})^{1/3}$ is the tidal radius of the MBH, and m_{bin} and a_{bin} are the mass and semi-major axis of the binary.

We use our ARMA code (see Madigan et al. 2011, for details) to simulate the evolution of orbital eccentricities for B-stars in the BD scenario without the dynamical influence of the O/WR disk but including two-body and resonant relaxation. In doing so, we confirm the result by Perets & Gualandris (2010) that stellar orbits remain at very high eccentricities outside $\sim 0.1\,\mathrm{pc}$. We find higher mean eccentricity values at all radii however, for both steep ($\alpha = 1.75$) and shallow ($\alpha = 0.5$) cusp profiles; see Figure 4.1 in which we plot mean orbital eccentricities as a function of semi-major axis at 60 and $100\,\mathrm{Myr}$. We simulate both a *burst* scenario in which all B-stars begin at $t = 0$, and a *continuous* scenario in which they are randomly initialized between $t = 0$ and $t = t_{\mathrm{max}}$; the latter best reflects binary disruptions due to massive perturbers but the former can be directly compared with the simulations of Perets & Gualandris (2010). As the authors use full N-body simulations, they do not include the entire stellar cusp and hence precession rates for stars are lower than in our simulations, contributing to a higher resonant relaxation rate and hence larger eccentricity changes. We use a fit of the resulting eccentricity distribution after $100\,\mathrm{Myr}$ in the *continuous* case as our initial conditions for our BD scenario.

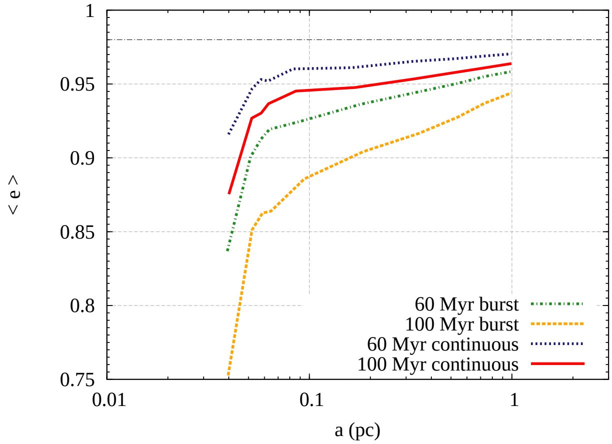

Figure 4.1 – Mean B-star orbital eccentricities as a function of semi-major axis in the BD scenario. Stars begin with initial eccentricity $e = 0.98$ and evolve due to resonant and non-resonant relaxation over 60 and $100\,\mathrm{Myr}$. In the *burst* scenario, stars are initialized at $t = 0$; in the *continuous* scenario, they are initialized randomly between $t = 0, t_{\mathrm{max}}$. For this plot we use our ARMA code (Madigan et al. 2011) with $M(< 1\,\mathrm{pc}) = 1.5 \times 10^6 M_\odot$ and $\alpha = 1.75$.

Our simulation runs are organized to explore a wide range of parameters relevant for the GC; see Table 4.1 for specifics of each run. An important variation in the models is the stellar cusp index of which we choose two values – a steep stellar cusp $\alpha = 1.75$, and a shallow stellar cusp $\alpha = 0.5$ – the latter motivated by recent observations of the old stellar population in the GC (Buchholz et al. 2009; Do et al. 2009; Bartko et al. 2010; Yusef-Zadeh et al. 2011). This variation reveals itself in the precession rate of stars at different radii, and hence the persistence of stellar torques. Another difference is the mean eccentricity of the B-stars and the O/WR disk stars, which will affect the results through the strength of the torques between the two groups.

In addition, we run simulations with both coherently eccentric (or lopsided) O/WR disks where the eccentricity vectors of the stellar orbits overlap (Bonnell & Rice 2008; Hopkins & Quataert 2010a,b), and non-coherent ones. The *DD* simulations vary in the opening angle of the B-star disk and the inclination angle between the two disks. The relative orientation of O/WR disk is important as B-star orbits like to orient themselves with this new disk.

A more realistic stellar mass function for the O/WR and B-star populations should not have an impact on our results; due to the equivalence principle, the stars will respond to the gravitational potential in the same way, regardless of their mass. A reduction in the average mass in stars however, with a corresponding increase in their number, will reduce the coherence of the stellar torques – in this case the B-star population will retain memory of their initial conditions over an even longer timescale.

Table 4.1 – Model parameters

Model[1]	$\langle e\rangle$[2]	α[3]	$\langle e\rangle_{\mathrm{O/WR}}$[4]	sw[5]	θ[6]	$\langle i\rangle$[7]	$\langle\lvert h\rvert\rangle$[8]
BD_1	0.97	0.5	0.6 c	0	-	-	0.1
BD_2	0.97	0.5	0.6 c	1	-	-	0.1
BD_3	0.97	0.5	0.6	0	-	-	0.11
BD_4	0.97	0.5	0.3 c	0	-	-	0.1
BD_5	0.93	1.75	0.6 c	0	-	-	0.12
BD_6	0.93	1.75	0.3 c	0	-	-	0.14
DD_1	0.6	0.5	0.6 c	0	40	80	0.15
DD_2	0.6	0.5	0.6 c	0	40	25	0.28
DD_3	0.6	0.5	0.6 c	0	40	121	0.48
DD_4	0.6	0.5	0.6 c	0	40	163	0.18
DD_5	0.6	0.5	0.6	0	40	80	0.12
DD_6	0.3	0.5	0.6 c	0	40	80	0.43
DD_7	0.6	1.75	0.6 c	0	40	80	0.23
DD_8	0.6	0.5	0.6 c	0	60	80	0.29
DD_9	0.6	0.5	0.6 c	1	40	80	0.14
DD_{10}	0.6	0.5	0.3 c	0	40	80	0.19

Notes

[1] BD: binary disruption. DD: dissolved disk.

[2] Mean initial eccentricity of B-stars across all radii.

[3] Index of power-law density cusp profile.

[4] Mean initial eccentricity of O/WR stars. c: coherent disk.

[5] Switch-on function on/off (1/0).

[6] Initial opening angle B-star disk in arcdeg.

[7] Mean initial inclination of B-star disk with respect to O/WR disk in arcdeg.

[8] Mean absolute value of h for B-stars with $p > 7''$ at end of simulation.

4.3 Results

4.3.1 Evolution of orbital eccentricities

We run the simulations for $6\,\mathrm{Myr}$ to follow the orbital vector and scalar angular momentum change in the B-stars in response to the stellar disk. The B-stars with small semi major axes not only experience a greater torque, $\tau \propto 1/a$, but have lower angular momentum, J, and hence the percentage change in angular momentum is high. This brings about a rapid change in their eccentricities. In contrast, B-stars with large semi-major axes experience smaller torques, less percentage change in J and retain memory of their initial orbital eccentricities. Hence these large a stars can constrain their formation scenario. This is as Perets & Gualandris (2010) found for resonant relaxation, but the change in eccentricities of low-radii B-stars over $6\,\mathrm{Myr}$ under the persistent torques of the O/WR disk proves to be more rapid than resonant relaxation over $100\,\mathrm{Myr}$. We show this effect in Figure 4.2, plotting the eccentricity, e, of B-star orbits as a function of semi major axis, a, for different times during the simulation. The BD scenario produces the most dramatic signature as stars with large semi

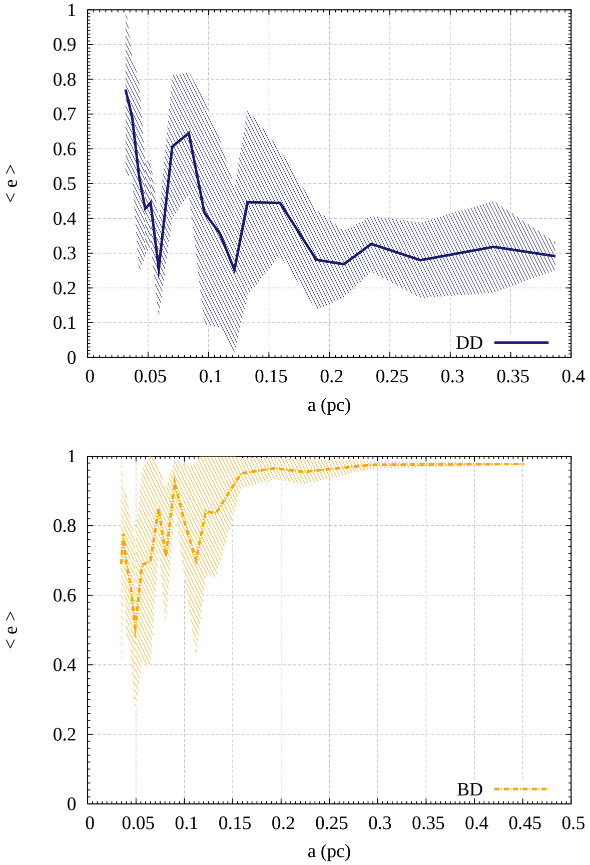

Figure 4.2 – Mean eccentricity and one standard deviation of B-stars after $6\,\mathrm{Myr}$ of evolution in the DD_6 scenario (top) and BD_1 scenario (bottom) as a function of semi major axis a. Stars at large a do not move far from their original eccentricity values. In particular, all stars in the BD scenario with $a > 0.26$ remain almost fixed with $e > 0.96$.

major axes retain their high orbital eccentricities. In the DD scenario, the B-stars with large semi major axes have similar eccentricities as their initial values and so are highly sensitive to their initial conditions.

For the B-stars outside of the central arcsecond, only a very small portion of their orbits has been mapped out, sufficient to determine their "instantaneous" proper motion but insufficient to determine their eccentricities and other orbital parameters. In the next subsection we develop a statistic which uses the star's sky position and proper motion velocities and is particularly sensitive in identifying distributions with high orbital eccentricity.

4.3.2 The high-eccentricity statistic

The basic idea for identifying stars with high eccentricities is straightforward: the radial orbit in three spacial dimensions also appears as a radial orbit in projection on the sky. This was noted by Genzel et al. (2003) and revisited by Paumard et al. (2006) and Bartko et al. (2009). These authors have utilized the j versus p diagram, where j is the normalized angular momentum along the line-of-sight (z-axis),

$$\begin{aligned} j &= \frac{j_z}{j_{\mathrm{z(max)}}} \\ &= \frac{xv_y - yv_x}{pv_p}. \end{aligned} \tag{4.7}$$

Here v_x, v_y are the right ascension and declination velocities of a star at (x, y) on the sky,

$$v_p = (v_x^2 + v_y^2)^{1/2} \tag{4.8}$$

is the projected velocity (i.e., proper motion), and

$$p = (x^2 + y^2)^{1/2} \tag{4.9}$$

is the projected radius from the MBH. The quantity j is $\sim 1, \sim 0, \sim -1$ depending on whether the stellar orbit projected on the sky is mainly clockwise (CW) tangential, radial, or counterclockwise (CCW) tangential with respect to the projected radius. To compare different stellar populations, Genzel et al. (2003) and Paumard et al. (2006) define three j ranges: CW tangential ($j \geq 0.6$), CCW tangential ($j \leq -0.6$) and radial ($-0.3 \geq j \leq 0.3$).

Here we show that the quantity j is not the one that is most sensitive to the high-e stellar distributions. This is because stars on radial orbits spend the majority of their orbital period near apoapsis, and hence can have low v_p with respect to the circular velocity at their projected radii p; this increases their value of j and imparts a more tangential orbit in projection. Instead, we propose to use the high-eccentricity statistic, h: j_z normalized to the maximum angular momentum at that radius (i.e. taking circular velocity at p):

$$\begin{aligned} h &= \frac{j_z}{J_p} \\ &= \frac{xv_y - yv_x}{\sqrt{GM_\bullet p}}, \end{aligned} \tag{4.10}$$

where we have used the Keplerian circular velocity such that $v_{\mathrm{circ}}(p) = (GM_\bullet/p)^{1/2}$ (i.e., we do not include the stellar mass within radius p).

We contrast the j and h versus p diagrams for both scenarios in Figure 4.3. To directly compare with observations, we work in units of arcsecond using

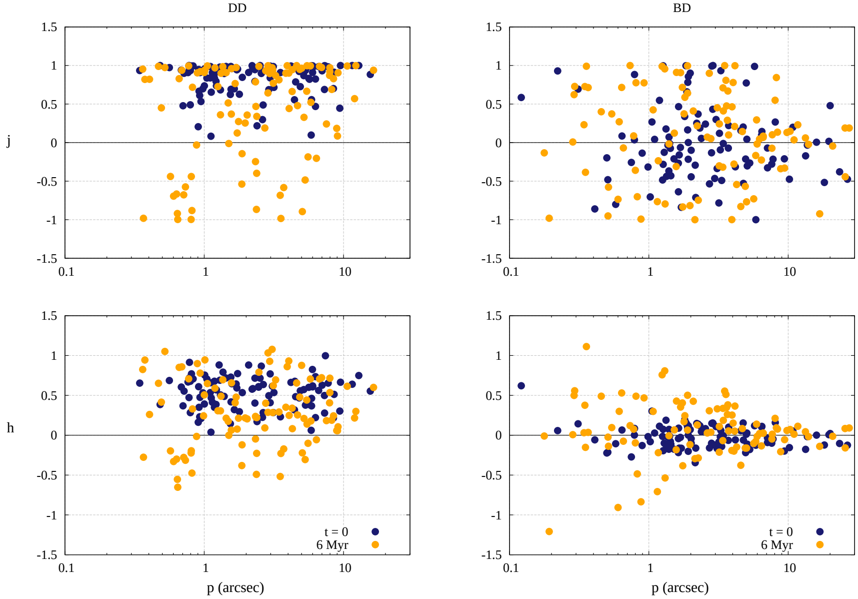

Figure 4.3 – (Top) Distribution of projected, normalized orbital angular momentum on the sky, j, for stars in the DD_6 scenario (left) and BD_1 scenario (right) at $t = 0, 6\,\mathrm{Myr}$. In plotting the parameter j we lose evidence of high eccentricity orbits as stars on near-radial orbits spend most of their orbital period near apoapsis and their v_p value will be lower than the circular velocity at their projected radius p. (Bottom) Distribution of projected orbital angular momentum on the sky normalized to the maximum angular momentum at that projected radius p, for stars in the DD_6 scenario (left) and BD_1 scenario (right) at $t = 0, 6\,\mathrm{Myr}$. This new statistic, h, illuminates high eccentricity orbits by focusing them at zero.

the conversion $1'' = 0.0388\,\mathrm{pc}$ which corresponds to a distance to SgrA* of 8.0 kpc (Eisenhauer et al. 2003; Ghez et al. 2008; Gillessen et al. 2009). The advantage of the h-parameter is not obvious in the DD scenario as there are few very-high eccentricity orbits. However, in the BD scenario, the B-stars at large radii retain their high eccentricities over the $6\,\mathrm{Myr}$ simulation, and their h values are centered about zero in contrast with the j-parameter.

We plot the mean value of $|h|$ as a function of projected radius p at the beginning of the simulation and after $6\,\mathrm{Myr}$ in Figure 4.4. The most distinguishing feature between the two scenarios is the disparate $|h|$-signature at large radii, $p > 7''$, where $\langle|h|\rangle \sim 0.12 - 0.48$ in the DD scenario and $\langle|h|\rangle \sim 0.1 - 0.14$ in the BD scenario. These results are dependent on binning but the qualitative trend is not, and they can be directly compared to observations using a χ^2 analysis which can take observational errors into account. The mean values of $|h|$ for stars with large projected radii, $p > 7''$, are listed in Table 4.1.

Simulations BD_{1-4} (shallow cusp, $\alpha = 0.5$) produce B-stars with higher eccentricities, and hence lower mean $|h|$ values, at large radii in comparison

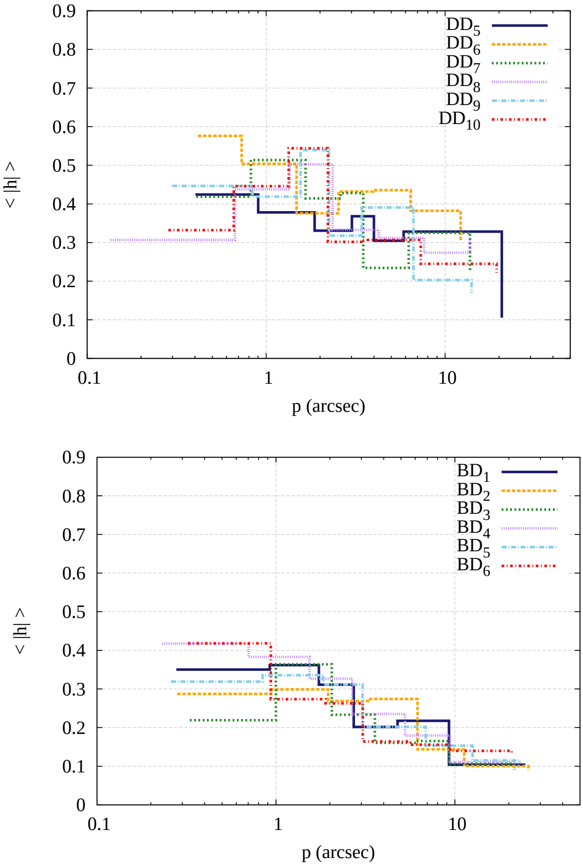

Figure 4.4 – Mean absolute h values as a function of projected distance, p, for several variations of the DD scenario (top) and BD scenario (bottom). The DD results are dependent on disk orientation angle with respect to the line of sight. All variants of the BD scenario produce low $|h|$ values at large projected radii, the most distinguishable feature between the two scenarios.

with simulations BD_{5-6} (steep cusp, $\alpha = 1.75$); the stellar orbits of the latter, at large radii, precess relatively slowly and secular changes in J are more efficient as torques can act on the stellar orbits over a longer time. The BD_3 simulation with a non-coherent O/WR disk has lower $|h|$ values at low radii than the others. This is expected as the stellar torques at the inner edge of the disk will not be aligned and hence be weaker. This is also seen in DD_5 in which the O/WR disk is non-coherent. The DD_6 simulation, in which the B-stars are initialized in an $e = 0.3$ disk, and DD_8 with a larger opening angle in the B-star disk, produce higher $|h|$ values for a similar reason. The simulations employing the "switch-on" function show no differences with respect to the basic models. The inclination angle between the two disks plays an important role in deter-

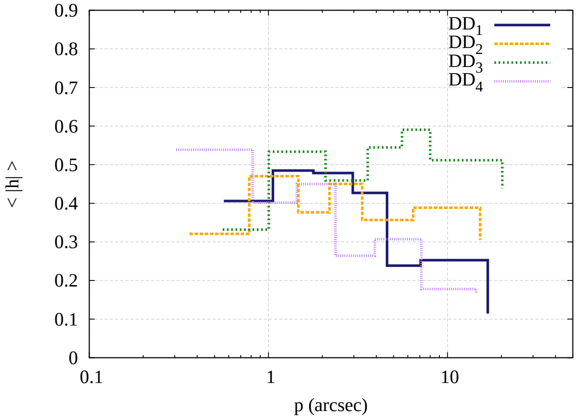

Figure 4.5 – Mean absolute h values as a function of projected distance, p, for four variations of the DD scenario which vary only in inclination angle between the O/WR disk and B-star disk. The DD results are dependent on disk orientation angle with respect to the line of sight.

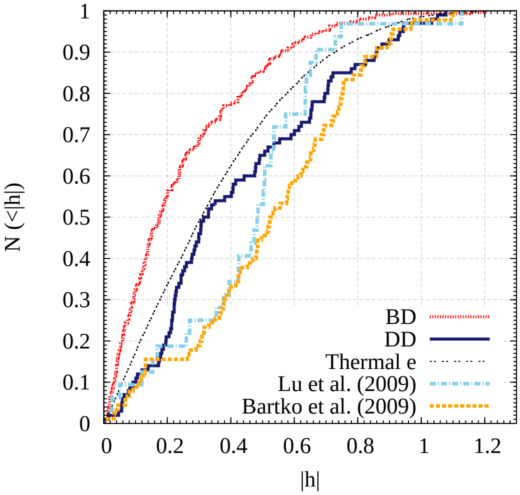

Figure 4.6 – Cumulative $|h|$ plots for the DD_6 scenario and BD_1 scenario with corresponding values from a thermal eccentricity distribution as a comparison. Also plotted are the values for the O/WR disk (Lu et al. 2009; Bartko et al. 2010). The DD results, though dependent on orientation of the B-star disk plane, are qualitatively similar regardless of viewing angle.

mining the resulting $|h|$ values and we plot DD_{1-4} in Figure 4.5. In $DD_{1,2}$, where the initial mean inclination angle between the two disks is $\langle i \rangle < 90°$, the B-star angular momentum vectors tend to overlap with those of the O/WR disk by the end of the simulation. In $DD_{3,4}$, where the initial mean inclination angle between the two disks is $90^\circ < \langle i \rangle < 180^\circ$, the two disks are still distinguishable from each other after $6\,\mathrm{Myr}$. In all DD cases, a substantial fraction of the B-stars are in an isotropic distribution at the end of the simulation.

We plot the cumulative $|h|$ values in Figure 4.6 for representative examples of each scenario, DD_6 and BD_1, with a thermal distribution of eccentricities for comparison. The BD scenario produces more low $|h|$ orbits than the DD scenario. If we have the observed distribution for B-stars, we can perform a two-dimensional Kolmogorov-Smirnov (2DKS) test, a nonparametric test which checks whether two data samples come from different distributions (see e.g., Peacock 1983), against the simulated cumulative distributions. We also present the cumulative $|h|$ distributions for the O/WR stars from data in Bartko et al. (2009) and Lu et al. (2009). Though the data sample given in these two papers overlap, they are not identical and differences are observed; the stars in the Lu et al. (2009) data sample have lower $|h|$ values and hence are more eccentric. The observational data include errors which are normally distributed, which tends to artificially "isotropize" their stellar distribution. This issue will have to be addressed when considering real data from B-stars.

4.4 Summary

In this chapter we compare two formation scenarios of the B-stars in the GC; the dissolved disk scenario based on the model proposed by Seth et al. (2006), and the binary disruption scenario due to enhanced stellar relaxation from massive perturbers by Perets et al. (2007). We specifically investigate the change in the B-star orbital parameters after dynamical gravitational interaction with the O/WR disk over $6\,\mathrm{Myr}$, concentrating on those at large radii where torques from stellar orbits are weakest. We formulate a new, directly-observable statistic, h, which uses the position of stars on the sky (x, y) and their proper motion (v_x, v_y), and show that it is particularly sensitive to high-eccentricity orbits.

The results from our N-body simulations show that we can constrain the formation scenario, in particular the high-eccentricity signature of the binary disruption model. Non-parametric testing between the observed cumulative distribution function of h and those simulated here may be used to compare the two. Distinguishing between the scenarios based on the h-statistic is already possible with current observational techniques, and new data should soon exclude one or both formation mechanisms.

If the dissolved disk scenario best fits the observations, this will inform us about the build-up of stellar mass in the GC, and the h values of the stars at large radii will help constrain the initial orbital parameters of the stars in the disk. An additional feature to look for in this case is the outer cut-off in radius of the B-stars. If the binary disruption scenario best fits the data, the formation mechanism of the S-stars and the rest of the B-stars in the GC will be united.

Acknowledgments A.-M.M. is supported by a TopTalent fellowship from the Netherlands Organisation for Scientific Research (NWO), and thanks Monash University for their hospitality during her visit. Y.L. is supported by a VIDI fellowship from NWO. We thank Clovis Hopman for useful discussions, and for encouraging an economy of words in this chapter.

4.A Statistical constraints on eccentricity from the h-statistic

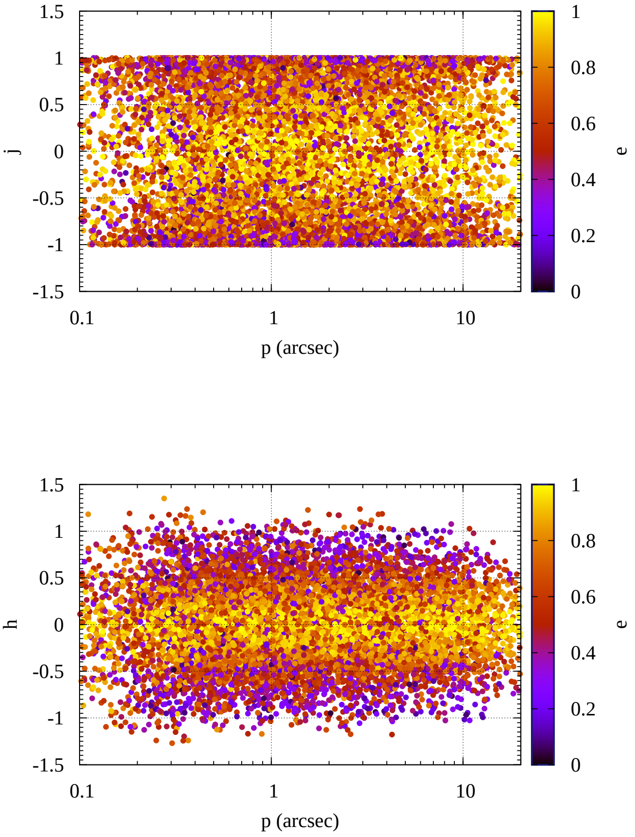

Figure 4.7 – j (top) and h (bottom) values of stars as a function of projected radius, p, color-coded according to orbital eccentricity, e. These plots illustrate the sensitivity of the h-parameter to high-eccentricity orbits and demonstrate how it can be used to constrain the dynamical origin of stars in the GC.

For a given eccentricity distribution we can plot the corresponding j and h values and see how well they constrain the original eccentricity distribution. We do so here for a thermal distribution of eccentricities, initializing one thousand B-star orbits with cumulative distribution function $f(e) = e^2$, and calculating their j and h values. Figure 4.7 shows both the j and h planes populated by stars colored according to their orbital eccentricities. These plots visualize the fidelity with which the h parameter, in contrast to the j parameter, differentiates between tangential vs radial orbits; near-radial orbits are confined to

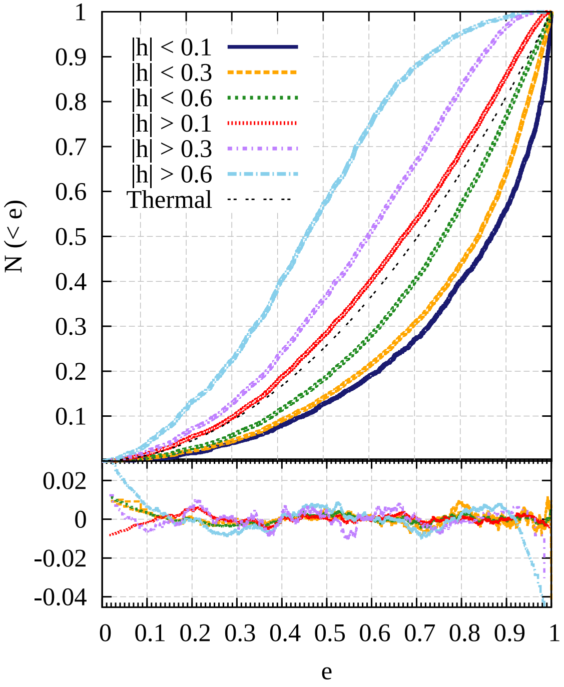

Figure 4.8 – Cumulative plots of stellar eccentricity for different slices of $|h|$. The original distribution in this case has a thermal eccentricity profile, $f(e) = e^2$, also plotted for comparison. Below are plotted the residuals from the simulated cumulative distribution functions and the fits to the function in Equation 4.11.

low $|h|$ values.

We plot the cumulative distribution of orbital eccentricities in specific $|h|$ bins in Figure 4.8. Our goal is to place statistical limits on the eccentricities of stars using the h plot. For example, 50% of stars with $|h| < 0.1(0.3)$ have an eccentricity $e > 0.87(0.84)$, while 90% of stars with $|h| > 0.6$ have an eccentricity $e < 0.73$. These statistics are dependent on the initial eccentricity distribution. As neither the DD nor the BD scenario produce a thermal eccentricity distribution after $6\,\mathrm{Myr}$, we cannot directly use these limits, but these plots illustrate the usefulness of the h parameter and can used to constrain older stellar populations which are expected to be isotropized.

We fit the cumulative e distributions shown in Figure 4.8 with the following

Table 4.2 – Fits of e-distributions in Figure 4.8 to Equation (4.11)

$\lvert h\rvert$[1]	μ	σ^2	β	γ	δ	ϵ
< 0.1	0.96	0.17	-1.06	-1.22	1.20	1.10
< 0.3	1.06	0.01	4.22	0.15	-0.16	-4.09
< 0.6	1.66	0.16	5.43	0.09	-0.10	-5.26
> 0.1	0.34	0.13	5.75	0.29	-0.45	-6.52
> 0.3	0.40	0.13	6.95	1.35	-1.48	-7.51
> 0.6	0.51	0.05	-2.80	-0.54	0.51	3.15

Notes

[1] Absolute value of h corresponding to distributions in Figure 4.8.

formula

$$\begin{aligned} f(x) = {} & \frac{1}{2}\left[1 + \mathrm{erf}\left(\frac{x-\mu}{\sqrt{2\sigma^2}}\right)\right] \\ & + \beta x + \gamma\sqrt{1-x^2} + \delta\cos(x) + \epsilon\sin(x), \end{aligned} \tag{4.11}$$

where μ and σ^2 are the mean and variance of a cumulative Gaussian distribution, β, γ, δ and ϵ are coefficients and $x = e$. The trigonometric terms are chosen ad-hoc; they are necessary to fit the extreme distributions $|h| > 0.6$, $|h| < 0.1$. The fitted values for each line in Figure 4.8 are listed in Table 4.2; the residuals from subtracting the functions from the distributions are plotted in the lower panel.

References

Agarwal, M. & Milosavljević, M. 2011, ApJ, 729, 35

Alexander, R. D., Armitage, P. J., Cuadra, J., & Begelman, M. C. 2008, ApJ, 674, 927

Antonini, F. & Merritt, D. 2011, ArXiv e-prints

Bartko, H., Martins, F., Fritz, T. K., Genzel, R., Levin, Y., Perets, H. B., Paumard, T., Nayakshin, S., Gerhard, O., Alexander, T., Dodds-Eden, K., Eisenhauer, F., Gillessen, S., Mascetti, L., Ott, T., Perrin, G., Pfuhl, O., Reid, M. J., Rouan, D., Sternberg, A., & Trippe, S. 2009, ApJ, 697, 1741

Bartko, H., Martins, F., Trippe, S., Fritz, T. K., Genzel, R., Ott, T., Eisenhauer, F., Gillessen, S., Paumard, T., Alexander, T., Dodds-Eden, K., Gerhard, O., Levin, Y., Mascetti, L., Nayakshin, S., Perets, H. B., Perrin, G., Pfuhl, O., Reid, M. J., Rouan, D., Zilka, M., & Sternberg, A. 2010, ApJ, 708, 834

Bender, R. et al. 2005, ApJ, 631, 280

Berukoff, S. J. & Hansen, B. M. S. 2006, ApJ, 650, 901

Bonnell, I. A. & Rice, W. K. M. 2008, Science, 321, 1060

Buchholz, R. M., Schödel, R., & Eckart, A. 2009, A&A, 499, 483

Chang, P., Murray-Clay, R., Chiang, E., & Quataert, E. 2007, ApJ, 668, 236

Danby, J. M. A. 1992, Fundamentals of celestial mechanics (Richmond: Willman-Bell, |c1992, 2nd ed.)

Do, T., Ghez, A. M., Morris, M. R., Lu, J. R., Matthews, K., Yelda, S., & Larkin, J. 2009, ApJ, 703, 1323

Eisenhauer, F., Schödel, R., Genzel, R., Ott, T., Tecza, M., Abuter, R., Eckart, A., & Alexander, T. 2003, ApJ, 597, L121

Eisenhauer, F. et al. 2005, ApJ, 628, 246

Genzel, R., Eisenhauer, F., & Gillessen, S. 2010, Reviews of Modern Physics, 82, 3121

Genzel, R. et al. 2003, ApJ, 594, 812

Gerhard, O. 2001, ApJ, 546, L39

Ghez, A. M., Salim, S., Hornstein, S. D., Tanner, A., Lu, J. R., Morris, M., Becklin, E. E., & Duchêne, G. 2005, ApJ, 620, 744

Ghez, A. M., Salim, S., Weinberg, N. N., Lu, J. R., Do, T., Dunn, J. K., Matthews, K., Morris, M. R., Yelda, S., Becklin, E. E., Kremenek, T., Milosavljevic, M., & Naiman, J. 2008, ApJ, 689, 1044

Ghez, A. M. et al. 2003, ApJ, 586, L127

Gillessen, S., Eisenhauer, F., Trippe, S., Alexander, T., Genzel, R., Martins, F., & Ott, T. 2009, ApJ, 692, 1075

Glebbeek, E., Gaburov, E., de Mink, S. E., Pols, O. R., & Portegies Zwart, S. F. 2009, A&A, 497, 255

Gould, A. & Quillen, A. C. 2003, ApJ, 592, 935

Gualandris, A. & Merritt, D. 2009, ApJ, 705, 361

Gürkan, M. A., Freitag, M., & Rasio, F. A. 2004, ApJ, 604, 632

Gürkan, M. A. & Rasio, F. A. 2005, ApJ, 628, 236

Haas, J., Šubr, L., & Kroupa, P. 2011, MNRAS, 412, 1905

Hansen, B. M. S. & Milosavljević, M. 2003, ApJ, 593, L77

Hartmann, M., Debattista, V. P., Seth, A., Cappellari, M., & Quinn, T. R. 2011, ArXiv e-prints

Hills, J. G. 1988, Nature, 331, 687

—. 1991, AJ, 102, 704

Hobbs, A. & Nayakshin, S. 2009, MNRAS, 394, 191

Hopkins, P. F. & Quataert, E. 2010a, MNRAS, 407, 1529

—. 2010b, MNRAS, 405, L41

Kim, S. S., Figer, D. F., & Morris, M. 2004, ApJ, 617, L123

Kim, S. S. & Morris, M. 2003, ApJ, 597, 312

Kinoshita, H., Yoshida, H., & Nakai, H. 1991, Celestial Mechanics and Dynamical Astronomy, 50, 59

Kocsis, B. & Tremaine, S. 2010, ArXiv e-prints

Lauer, T. R., Faber, S. M., Groth, E. J., Shaya, E. J., Campbell, B., Code, A., Currie, D. G., Baum, W. A., Ewald, S. P., Hester, J. J., Holtzman, J. A., Kristian, J., Light, R. M., Ligynds, C. R., O'Neil, Jr., E. J., & Westphal, J. A. 1993, AJ, 106, 1436

Levin, Y. 2007, MNRAS, 374, 515

Levin, Y. & Beloborodov, A. M. 2003, ApJ, 590, L33

Levin, Y., Wu, A., & Thommes, E. 2005, ApJ, 635, 341

Löckmann, U. & Baumgardt, H. 2009, MNRAS, 394, 1841

Löckmann, U., Baumgardt, H., & Kroupa, P. 2009, MNRAS, 398, 429

—. 2010, MNRAS, 402, 519

Lu, J. R., Ghez, A. M., Hornstein, S. D., Morris, M. R., Becklin, E. E., & Matthews, K. 2009, ApJ, 690, 1463

Madigan, A.-M., Hopman, C., & Levin, Y. 2011, ApJ, 738, 99

Madigan, A.-M., Levin, Y., & Hopman, C. 2009, ApJ, 697, L44

Maness, H., Martins, F., Trippe, S., Genzel, R., Graham, J. R., Sheehy, C., Salaris, M., Gillessen, S., Alexander, T., Paumard, T., Ott, T., Abuter, R., & Eisenhauer, F. 2007, ApJ, 669, 1024

Martins, F., Gillessen, S., Eisenhauer, F., Genzel, R., Ott, T., & Trippe, S. 2008, ApJ, 672, L119

Merritt, D. 2010, ApJ, 718, 739

Merritt, D., Alexander, T., Mikkola, S., & Will, C. 2011, ArXiv e-prints

Milosavljević, M. 2004, ApJ, 605, L13

Morris, M. 1993, ApJ, 408, 496

Nayakshin, S. & Cuadra, J. 2005, A&A, 437, 437

Nayakshin, S., Dehnen, W., Cuadra, J., & Genzel, R. 2006, MNRAS, 366, 1410

Nayakshin, S. & Sunyaev, R. 2005, MNRAS, L94+

Paumard, T., Genzel, R., Martins, F., Nayakshin, S., Beloborodov, A. M., Levin, Y., Trippe, S., Eisenhauer, F., Ott, T., Gillessen, S., Abuter, R., Cuadra, J., Alexander, T., & Sternberg, A. 2006, ApJ, 643, 1011

Peacock, J. A. 1983, MNRAS, 202, 615

Perets, H. B. & Gualandris, A. 2010, ApJ, 719, 220

Perets, H. B., Gualandris, A., Kupi, G., Merritt, D., & Alexander, T. 2009, ApJ, 702, 884

Perets, H. B., Hopman, C., & Alexander, T. 2007, ApJ, 656, 709

Pfahl, E. 2005, ApJ, 626, 849

Portegies Zwart, S. F., Makino, J., McMillan, S. L. W., & Hut, P. 2002, ApJ, 565, 265

Rauch, K. P. & Tremaine, S. 1996, New Astronomy, 1, 149

Saha, P. & Tremaine, S. 1992, AJ, 104, 1633

Sanders, R. H. 1998, MNRAS, 294, 35

Schödel, R., Eckart, A., Alexander, T., Merritt, D., Genzel, R., Sternberg, A., Meyer, L., Kul, F., Moultaka, J., Ott, T., & Straubmeier, C. 2007, A&A, 469, 125

Schödel, R., Merritt, D., & Eckart, A. 2009, A&A, 502, 91

Seth, A. C. 2010, ApJ, 725, 670

Seth, A. C., Blum, R. D., Bastian, N., Caldwell, N., & Debattista, V. P. 2008, ApJ, 687, 997
Seth, A. C., Dalcanton, J. J., Hodge, P. W., & Debattista, V. P. 2006, AJ, 132, 2539
Su, M., Slatyer, T. R., & Finkbeiner, D. P. 2010, ApJ, 724, 1044
Tremaine, S. 1995, AJ, 110, 628
Tremaine, S. D., Ostriker, J. P., & Spitzer, Jr., L. 1975, ApJ, 196, 407
Trippe, S., Gillessen, S., Gerhard, O. E., Bartko, H., Fritz, T. K., Maness, H. L., Eisenhauer, F., Martins, F., Ott, T., Dodds-Eden, K., & Genzel, R. 2008, A&A, 492, 419
Wardle, M. & Yusef-Zadeh, F. 2008, ApJ, 683, L37
—. 2011, ArXiv e-prints
Wisdom, J. & Holman, M. 1991, AJ, 102, 1528
Yu, Q. & Tremaine, S. 2003, ApJ, 599, 1129
Yusef-Zadeh, F., Bushouse, H., & Wardle, M. 2011, ArXiv e-prints
Zubovas, K., King, A. R., & Nayakshin, S. 2011, MNRAS, 415, L21

5

Secular Dynamical Anti-Friction in Galactic Nuclei

We identify a gravitational-dynamical process in near-Keplerian potentials of galactic nuclei that occurs when an intermediate-mass black hole (IMBH) is migrating on an eccentric orbit through the stellar cluster towards the central supermassive black hole (SMBH). We find that, apart from the conventional dynamical friction, the IMBH experiences an often much stronger systematic torque due to the secular (i.e., orbit-averaged) interactions with the cluster's stars. The force which results in this torque is applied, counter-intuitively, in the same direction as the IMBH's precession and we refer to its action as "secular-dynamical anti-friction" (SDAF). We argue that SDAF, and not the gravitational ejection of stars, is responsible for the IMBH's eccentricity increase as seen in previous N-body simulations. Our numerical experiments, supported by qualitative arguments, demonstrate that (1) when the IMBH's precession direction is artificially reversed, the torque changes sign as well, which decreases the orbital eccentricity, and (2) the rate of eccentricity growth is sensitive to the IMBH migration rate, with zero systematic eccentricity growth for an IMBH whose orbit is artificially prevented from inward migration.

Ann-Marie Madigan and Yuri Levin (2012)
To be submitted to The Astrophysical Journal

5.1 Introduction

RECENT studies on secular dynamics in near-Keplerian potentials (Rauch & Tremaine 1996; Hopman & Alexander 2006; Eilon et al. 2009; Kocsis & Tremaine 2011; Madigan et al. 2011) have focused attention on the long-term dynamical evolution of stars and compact objects in galactic nuclei. Due to persistent gravitational torques exerted by stellar orbits on each other as they precess slowly around the supermassive black hole (SMBH), the angular momentum evolution of stellar orbits can proceed at a much higher rate than that of energy evolution (resonant relaxation; Rauch & Tremaine 1996). In this chapter we aim to extend such research to study secular dynamical effects on the inspiral of a massive body, e.g., an intermediate-mass black hole (IMBH), into the combined potential of an SMBH and nuclear stellar cluster.

As a body of mass M moves through a distribution of field stars of individual mass m_a, the influence of accumulative encounters with the field stars on its orbit may be described using the velocity diffusion coefficients in the Fokker-Planck equation (e.g., Binney & Tremaine 2008). If $M \gg m_a$, the first-order diffusion coefficient (or drift term, $D[\Delta v_{||}]$) will be much larger than the second-order coefficients (diffusion terms, $D[(\Delta \mathbf{v}_{\perp})^2]/v$, $D[(\Delta v_{||})^2]/v$), by a factor of order M/m_a. The dominant effect of the lower mass stars is to exert a frictional force on the massive body anti-parallel to its velocity $\mathbf{v}$,

$$M\frac{d\mathbf{v}}{dt} = -16\pi^2 G^2 M^2 m_a \ln\Lambda \left[\int_0^v dv_a v_a^2 f(v_a)\right] \frac{\mathbf{v}}{v^3}. \tag{5.1}$$

This is Chandrasekhar's dynamical friction formula (Chandrasekhar 1943; Tremaine & Weinberg 1984) for an isotropic field star distribution normalized such that the density $n(r) = \int d^3 v_a f(r, v_a)$, and $\ln\Lambda$ is the Coulomb logarithm. The formula accounts only for stars moving slower than the massive body, and it neglects self-gravity of the stars themselves; Antonini & Merritt (2011) have recently updated the formula to include changes induced by the massive body on the stellar velocity distribution and the contribution from stars moving faster. The stars are deflected by the massive body into a gravitational 'wake' behind it which results in an increase in stellar density, the amplitude of which is proportional to M (Danby & Camm 1957; Kalnajs 1971; Mulder 1983); hence the gravitational force experienced by the massive body is proportional to M^2. This frictional force acts to decrease the kinetic energy and angular momentum of the massive body and it sinks towards the centre of the potential.

The picture described above does not take into account the orbit-averaged dynamics that is particular for near-Keplerian potentials and that has been shown to play a central role in the angular momentum evolution of stars near the SMBH. Indeed, it is natural to assume that some other form of dynamical friction could be associated with the orbit-averaged potential created by the IMBH, as this potential is rotating around the SMBH due to precession of the IMBH's eccentric orbit. The possibility of this secular-dynamical friction was already suggested by Rauch & Tremaine in 1996. In this chapter we explore this effect and find that, contrary to our experience with ordinary dynamical friction, the resulting torque comes from a gravitational force acting in the same direction as that of the IMBH precession. We therefore refer to this effect as "secular-dynamical anti-friction" (SDAF).

For the remainder of this chapter we will keep referring to the massive inspiraling body as an IMBH, though the reader should keep in mind that the essential dynamics will hold for any massive body moving in a near-Keplerian potential. As large mass ratio massive black hole binaries are expected to coalesce in at least some merging and non-merging galaxies (Milosavljević & Merritt 2003; Preto et al. 2011), the dynamics of such systems are important to understand. In particular, IMBH inspirals into SMBHs will be a major source of gravitational waves for space-based laser interferometers such as the proposed New Gravitational Observatory (*ELISA/NGO*)[1] (e.g., Miller 2005). Simulations of the inspiral of IMBHs ($10^2 - 10^4 M_\odot$) through nuclear stellar clusters embedding a massive black hole have shown an increase in eccentricity of the IMBH (Baumgardt et al. 2006; Matsubayashi et al. 2007; Löckmann et al. 2008; Iwasawa et al. 2011; Sesana et al. 2011; Antonini & Merritt 2011; Meiron & Laor 2011). Here we show that the theory of SDAF can explain this phenomenon, and present results of N-body simulations set up to test this claim.

5.2 Secular dynamical anti-friction

Let us consider the combined gravitational potential of an SMBH, mass $M_\bullet$, embedded in a nuclear star cluster with a power-law number density distribution, $n(r) \propto r^{-\alpha}$, and individual stellar masses m. The specific energy and angular momentum of a stellar orbit can be written in terms of Kepler elements as

$$E = -\frac{GM_\bullet}{2a}, \tag{5.2}$$

$$|\mathbf{J}| = |\mathbf{r} \times \mathbf{v}| = [GM_\bullet a(1 - e^2)]^{1/2}, \tag{5.3}$$

where a is the semi major axis of the elliptical orbit, and e is the eccentricity. The eccentricity vector, $\mathbf{e}$, of the star is that which points from the occupied focus of the orbit to the periapsis of the orbit and has a magnitude equal to the scalar eccentricity of the orbit,

$$\mathbf{e} = \frac{1}{GM_\bullet}(\mathbf{v} \times \mathbf{J}) - \hat{\mathbf{r}}. \tag{5.4}$$

The orbit of a star in this potential is nearly Keplerian (i.e. closed) but $\mathbf{e}$ will precess due to the additional (Newtonian) potential and general relativity. We define the precession time, $t_{\rm prec}$, as a timescale over which an orbit precesses by 2π rad in its plane. As Newtonian precession acts with retrograde motion (i.e., in the direction opposite of a star's motion) and general relativistic precession with prograde motion,

---

[1] https://lisa-light.aei.mpg.de/bin/view/

$$t_{\rm prec} = \left| \frac{1}{t_{\rm prec}^{\rm cl}} - \frac{1}{t_{\rm prec}^{\rm GR}} \right|^{-1}. \tag{5.5}$$

The general relativistic precession time is given by

$$t_{\rm prec}^{\rm GR} = \frac{a(1-e^2)c^2}{3GM_\bullet} P(a), \tag{5.6}$$

wtih the orbital period $P(a) = 2\pi\sqrt{a^3/GM_\bullet}$. The Newtonian precession time due to the addition of the star cluster mass in an otherwise-Keplerian potential, $t_{\rm prec}^{\rm cl}$, can be written for $\alpha \neq 2$ as

$$t_{\rm prec}^{\rm cl} = \pi(2-\alpha) f(e,\alpha)^{-1} \left[\frac{M_\bullet}{N_< m} P(a) \right], \tag{5.7}$$

where $N_<$ is the number of stars within semi-major axis a, and

$$f(e,\alpha) = \frac{\partial}{\partial \mathcal{J}} \left(\frac{1}{\mathcal{J}} \int_0^\pi \left[\frac{\mathcal{J}^2}{1+\sqrt{1-\mathcal{J}^2}\cos\phi} \right]^{4-\alpha} d\phi \right) \tag{5.8}$$

(Landau & Lifshitz 1969). Here $\mathcal{J} = J/(GM_\bullet a)^{1/2} = (1-e^2)^{1/2}$. For all values of α, the Newtonian precession time of a stellar orbit increases with eccentricity. The difference in precession times for circular and highly eccentric stellar orbits vary with α. We plot $t_{\rm prec}$ in Figure 5.1, setting the quantity in brackets $[M_\bullet/(N_< m)P(a)]$ in Equation (5.7) equal to one, with $f(e,\alpha)$ as given in Madigan et al. (2011). For a steep cusp, $\alpha = 1.75$ (Bahcall & Wolf 1976), there is a factor of ~ 5 difference in precession time for a near-circular ($e = 0.01$) and near-radial ($e = 0.99$) orbit, which increases to ~ 7 for a shallow profile $\alpha = 0.5$. We plot Equation (13) from Merritt et al. (2011) and Equation (A11) from Ivanov et al. (2005) ($\alpha = 1.5$) as a comparison. Differences arise in the normalization of the functions due to approximations made in deriving the analytical formulae in these papers; the monotonic dependence of the precession time on orbital eccentricity persists. We note that the exact expressions for the precession time in Ivanov et al. (2005) agrees with numerical evaluation of our Equation (5.7).

We now introduce an IMBH of mass $M_{\rm imbh}$ on an orbit with non-zero eccentricity, $e_{\rm imbh}$, and semi major axis, $a_{\rm imbh}$, within the dynamical radius, r_h, of the SMBH, defined such that the mass in stars at r_h equals that of the SMBH, $N(< r_h)m = M_\bullet$. As we are interested in secular dynamics[2], it is useful to envisage the mass of the IMBH spread smoothly out along its orbit, such that

---

[2] The term 'secular' refers to long-period dynamics, in which the dependence on the mean longitude of an orbit is dropped from the disturbing function (see e.g., Murray & Dermott 1999).

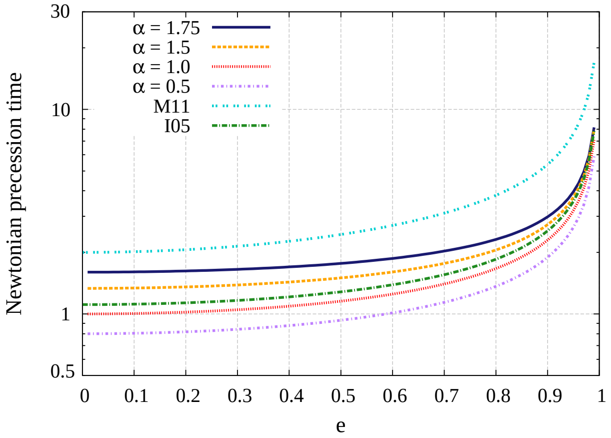

Figure 5.1 – Dependence of the precession time ($M_\bullet/(N_< m)P(a) = 1$) of a stellar orbit on orbital eccentricity, e. Several values are plotted for different power-law density profiles, $n(r) \propto r^{-\alpha}$. The dependence given in Merritt & Vasiliev (2011) (M11) and Ivanov et al. (2005) (I05) are plotted for comparison.

the local density at any segment is inversely proportional to its local velocity. The position of furthest distance from the SMBH, the apoapsis of the orbit, will therefore contain the most mass. Over a timescale longer than its orbital period but much less than the precession time, it will exert a strong (specific) gravitational torque on the orbit of a star with a similar semi major axis (Gürkan & Hopman 2007) on the order of

$$|\tau| = |\mathbf{r} \times \mathbf{F}| \sim \frac{GM_{\rm imbh} e_{\rm imbh} e}{a_{\rm imbh}} \delta\phi, \tag{5.9}$$

where $\delta\phi$ is the angle between two orbits. The orbit of the IMBH will not affect the energy (or equivalently, the semi major axis) of the stellar orbit as its gravitational potential is stationary over this timescale. A star on a co-planar orbit with the IMBH will experience a torque that is parallel (or anti-parallel) to its angular momentum vector $\mathbf{J}$. Hence the torque will act to change the magnitude of $\mathbf{J}$; equivalently, the eccentricity of the orbit. Let us consider the stellar orbit with an eccentricity $e \sim e_{\rm imbh}$ and semi major axis $a \sim a_{\rm imbh}$. We place the orbit such that its eccentricity vector forms an angle $\delta\phi$ with that of the IMBH.

If there existed no gravitational interaction (secular or otherwise) between the IMBH and the star, they would precess in the background stellar potential at the same rate. Their eccentricity vectors would rotate by 2π rad in one $t_{\rm prec}$ and $\delta\phi$ would remain constant. Switching on secular gravitational interactions results in a strong secular encounter between the star and the IMBH. The star's orbit is pushed away from the IMBH, transferring negative or positive angular

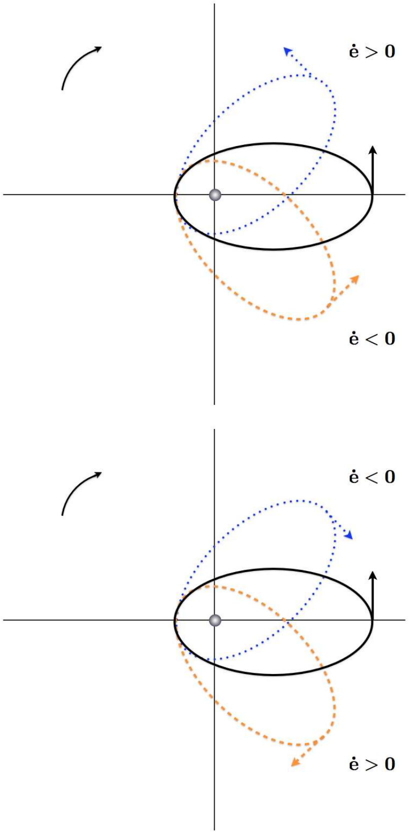
$\dot{\mathbf{e}} > \mathbf{0}$
$\dot{\mathbf{e}} < \mathbf{0}$
$\dot{\mathbf{e}} < \mathbf{0}$
$\dot{\mathbf{e}} > \mathbf{0}$

Figure 5.2 – (Top) Schematic of orbits of IMBH (black, filled line) and prograde trailing (orange, dashed line) and prograde leading (blue, dotted line) stellar orbits in the frame of reference rotating with the IMBH orbit. The velocity vectors of each are indicated at apoapsis and the direction of precession of the IMBH is shown with a curved arrow at top left. (Bottom) Schematic of orbits of IMBH (black, filled line) and retrograde trailing (orange, dashed line) and retrograde leading stellar orbits (blue, dotted line) in the frame of reference rotating with the IMBH orbit.

momentum to the orbit of the IMBH, depending on its orientation. We elaborate on the dynamics in the following:

If the star is moving on a prograde orbit (in the direction of motion of the IMBH) that trails behind the IMBH (see Figure 5.2: top), it will experience a torque in the direction of its angular momentum vector **J** such that $dJ/dt > 0$. Due to the resulting decrease in eccentricity, the stellar orbit will precess faster (see Figure 5.1) and move away from the IMBH[3].

Conversely if the stellar orbit is leading, the torque exerted on it will be anti-parallel to $\mathbf{J}$. The stellar orbit will increase in eccentricity, precess more slowly and in effect be pushed away from the orbit of the IMBH. In both cases, $d|\delta\phi|/dt > 0$.

---

[3] This mechanism involves the same interplay between stellar torques and orbital precession which results in an instability in an eccentric disk of stars near a SMBH (Madigan et al. 2009).

For a star moving along a retrograde orbit (see Figure 5.2: bottom), its precession acts in the opposite direction to that of the IMBH. If the orbit is trailing behind the IMBH, the torque will act to increase its eccentricity and hence decrease the differential precession rate between the two orbits. This increases the timescale over which the stellar orbit experiences a coherent torque and its eccentricity can increase to one. In this scenario the orbit can easily 'flip' through $e = 1$ to a prograde orbit, and be pushed away from the IMBH as described above. If if does not flip, the retrograde orbit will precess past the IMBH, experience a torque which will decrease its eccentricity and hence will increase the differential precession rate between the two orbits. Once again, in both cases the stellar orbit is pushed away from that of the IMBH, $d|\delta\phi|/dt > 0$.

In contrast to Chandrasekhar's dynamical friction, which acts to increase the density of stars behind a massive body, the effect of SDAF is to push stellar orbits away from that of the massive body. The varying strength of Chandrasekhar's dynamical friction on different segments of a massive body's orbit causes evolution of orbital eccentricity, the sign of which is dependent on the background stellar density profile (e.g., Gould & Quillen 2003; Levin et al. 2005). With SDAF, it is the relative number of prograde/retrograde stellar orbits which determines the sign of the orbital eccentricity evolution of the IMBH.

5.2.1 Increase in orbital eccentricity

The differential precession rate between the IMBH and co-planar prograde orbits at similar semi major axes is small in comparison with retrograde orbits, as the latter precess in the opposite direction to the IMBH. Hence, the IMBH orbit has a higher rate of strong interactions with retrograde orbits (on its trailing side) than prograde orbits. Therefore, in contrast with Chandrasekhar's dynamical friction where the frictional force acts against its orbital motion, the net gravitational torque experienced by the IMBH orbit comes from a force which acts along its direction of precession. Due to dynamical friction the IMBH sinks towards the center of the potential, decreasing in semi major axis. As it sinks, the retrograde orbits at similar semi-major axes donate negative angular momentum to the IMBH orbit, and its orbital eccentricity increases.

5.2.2 Comparison with theories in the literature

The N-body simulations of Iwasawa et al. (2011) show an increase in the eccentricity of an IMBH as it spirals into an SMBH. With careful analysis of the orbital properties of the field stars in their simulations, the authors attribute the increase to secular chaos (and the Kozai mechanism), brought about by the non-axisymmetric potential induced by the IMBH. This acts to bring the relative number of orbits back into balance after prograde-moving stars are preferentially ejected by the IMBH (retrograde stars have larger relative velocities with respect to the IMBH than prograde, and hence are ejected less frequently). The retrograde orbits moving to prograde orbits extract angular momentum from the orbit of the IMBH and its eccentricity increases.

Sesana et al. (2011) present both hybrid[4] and direct N-body simulations with stellar cusps of varying degrees of rotation, to examine the importance of the relative number of prograde/retrograde orbits on the orbital evolution of the IMBH. The authors propose a hypothesis in which the ejections of stars, via the slingshot mechanism, is the cause of the evolution of the IMBH eccentricity. Most retrograde orbits which end up being ejected from the potential, donate their negative angular momentum to the IMBH and move to prograde orbits before they escape. Again it is the preferential ejection of prograde orbits that drives the increase of the orbital eccentricity of the IMBH.

With SDAF, it is the cumulative secular torques from retrograde stellar orbits that lead to the increase in orbital eccentricity of an IMBH, irrespective of ejections of stars from the potential. SDAF makes testable predictions which can distinguish itself from the above theories.

1. If the orbit of the IMBH is made to artificially precess in the opposite direction to its true motion, its rate of change of angular momentum should reverse sign as well.
2. If escaping stars are injected back into the cluster with the same parameters as before their interaction with the IMBH, the eccentricity evolution of the IMBH should not qualitatively be affected.
3. Due to the ‘pushing away’ of co-planar stellar orbits, there will be a density anisotropy in the stellar distribution as a result of SDAF.
4. If dynamical friction is artificially slowed, there will be a lower rate of axisymmetric flow of retrograde orbits to one side of the IMBH’s orbit and hence a lower negative rate of change of angular momentum.

In the following section we present the results of numerical trials to test the theory of SDAF and decrease of orbital angular momentum of an IMBH in a galactic nucleus.

5.3 Numerical method and simulations

The simulations presented in this chapter are performed using a special-purpose, mixed-variable symplectic N-body integrator as described in detail in Madigan et al. (2011). We use a galactic nucleus model with parameters chosen to represent the Galactic center. At the center of the coordinate system, there is a massive black hole with $M_\bullet = 4 \times 10^6 M_\odot$ (Ghez et al. 2003), and an IMBH with a mass $M_{\rm imbh}$ within the range $[10^3 - 10^4] M_\odot$ with $0.04 < a < 0.08\,{\rm pc}$.

---

[4] The hybrid model couples numerical three-body scatterings to an analytical formalism for interactions between the cusp and the IMBH (Sesana et al. 2008).

We simulate the nuclear star cluster as a smooth potential with a power-law number density profile $n(r) \propto r^{-\alpha}$; this decreases the computation time and lends a clear, direct interpretation to our results. Typically $\alpha \in [0.5, 1.75]$, and is normalized such that at one parsec the stellar mass is $M(< 1\,\mathrm{pc}) = 1 \times 10^6 M_\odot$ (Schödel et al. 2007; Trippe et al. 2008; Schödel et al. 2009). To test our theory of SDAF, we include an isotropically-distributed population of test stars with individual masses m within the range $[10-100] M_\odot$ which gravitationally interact only with the IMBH, not with each other. In doing so we isolate the effects of the IMBH on the stellar orbits. The orbits of the IMBH and the test stars precess according to Equation (5.5), such that for each time-step, dt, they rotate in their orbital plane by an angle $|\delta\phi| = 2\pi(dt/t_{\mathrm{prec}})$.

As the IMBH moves in a smooth stellar potential, it experiences no dynamical friction from it. To account for this we use the dynamical friction formulae given by Just et al. (2011) to artificially decrease the semi major axis of the IMBH's orbit. Just et al. (2011) use a self-consistent velocity distribution function in place of the standard Maxwellian assumption and an improved formula for the Coulomb logarithm to arrive at dynamical friction timescale for a near-Keplerian potential, which can differ by a factor of three from the standard formula in Equation (5.1). The radial evolution of the IMBH (point-like object) behaves, for $\alpha \neq 3/2$, as[5]

$$r = r_0 \left(1 - \frac{t}{t_{\mathrm{DF}}}\right)^{\frac{2}{2\alpha-3}}, \tag{5.10}$$

where t_{DF} is the dynamical friction timescale calculated from the starting position of the massive body r_0,

$$t_{\mathrm{DF}} = \frac{P}{2\pi(3-\alpha)\chi \ln\Lambda} \frac{M_\bullet^2}{M_{\mathrm{imbh}} M_<}. \tag{5.11}$$

χ is the fraction of stars with velocity smaller than that of the IMBH (circular case),

$$\chi(\alpha) = \frac{1}{\sqrt{2}B(3/2, \alpha-1/2)} \int_0^1 u^2 \left(1 - \frac{u^2}{2}\right)^{\alpha-3/2} du \tag{5.12}$$

and Λ is given by

$$\Lambda = \frac{(3+\alpha)}{\alpha(1+\alpha)} \frac{M_\bullet}{M_{\mathrm{imbh}}}. \tag{5.13}$$

We implement Equations (5.10) - (5.13) by adjusting the semi major axis of the IMBH orbit at each time-step with the following transformation

$$r_t \rightarrow \beta\, r_{\mathrm{t}-1} \quad v_t \rightarrow \frac{v_{\mathrm{t}-1}}{\sqrt{\beta}}, \tag{5.14}$$

---

[5] For $\alpha = 3/2$ see similar equations in Just et al. (2011).

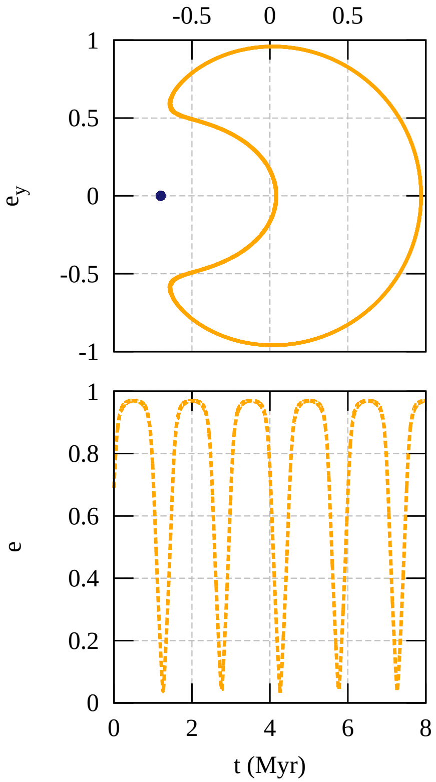

Figure 5.3 – Example of a secular horseshoe orbit of a star of mass $m = 1M_\odot$, bound to a massive black hole of mass $M_\bullet = 4 \times 10^6 M_\odot$. The stellar orbit feels a gravitational torque from an IMBH (mass $M_{\rm imbh} = 10^3 M_\odot$) and precesses due to general relativity and a background stellar potential. (Top) The eccentricity vectors of the IMBH and the prograde-directed single star in the frame co-precessing with the eccentricity vector of the IMBH. (Bottom) Eccentricity evolution of the stellar orbit over $8\,\mathrm{Myr}$ during which it performs a few secular horseshoe orbits.

$$\beta = \left(1 - \frac{t}{t_{\rm DF}(r_{\rm t-1})}\right)^{\frac{2}{2\alpha-3}} . \tag{5.15}$$

Essentially we are re-scaling the stellar ellipse, without changing its eccentricity. In the next subsections we present three examples of dynamics resulting from SDAF.

5.3.1 Secular horseshoe orbits

Horseshoe orbits describe the motion of satellite bodies in the circular planar restricted three-body problem (for a comprehensive overview see Murray & Dermott 1999) which librate on paths encompassing the $L3$, $L4$ and $L5$

Lagrangian points. Such orbits map out horseshoe shapes in the frame co-rotating with two massive bodies and have been observed in the Saturnian satellite system (Dermott & Murray 1981) and in the co-orbital Earth Asteroid 2002 AA_{29}(Connors et al. 2002).

Secular dynamical anti-friction results in *secular* horseshoe orbits[6]. Secular horseshoe orbits differ from those in our above description in that it is the eccentricity vector, as opposed to the guiding centre of the orbit which maps out a horseshoe in the frame co-rotating with the IMBH (for close analogies in planetary dynamics, see Michtchenko & Malhotra 2004; Pan & Sari 2004; Lithwick & Wu 2011). We illustrate this behaviour in Figure 5.3 where we show the position of the eccentricity vectors of a IMBH and a star in the frame of reference co-precessing with the eccentricity vector of the IMBH.

In this example $M_\bullet = 4 \times 10^6 M_\odot$, $M_{\rm imbh} = 10^3 M_\odot$, $m = 1 M_\odot$, $\alpha = 1$, $M(< 1~{\rm pc}) = 1 \times 10^6 M_\odot$, $a_{\rm imbh} = a = 0.0703~{\rm pc}$, $e_{\rm imbh} = 0.7$ and $e = 0.69$. Both the IMBH and stellar orbits are on the xy-plane with an initial angle of $\delta\phi = \pi/4~{\rm rad}$ between their eccentricity vectors. This behaviour is transitory due to non-secular gravitational interactions. The timescale over which the star in this simulation performs a horseshoe in eccentricity space is $\sim 1.5\,{\rm Myr}$, or ~ 1700 orbital periods.

5.3.2 Separation of potential into pro- and retro- grade orbits

As illustrated in Figure 5.3 the eccentricity vectors of prograde orbits which have a small inclination angle with respect to an IMBH will tend to librate about a point $\pi~{\rm rad}$ opposite that of the IMBH – the secular analogue of the Lagrangian $L3$ point. In contrast, the eccentricity vectors of retrograde orbits (those which do not flip to prograde orbits) will, in a time-averaged sense, cluster around that of the IMBH before they are pushed away, as they precess more slowly due to the increase in their orbital eccentricity. We find that the presence of a massive body, such as an IMBH, surrounded by less massive objects in a near-Keplerian potential tends to segregate the lighter objects into a region dominated by prograde orbits and one dominated by retrograde. This mechanism has the strongest effect for, but is not restricted to, co-planar orbits, as scalar angular momentum changes result in eccentricity changes whereas vector angular momentum relaxation re-orients the stellar orbital plane.

In Figure 5.4 we plot an example of this segregation. The top figure shows a schematic of eight octants in eccentricity vector space. We rotate the cluster such that the eccentricity vector of the IMBH lies parallel with (1,1,1), and follow the change in the number of massless stellar orbits with eccentricity vectors in each octant. The middle plot shows the results for prograde orbits and the bottom plot for retrograde. There is a clear increase in the number of prograde stellar orbits in octant 8, opposite that in which the IMBH lies, as expected. Furthermore, there is an enhancement of retrograde stellar orbits in octant 1 as the theory predicts.

---

[6] Referred to as "windshield-wiper orbits" in Merritt & Vasiliev (2011) in the context of non-axisymmetric star clusters.

5.3.3 Increase in orbital eccentricity of IMBH

Here we examine two of the main testable predictions of SDAF: the eccentricity evolution of an IMBH with 1) artificially reversed apsidal precession, and 2) with a decreased migration rate from Chandrasekhar's dynamical friction. We present the results of short-term simulations performed to test these predictions, using ten realizations for each simulation to look at the statistical results. In the following, $M_{\bullet} = 4 \times 10^6 M_{\odot}$, $M_{\rm imbh} = 10^4 M_{\odot}$, $a_{\rm imbh} = 0.06$ pc, $e_{\rm imbh} = 0.4$, $\alpha = 1.5$, $M(< 1 \text{ pc}) = 1 \times 10^6 M_{\odot}$. We integrate the orbits of 1000 test stars in each simulation, distributed from $0.006\,\text{pc} < a < 0.12\,\text{pc}$, with $m = 20 M_{\odot}$.

In Figure 5.5 we show the evolution of orbital eccentricity of the IMBH as a function of time in units of the initial orbital period, $P(a = 0.06 \text{ pc}) \simeq 692\,\text{yr}$. Each line shows the mean eccentricity of ten simulations. $C_{\rm prec}$ is a pre-factor placed in front of the apsidal precession angle, $\delta\phi$, at each time-step. The reference simulation with the correct precession rate $C_{\rm prec} = 1.00$ shows an increase in eccentricity as expected. Increasing the precession rate by a factor of 1.25 does not however increase the rate of eccentricity growth, as the IMBH orbit has less time to exert torques on the surrounding stellar orbits. In the next two simulations we reverse the direction of apsidal precession of the IMBH, keeping the precession period roughly constant in relation to the first two simulations. The overall eccentricity growth of the IMBH is negative, as predicted.

Next, we present the results of simulations wherein we change the migration rate of the IMBH (Figure 5.6). SDAF predicts that lower migration rates lead to slower eccentricity growth as the IMBH interacts with retrograde orbits at a lower rate. In this figure, $C_{\rm tdf}$ is a multiplicative pre-factor in front of the dynamical friction timescale given in Equation (5.11). The semi-major axis of the IMBH orbit shrinks from 0.06 pc to ~ 0.024 pc over the simulation run for $C_{\rm tdf} = 1$. For $C_{\rm tdf} = 2, 5, 10$ the eccentricity growth of the IMBH is suppressed (though still positive), exactly as SDAF predicts.

In the simulation in which we half the friction timescale ($C_{\rm tdf} = 0.5$), and hence increase the migration rate by a factor of two, the eccentricity growth rate does not increase. We attribute this to the shortening over the timescale over which the IMBH exerts persistent torques on the surrounding stellar orbits.

Finally, we run simulations wherein we soften the IMBH's gravity to such an extent that it switches off entirely for a star coming within 0.01 pc of the IMBH itself. We do so to confirm that secular dynamics are dominating the eccentricity evolution of the IMBH orbit; these conditions inhibit the three-body scatterings and ejections which are the basis for the theories given in

Iwasawa et al. (2011) and Sesana et al. (2011). We find it makes no significant difference for the angular momentum evolution of the IMBH even though it significantly reduces the number of stellar ejections (by a factor of ~ 5).

5.4 Discussion

We have presented a new secular gravitational dynamical process in galactic nuclei which acts to push low-mass stellar orbits away from that of massive bodies. It can also act to decrease the orbital angular momentum of the massive body. There are two essential components to the decrease. The first is SDAF and the net flow of retrograde orbits past that of the massive body which extracts orbital angular momentum. The second is Chandrasekhar's dynamical friction force acting on the massive body which decreases its semi major axis and provides a mechanism for net negative J change. Although we have told this story in the context of an IMBH inspiral into the centre of a galaxy, the interactions described here will be valid for any massive body in a near-Keplerian potential. Observational predictions of SDAF include higher mass objects with increasingly larger eccentricities, and density anisotropy in the stellar distribution near the plane of the massive body.

Acknowledgments A.-M.M gratefully acknowledges the hospitality of Monash University and the Aspen Center for Physics. We thank Fabio Antonini, Dan Fabrycky, Clovis Hopman, Margaret Pan, Alberto Sesana and Scott Tremaine for valuable discussions and/or comments on the text. A.-M.M is supported by a TopTalent fellowship from the Netherlands Organisation for Scientific Research (NWO) and Y.L. by a VIDI grant from NWO.

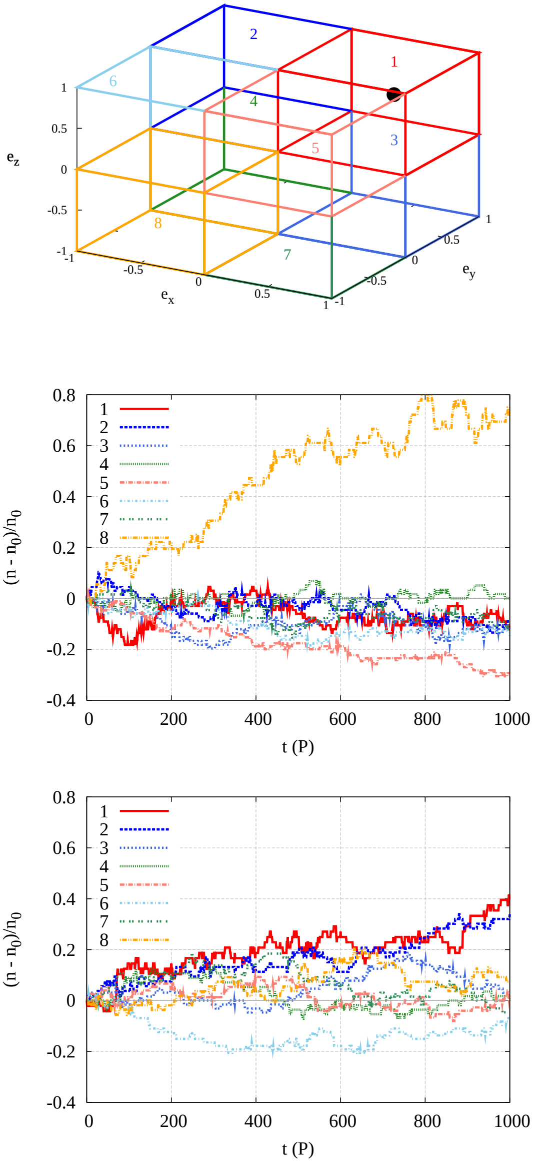

Figure 5.4 – Schematic of octants in eccentricity vector space (top). The unit eccentricity vector of the IMBH lies parallel with (1,1,1) in octant 1 (black dot). Fractional change in number of prograde (middle) and retrograde (bottom) stars in each octant in the frame rotating with the IMBH. Time is given in units of initial orbital period of the IMBH, $P(a = 0.06\ \mathrm{pc})$. The increase in the number of prograde stellar orbits in octant 8, and retrograde stellar orbits in octant 1, is as predicted.

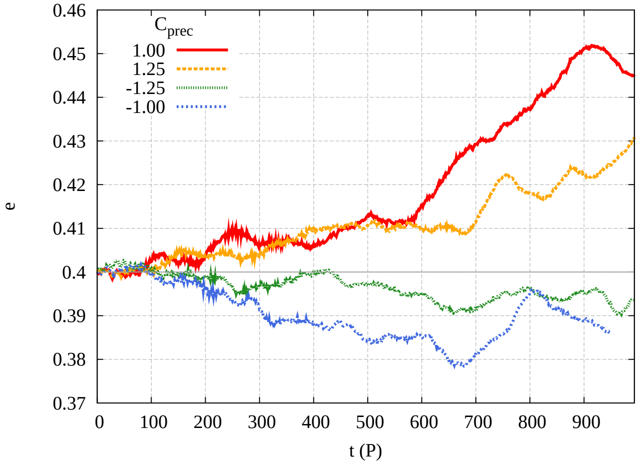

Figure 5.5 – Mean eccentricity evolution (each curve is the average of ten simulation runs) of an IMBH experiencing four different rates of apsidal precession. The first is the reference simulation with the correct precession rate corresponding to the smooth background potential (red solid line). In the second simulation, the IMBH has an increased precession rate by a factor of 1.25 (orange dotted line). In the third simulation, the IMBH has an increased precession rate by the same factor but the IMBH is made to precess in a *reversed* direction (green dotted line). In the fourth simulation, the IMBH has a precession period corresponding to the reference simulation but again in reversed direction (blue dotted line). Time is given in units of the initial orbital period $P(a = 0.06\,\mathrm{pc})$.

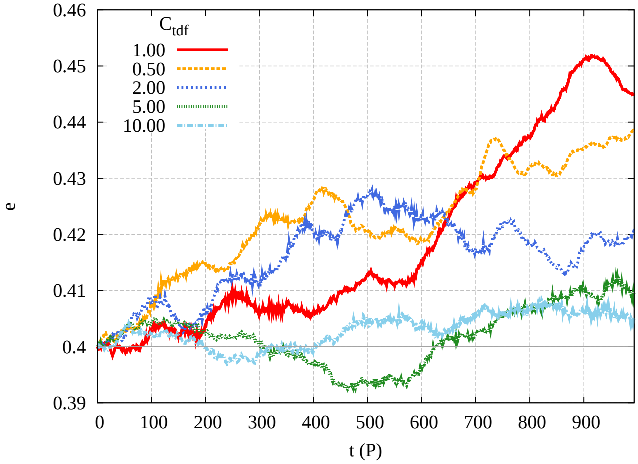

Figure 5.6 – Mean eccentricity evolution (each curve is the average of ten simulation runs) of an IMBH with five different migration rates due to dynamical friction. SDAF predicts lower rates of eccentricity growth with increasing dynamical friction timescales. The parameter C_{tdf} is a multiplicative pre-factor in front of the dynamical friction timescale given in Equation (5.11).

References

Antonini, F. & Merritt, D. 2011, ArXiv e-prints

Bahcall, J. N. & Wolf, R. A. 1976, ApJ, 209, 214

Baumgardt, H., Gualandris, A., & Portegies Zwart, S. 2006, MNRAS, 372, 174

Binney, J. & Tremaine, S. 2008, Galactic Dynamics, Second edition (Princeton, NJ: Princeton University Press)

Chandrasekhar, S. 1943, ApJ, 97, 255

Connors, M., Chodas, P., Mikkola, S., Wiegert, P., Veillet, C., & Innanen, K. 2002, Meteoritics and Planetary Science, 37, 1435

Danby, J. M. A. & Camm, G. L. 1957, MNRAS, 117, 50

Dermott, S. F. & Murray, C. D. 1981, Icarus, 48, 1

Eilon, E., Kupi, G., & Alexander, T. 2009, ApJ, 698, 641

Ghez, A. M. et al. 2003, ApJ, 586, L127

Gould, A. & Quillen, A. C. 2003, ApJ, 592, 935

Gürkan, M. A. & Hopman, C. 2007, MNRAS, 379, 1083

Hopman, C. & Alexander, T. 2006, ApJ, 645, 1152

Ivanov, P. B., Polnarev, A. G., & Saha, P. 2005, MNRAS, 358, 1361

Iwasawa, M., An, S., Matsubayashi, T., Funato, Y., & Makino, J. 2011, ApJ, 731, L9+

Just, A., Khan, F. M., Berczik, P., Ernst, A., & Spurzem, R. 2011, MNRAS, 411, 653

Kalnajs, A. J. 1971, Ap&SS, 13, 279

Kocsis, B. & Tremaine, S. 2011, MNRAS, 412, 187

Landau, L. D. & Lifshitz, E. M. 1969, Mechanics (Course of Theoretical Physics, Oxford: Pergamon Press, 1969, 2nd ed.)

Levin, Y., Wu, A., & Thommes, E. 2005, ApJ, 635, 341

Lithwick, Y. & Wu, Y. 2011, ApJ, 739, 31

Löckmann, U., Baumgardt, H., & Kroupa, P. 2008, ApJ, 683, L151

Madigan, A.-M., Hopman, C., & Levin, Y. 2011, ApJ, 738, 99

Madigan, A.-M., Levin, Y., & Hopman, C. 2009, ApJ, 697, L44

Matsubayashi, T., Makino, J., & Ebisuzaki, T. 2007, ApJ, 656, 879

Meiron, Y. & Laor, A. 2011, ArXiv e-prints

Merritt, D., Alexander, T., Mikkola, S., & Will, C. M. 2011, Phys. Rev. D, 84, 044024

Merritt, D. & Vasiliev, E. 2011, ApJ, 726, 61

Miller, M. C. 2005, ApJ, 618, 426

Milosavljević, M. & Merritt, D. 2003, ApJ, 596, 860

Michtchenko, T. A. & Malhotra, R. 2004, Icarus, 168, 237

Mulder, W. A. 1983, A&A, 117, 9

Murray, C. D. & Dermott, S. F. 1999, Solar system dynamics

Pan, M. & Sari, R. 2004, AJ, 128, 1418

Preto, M., Berentzen, I., Berczik, P. & Spurzem, R., S. 2011, ApJ, 732, L26

Rauch, K. P. & Tremaine, S. 1996, New Astronomy, 1, 149

Schödel, R., Eckart, A., Alexander, T., Merritt, D., Genzel, R., Sternberg, A., Meyer, L., Kul, F., Moultaka, J., Ott, T., & Straubmeier, C. 2007, A&A, 469, 125

Schödel, R., Merritt, D., & Eckart, A. 2009, A&A, 502, 91

Sesana, A., Gualandris, A., & Dotti, M. 2011, MNRAS, 415, L35

Sesana, A., Haardt, F., & Madau, P. 2008, ApJ, 686, 432

Tremaine, S. & Weinberg, M. D. 1984, MNRAS, 209, 729

Trippe, S., Gillessen, S., Gerhard, O. E., Bartko, H., Fritz, T. K., Maness, H. L., Eisenhauer, F., Martins, F., Ott, T., Dodds-Eden, K., & Genzel, R. 2008, A&A, 492, 419

Nederlandse samenvatting

De meeste, zo niet alle sterrenstelsels hebben met elkaar gemeen dat in het centrum een massief zwart gat[1] huist. Deze zwarte gaten zijn veel zwaarder dan sterren, en hun massa's lopen uiteen van miljoenen tot miljarden zonsmassa's. Onze eigen Melkweg is geen uitzondering op deze regel. Zeer gedetailleerde waarnemingen in infrarood hebben onomstotelijk de aanwezigheid van een zwart gat bewezen, dat ongeveer vier miljoen keer zo zwaar is als de zon.

Het zwarte gat kan (per definitie) niet direct worden waargenomen. Maar aangezien het centrum van de Melkweg op een afstand van slechts 8 kpc ligt[2] is het mogelijk om de banen van individuele sterren waar te nemen. Door deze banen is uit te rekenen wat de massa en dus (gegeven de afstand) de dichtheid van het object is dat ze aantrekt. Hieruit volgt de conclusie dat dit object enkel een zwart gat kan zijn.

De sterren die deze banen omschrijven vormen zelf een grote verrassing. Vóór de waarnemingen was de gangbare mening dat zich geen sterren zouden kunnen vormen in de buurt van een zwart gat, vanwege de zeer grote getijdenkrachten. Omdat het veel tijd kost voordat sterren van baan veranderen, was de verwachting dat zo er al sterren in de buurt van een massieve zwart gat zouden zijn, deze ouder dan een miljard jaar zouden moeten zijn. De sterren rond het zwarte gat in het centrum van de Melkweg zijn echter zeer zwaar, en omdat zware sterren maar kort leven (slechts enkele miljoenen jaren in het geval van sommige sterren rond het zwarte gat) moeten ze dus ook vrij jong zijn. Bovendien ontdekten Levin & Beloborodov (2003) dat sommige van deze jonge sterren in de vorm van een schijf rond het zwarte gat bewegen, vergelijkbaar met de beweging van de planeten om de zon. Dit suggereert dat deze groep sterren ook in die schijf zijn gevormd.

Dit proefschrift gaat over de dynamiek van sterren die zo dicht bij massieve zwarte gaten zijn dat de potentiaal wordt gedomineerd door het zwarte gat zelf. In deze situatie bewegen sterren zich ongeveer in ellipsen rond het zwarte gat, maar deze ellipsen worden over langere tijd gezien verstoord door wisselwerking met andere sterren.

---

[1] Een "massief" zwart gat is een pleonasme. In dit proefschrift nemen we dit pleonasme over van het vakjargon, waarin het woord "massief" duidt op zwarte gaten die miljoenen malen zwaarder zijn dan de zon.

[2] 1 kpc = 3,3 duizend lichtjaar.

Omdat de tijdschalen waarop verschillende dynamische effecten optreden sterk uiteenlopen is het moeilijk om deze direct te simuleren met standaard simulatiemodellen. Sommige sterren draaien in een jaar om het zwarte gat, terwijl de banen pas in de loop van miljoenen of miljarden jaren veranderen als gevolg van de verstoring door andere sterren. Voor het onderzoek in dit proefschrift heb ik daarom een nieuwe N-body simulatie ontwikkeld, die het feit uitbuit dat de baan van sterren rond het zwarte gat (dus zonder de verstoring van andere sterren) analytisch oplosbaar is. De wisselwerking met andere sterren wordt vervolgens als verstoring van deze banen beschouwd.

Het effect van verstoringen op een baan in een "gladde" potentiaal leidt er in veel andere situaties toe dat een ster een dronkaards wandel (*random walk*) uitvoert. De reden is dat ontmoetingen met andere sterren willekeurig zijn, zodat de kans op een afwijking van het "gladde" pad naar links en naar rechts even groot zijn.

Rond een massief zwart gat geldt deze aanname echter niet in alle omstandigheden. Banen in de potentiaal van een zwart gat hebben de unieke eigenschap dat ze geen precessie vertonen: de banen sluiten, en hun oriëntatie ten opzichte van de banen van andere sterren blijft gedurende zeer lange tijd hetzelfde. Als gevolg hiervan is de wisselwerking met andere sterren veel minder willekeurig dan in andere situaties, waardoor de banen veel sneller veranderen dan anders. In dit proefschrift onderzoek ik wat de gevolgen zijn van deze "seculiere effecten" voor de dynamica van sterren rond zwarte gaten.

In **hoofdstuk 2** beschouw ik de evolutie van een excentrische schijf van sterren, zoals die mogelijk is gevormd in het centrum van de Melkweg. Ik laat zien dat deze configuratie instabiel is: wanneer een baan een iets hoger dan gemiddelde excentriciteit heeft, dan groeit deze binnen relatief korte tijd (ongeveer een miljoen jaar) naar een waarde van bijna 1. Omgekeerd, als de excentriciteit iets lager is dan gemiddeld, dan wordt de baan snel cirkelvormig. Deze instabiliteit is interessant vanuit theoretisch oogpunt, maar heeft ook consequenties voor het centrum van de Melkweg. Als sommige van de objecten in de schijf dubbelsterren zijn, kan de baan zo excentrisch worden dat de dubbelster uiteen wordt gescheurd door de getijdenkrachten van het zwarte gat. In dat geval blijft één ster om een zeer nauwe baan rond het zwarte gat draaien. Omdat de processen snel verlopen zou dit de oorsprong van de waargenomen jonge sterren rond het zwarte gat kunnen verklaren.

In **hoofdstuk 3** wordt de lange termijn evolutie van sterrenbanen om een massief zwart gat gevolgd totdat een toestand van *steady state* wordt bereikt. Het is niet mogelijk om de evolutie te volgen met N-body simulaties, omdat deze te lang zouden duren. Voor het volgen van de lange termijn evolutie heb ik daarom een Monte Carlo code ontwikkeld. Een nieuw aspect aan deze code is dat zowel de gebruikelijke dronkaards wandel wordt gemodelleerd als de seculiere effecten ("*resonant relaxation*", voor het eerst beschreven in Rauch & Tremaine 1996), die over vele honderden banen gecorreleerd zijn.

De diffusiecoëfficiënten in deze code zijn gekalibreerd met N-body simulaties. Ik laat zien dat de seculiere effecten van groot belang zijn voor de *steady state* van een systeem van sterren in de buurt van een massief zwart gat. Deze evenwichtstoestand wijkt sterk af van de toestand die werd gevonden in het klassieke artikel van Bahcall & Wolf (1976). In dat artikel divergeerde de sterdichtheid naarmate de afstand tot het zwarte gat kleiner werd, maar in de *steady state* die tot stand komt uit het samenspel van seculiere effecten en sterren die als gevolg daarvan in het zwarte gat terecht komen blijven juist alleen banen met een grote half-lange as over. Een andere consequentie is dat de snelheidsverdeling van sterren in de evenwichtstoestand niet isotropisch is.

De vraag die ik in **hoofdstuk 4** probeer te beantwoorden is wat de oorsprong is van de B-sterren in het centrum van de Melkweg. Eén scenario uit de literatuur is dat deze de overblijfselen zijn van dubbelsterren die door de getijdenkrachten van het zwarte gat zijn verscheurd. Een andere mogelijkheid is dat een schijf van sterren langzaam “oplost”. Om uitsluitsel te geven volg ik de evolutie van sterrenbanen die volgt uit deze twee scenarios. De resulterende constellaties zijn zeer verschillend van elkaar. Ik laat zien dat deze verschillen ook duidelijk te zien zijn in termen van een nieuwe, direct waarneembare variabele. De al waargenomen banen zijn nog niet gepubliceerd, maar in de nabije toekomst kan deze methode waarschijnlijk (minstens) één van deze twee scenarios uitsluiten.

Hoofdstuk 5 gaat over het pad dat een object aflegt dat zwaarder is dan sterren, maar lichter dan het massieve zwarte gat – meer concreet kan hier gedacht worden aan een hypothetisch “intermediate mass” zwart gat, van duizend tot tienduizend zonsmassa’s. Algemeen bekend is dat zo’n object inspiraliseert als gevolg van dynamische wrijving. Simulaties laten zien dat daarnaast de excentriciteit onderweg toeneemt. Ik laat met analytische argumenten zien wat de oorzaak is van de groeiende excentriciteit. Deze blijkt opnieuw te zijn gelegen in seculiere effecten, waardoor sterren gemiddeld gezien impulsmoment aan het object onttrekken, een effect dat ik “seculiere dynamische antiwrijving” noem. Ik voer nieuwe simulaties uit om aan te tonen dat dit effect inderdaad verantwoordelijk is voor de toenemende excentriciteit.

Curriculum vitae

How strange it is to be anything at all.
Jeff Mangum

I was born on January 16, 1982 in Dublin, Ireland. I went to ‘St. Louis High School’ in Rathmines, where my mother taught maths. At the age of 16, I walked into my first physics class to find the question ‘*what is light?*’ written on the blackboard, and was hooked. And so, armed with the laws of reflection and refraction, I began a path in science.

In 2000, I began my bachelor studies in Physics and Astronomy at the University of Ireland, Galway. I graduated in 2004 with a First Class Honours degree and a thesis on exo-planetary transits. Following a summer research project searching for optical emission from pulsars, I spent eight months traveling in Asia. I began the Master in Astronomy program at Leiden University in 2005, supported by a research grant from the University.

During this time, three fortunate and formative events occurred: I took a course on the theory of general relativity taught by an inspiring new faculty member, Yuri Levin; I attended an exciting talk by a new postdoc, Clovis Hopman, on the inspiral of compact stellar remnants into massive black holes, and I won an NWO ‘Toptalent’ fellowship which allowed me to independently choose the direction of my future PhD research. I chose to work with Yuri and Clovis on stellar dynamics near massive black holes, and this thesis is largely a result of these timely circumstances.

During my PhD, I presented my research at international conferences in the Netherlands, Germany, Ireland, Israel, China, Australia and the United States, and visited Monash University in Melbourne for four months. As of December 2011, I am a post-doc at Leiden Observatory and, having sent off my post-doc applications for the fall 2012, am looking forward to the next step on this path.

Acknowledgments

People love chopping wood.
In this activity one immediately sees results.
Albert Einstein

ALTHOUGH writing a thesis can take a long time, my years at Leiden have flown by too fast. It was wonderful to be a student here and I'm grateful to everyone in the astronomy department for their help and friendship over the years, including the support staff who hold it all together.

Thanks to the old gang (now sadly dispersed) who made Leiden so much fun: Nina, Sarah, Remco, Rik, Hendrik, Andreas, Olmo, Rob, Freeke, Niruj, Tip and Craig (Boooth!). And a nerdy high-five to the first astro(awesome)-ph club, especially to Ryan, Steven, Jeroen, Ernst and Marcel who showed us how to make spiral arms in our coffee. I'm very grateful to the members of our theory group – Evghenii, Anders, Richard, Atakan, Clovis – I always felt privileged to be part of it. I'm also thankful for the friends I've made outside the observatory: in particular to Jonathan and Pantelis.

Thanks to everyone at Monash for showing me around Melbourne and instilling in me a healthy respect for rubidium. Maarten, I thoroughly enjoyed our blackboard discussions (*. . . magnets, how do they work?*), and Rutger, skydiving was just the beginning; we will indeed keep it up. Thanks to Sarah Levin for delicious meals and exquisite company, both in Leiden and Australia.

Conor, from sharing your maths notes with me 11 years ago to being by my side during these last few frenetic months, you've been amazing (thanks a million). Amelia, I hope we continue to narrate our lives together. It wouldn't be half so much fun without you. Martin, thank you for your warmth and friendship, and for all the wonderful times we've had. Olja, you've been the best friend and officemate in the whole universe - thank you for everything.

Finally, thanks so much to my family back home. First and foremost to my parents, Ev and Dave, for your love and support. Thanks to my brothers Ciaran and Danny, to all my aunts and uncles, grannies, my niece and (especially!) cousins for your interest and encouragement throughout the years. Cheers.